REPORT NO.
UCB/SESM-86/01

STRUCTURAL ENGINEERING AND
STRUCTURAL MECHANICS

APPLICATIONS OF MECHANICS TO CELL AND DEVELOPMENTAL BIOLOGY

by

LOUIS Y. CHENG

MAY 1986

DEPARTMENT OF CIVIL ENGINEERING
UNIVERSITY OF CALIFORNIA
BERKELEY, CALIFORNIA

Abstract

This is a study of cell and developmental biology based on the principles of mechanics. Cells and embryos are idealized as axisymmetric shell-like bodies containing a body of incompressible material. According to this view, this study devotes its first part to developing computational tools based on the finite element method. The tools formulated include an axisymmetric shell/membrane element based on a stress resultant formulation, valid for modeling finite bending, shearing and stretching; a volume constraint algorithm based on the Lagrange multiplier method; and a contact algorithm based on the penalty method. These analysis tools facilitate the study of three commonly used mechanical experiments on sea urchin eggs -- the compression experiment, the suction experiment, and the magnetic particle experiment. These numerical simulations are useful not only in obtaining mechanical property data, but in providing insights to these mechanical experiments that other approximate analyses cannot provide. The analysis tools are also utilized to study two developmental events -- gastrulation in sea urchins and neurulation in amphibia. By not focusing on the molecular basis of the cell shape changes during development, but concentrating on the mechanical consequences of the motion itself, this study reveals a great deal about the mechanisms driving embryonic shape changes.

Acknowledgements

I thank my advisors, Professors Robert Taylor and George Oster, for their guidance and encouragement.

I thank Professor Jacob Lubliner for encouraging me to pursue biomechanics, and for serving on my Dissertation Advisory Committee.

I thank Professor Raymond Keller for his invaluable comments on my work on sea urchin gastrulation, and for serving on my Dissertation Advisory Committee.

I also thank Professor Garrett Odell for his suggestions on modeling of neurulation; Professor Richard Skalak for the discussions on the mechanical experiments on cells; Professor Antone Jacobson for providing the illustrations for the developmental sequence of newt embryos; my fellow graduate students, Jean Paul Vincent and Jeffery Hardin for their many tutorials on biology; Professor Angela Cheer for sharing her insights on biomechanical modeling.

My gratitude extends to the people who encouraged me to pursue my doctorate at Berkeley, including Professors Lucien Schmit, Richard Nelson and Stanley Dong from U.C.L.A., and Dr. Marvin Ito and Dr. Russell England from California Institute of Technology, Inc.

The last but not the least, I thank my wife, Beth Pao, and all my family members, especially my "old-friend", Mr. Pe-Ya Lin, for their encouragement and understanding.

This research was supported by an NSF Grant MCS810557 to George F. Oster.

Table of Contents

Chapter 1

Introduction

1.1. Cell and developmental biology. Basic notions.

A cell is a concentrated solution of chemicals bounded by a membrane. Almost all multicellular organisms originate from a single cell, the fertilized egg. This cell, through cell divisions, differentiation and reorganization, develops into a layered embryo with specialized regions which are the rudiments of future organs. The study of how cells develop into organs is the subject of developmental biology.

Readers may wonder why mechanics plays a role in cell and developmental biology. Examining the ultrastructure of a cell will shed light on this question. The cytoplasm inside a cell contains protein fibers, many of which appears to form a structured network. The crosslinking of these fibers enables the cell to sustain tensile and compressive forces. For this reason, the fiber network is often referred to as the *cytoskeleton*. The cytoskeleton contains the protein actin, which interacts with myosin to generate active contractile forces in a manner similar to muscle contractions. Therefore, a cell is a mechanical system, capable of *passively* resisting forces, and *actively* generating forces. This mechanical machinery, regulated by chemical activities, is responsible for the shape changes that an embryo and its constituent cells undergo during development. Therefore, mechanical studies will certainly improve our understanding of these developmental phenomena.

1.2. Scope.

The initial focus of this study is on developing computational tools suited for mechanical analyses of cells and embryos. Our objective here is to develop tools that are both accurate and efficient, and yet general enough to handle a wide range of problems in cell and developmental biology. In the second half of this study we apply these tools to consider specific problems of interest.

1.3. Theoretical considerations of cells and embryos.

We shall model cells and embryos as axisymmetric shell-like bodies containing a body of incompressible material. For cells, the thickness of the cortical layer is generally small compared to its radius of curvature. Since the membrane action is dominant in this case, a *membrane* theory (in the sense of the theory of shells) is sufficient to capture the mechanical behavior of the cortex. Embryos, on the other hand, are lined by one or more cell layers, which resist bending and shearing, in addition to stretching. Modeling these behaviors requires a *shell* theory.

Perhaps the main difficulty in mechanical modeling of cells and embryos, and for most other biological materials, lies in characterizing their material properties. Since there is hardly any quantitative material description on cells and embryos, we shall assume a linear stress-strain relationship. Our simulations of mechanical experiments in a later chapter will prove this to be a good first approximation.

1.4. Computational tools.

In Chapter 2 we present an axisymmetric shell/membrane theory. This shell theory, deduced from the three-dimensional theory of continuum mechanics, is valid for modeling finite stretching, shearing and bending of the shell.

The shell equations are then adapted to a computational algorithm based on the finite element method.

When the shell deforms in response to loading, the incompressible material inside the shell constrains its motions. We model this by a volume constraint algorithm based on the Lagrange multiplier method. The theoretical details of the method are presented in Chapter 3.

Chapter 3 also contains the theoretical description of a contact algorithm based on the penalty function formulation. This algorithm models the mechanical interactions between material bodies, which will be used in the next chapter to simulate mechanical experiments.

1.5. **Applications.**

These computational tools facilitate mechanical analyses for many problems in cell and developmental biology. In Chapter 4 we consider several commonly used mechanical experiments on cells. The primary objective of that study is to demonstrate a theoretically sound procedure for analyzing mechanical experiments in a unified manner. This approach is not only useful for determining mechanical properties of cells, but it also gives invaluable insights to experiments that approximate analyses cannot provide.

Finally, we utilize these computational tools to study developmental biology in Chapter 5. There, we consider two examples -- gastrulation in sea urchins and neurulation in amphibia. By not focusing on the molecular basis of the cell shape changes, but concentrating on the mechanical consequences of the motion itself, we are able to learn a great deal about the mechanisms driving embryonic shape changes.

Chapter 2

Large Deformations of Axisymmetric Shells and Membranes

A Stress Resultant Formulation

2.1. Introduction.

We present here a nonlinear theory of axisymmetric shells, subjected to torsionless axisymmetric loading. The formulation, derived on the basis of the three dimensional theories of continuum mechanics, is capable of modeling finite stretching, shearing and bending of the shell.

A basic feature of this formulation is the description of the kinematics of the shell by means of an orthogonal moving frame. This approach, originally employed by Simo [1982,1984] for beams, identifies this moving frame with the deformed section of the shell. By specifying the dependence of this moving frame on the transverse coordinate of the shell, a variety of kinematic assumptions can be enforced. The formulation presented herein employs the "straight normal remains straight" assumption, which is introduced by prescribing the moving frame to be invariant over the deformed section of the shell. In conjunction with the notion of the moving frame is the use of the first Piola-Kirchhoff stresses to derive the stress resultants. These stress resultants, when resolved into components relative to the moving frame, take on the direct physical meaning of the normal and shear forces, as well as the moments. For this reason, the exact governing field equations of the shell can be deduced directly from the material form of the three-dimensional theory.

Since both the shell and the loading are axisymmetric, the theory involved becomes one-dimensional. Despite the simplification, the proper reduction of this theory from the three-dimensional theory requires the use of curvilinear coordinates. In Section 2.2, the use of special coordinate systems for the

axisymmetric shell are introduced. The results regarding the geometry of these coordinate systems are recorded in Appendix 1. Due to the axisymmetry of the shell, the moving frame is constrained such that the base vector normal to the meridian plane remains normal throughout the deformation history. Details regarding the kinematics of the shell are given in Section 2.3.

The rest of the chapter is organized as follows. The derivations of the stress resultants and the equilibrium equations for the shell are given in Sections 2.4 and 2.5. The strain measures conjugate to the stress resultants are derived in Section 2.6 through the virtual work expression. We emphasize that the formulation derived here reduces to the Kirchhoff-Love theory for sufficiently small membrane and shear strains and small motions. In Section 2.7, the shell is specialized to the membrane case when the thickness of the shell is negligible compared to its radius of curvature. To complete the theory, several constitutive relations are postulated for the shell and membrane cases in Section 2.8.

Section 2.9 is concerned with adapting the resulting set of shell equations to a computational algorithm. Here, we employ the mixed finite element method based on the Reissner-Hellinger variational formulation. Consistent linearization procedures of Hughes and Pister [1978] are utilized to cast the nonlinear problem into an incremental formulation. A full Newton-Raphson iterative scheme is then used to obtain the solution.

We consider the case of the follower pressure loading in Section 2.10. Because the loading term varies with the deformation, linearization procedures as in Section 2.9 produce a tangent operator which is nonsymmetric at the element level. In the case of a conservative system, this "load" tangent stiffness achieves a symmetric form at the global level, consistent with the finding of Hibbitt [1979] and Schweizerhof and Ramm [1984].

Finally, we illustrate the performance of the formulation by means of numerical examples. Results obtained here are compared with those found in the literature.

2.2. Notation.

We define the reference (material) configuration B for an axisymmetric shell-like body as a surface of revolution having a constant thickness h, obtained by rotation of a meridian about the axis of symmetry (Fig. 2.1). For simplicity, we consider this meridian as initially straight, with length L. Thus body B assumes the shape of a frustrum, with its orientation parametrized by the angle α as shown.

We refer to points in B as $\mathbf{X}$. We further designate a mapping Φ to describe the deformation of the shell, so that $\Phi(B)$ is the deformed configuration. By this deformation map Φ, point $\mathbf{X}$ is mapped to point $\mathbf{x}$ in the deformed configuration by $\mathbf{x} = \Phi(\mathbf{X}) \in \Phi(B)$ (Fig. 2.2).

For this development, we assign the coordinate system of a right circular cone to describe both the reference and the deformed configurations. Appendix 1 records the results regarding the geometry of this coordinate system. Let points $\mathbf{X} \in B$ and $\mathbf{x} \in \Phi(B)$ be referred to by their position vectors $\mathbf{X}$ and $\mathbf{x}$, respectively. Then a point $\mathbf{X}$ in the reference configuration can be identified by the coordinates $X^I, I=1,3$, with covariant base vectors $\mathbf{G}_I$, $I = 1,3$ (Fig. 2.2). Similarly, a point $\mathbf{x}$ in the deformed configuration can be described by another set of coordinates $x^i, i=1,3$, with covariant base vectors $\mathbf{g}_i$, $i = 1,3$ (Fig. 2.2). Both of these coordinate systems are considered to be fixed in space.

In employing the coordinate system of a circular cone, it is noted that the base vectors in the hoop direction, namely $\mathbf{G}_3$ and $\mathbf{g}_3$, are not unit vectors. Thus coordinates associated with these base vectors are not measures of linear

distances. Throughout this development, we identify a unit vector with a circumflex, and a physical component of a tensor quantity with bracketed indices.

Finally, we shall use upper case symbols to denote variables and indices for the reference configuration, and lower case symbols for those of the deformed configuration. Partial differentiation with respect to X^1 are denoted by a prime.

2.3. Kinematic considerations.

2.3.1. Kinematic description.

Since both the geometry of the shell and the load acting on it are axisymmetric, the deformation is constrained to take place only in the meridian plane (i.e. the plane normal to the base vectors $\mathbf{G}_3$ and $\mathbf{g}_3$). A pictorial illustration of the kinematics of the shell in this plane is given in Fig. 2.2.

The kinematic assumption employed in this theory is the ***straight normal remains straight*** hypothesis. Based on this assumption, the orientation of the deformed section can be described by the angle ψ which is constant across the thickness of the shell. Thus, three kinematic variables -- the angle $\psi(X^1)$, and the reference surface displacements $u(X^1)$ and $w(X^1)$ in the directions of the base vectors $\mathbf{g}_1$ and $\mathbf{g}_2$, respectively -- fully characterize the deformation of the shell. In the context of the ***moving frame*** proposed by Simo [1982,1984], the angle ψ describes the orientation of the frame with respect to the reference surface of the shell.

Referring to Fig. 2.2, the points on the shell after deformation $\mathbf{x} = \boldsymbol{\Phi}(\mathbf{X})$ can be expressed in terms of these kinematic variables by

$$\mathbf{x} = \boldsymbol{\Phi}(\mathbf{X}) = \boldsymbol{\Phi}_0(X^1,X^3) + \boldsymbol{\Phi}_1(X^1,X^2)\,. \tag{2.3.1}$$

The first member of (2.3.1), $\Phi_o(X^1,X^3)$, is the deformation map of the reference surface, i.e., $\Phi_o(X^1,X^3) = \Phi(\mathbf{X})|_{X^2=0}$, where

$$\Phi_o(X^1,X^3) = (X^1+u(X^1))\,\mathbf{g}_1 + w(X^1)\,\mathbf{g}_2 + X^3\mathbf{g}_3 \equiv \mathbf{x}_o\,. \tag{2.3.2}$$

The second member $\Phi_1(X^1,X^2)$ is the rotation of the cross section of the shell by the angle ψ, and is given by

$$\Phi_1(X^1,X^2) = X^2\,[-\sin\psi(X^1)\,\mathbf{g}_1 + \cos\psi(X^1)\,\mathbf{g}_2]. \tag{2.3.3}$$

Based on (2.3.1), a number of pertinent kinematic quantities can be computed. First, the deformation gradient is defined by $\mathbf{F} = \dfrac{\partial\Phi}{\partial\mathbf{X}}$, with components $F^a{}_A = \dfrac{\partial x^a}{\partial X^A}$. Denoting the differentiation with respect to X^1 by a prime, the deformation gradient associated with the deformation map in (2.3.1) is

$$\mathbf{F} = F^a{}_A\,\mathbf{g}_a \otimes \mathbf{G}^A \tag{2.3.4}$$

where

$$\left[F^a{}_A\right] = \begin{bmatrix} 1+u'-X^2\psi'\cos\psi & -\sin\psi & 0 \\ w'-X^2\psi'\sin\psi & \cos\psi & 0 \\ 0 & 0 & 1 \end{bmatrix}.$$

The corresponding Jacobian $J = \det|F^a{}_A| = \varepsilon^{LMN}\varepsilon_{pqr}F^p{}_L F^q{}_M F^r{}_N$, where ε^{LMN} and ε_{pqr} are the permutation tensors corresponding to the shell coordinate system given in Appendix 1. Making use of (2.3.4) and (A1.13), the Jacobian is

$$J = \frac{r}{R}\,[(1+u')\cos\psi + w'\sin\psi - X^2\psi']. \tag{2.3.5}$$

Here, r and R are the radii in the deformed and the reference configurations, respectively, where

$$r = (X^1+u-X^2\sin\psi)\sin\alpha + (w+X^2\cos\psi)\cos\alpha\,, \qquad R = X^1\sin\alpha + X^2\cos\alpha.$$

For later reference, we define a related quantity $J_o = J|_{\chi^2=0,r=R}$ so that

$$J_o = (1+u')\cos\psi + w'\sin\psi \,. \tag{2.3.6}$$

The right Cauchy-Green tensor $\mathbf{C}$ is defined by $\mathbf{C} = \mathbf{F}^T\mathbf{F}$. In component form, $\mathbf{C} = C_{AB}\,\mathbf{G}_A\otimes\mathbf{G}_B = F^a{}_A F^b{}_B g_{ab}\,\mathbf{G}_A\otimes\mathbf{G}_B$, where the metric tensor g_{ab} for the shell coordinate system is given in Appendix 1. For use in later developments, the components C_{12} and C_{22} are evaluated here:

$$C_{12} = -(1+u')\sin\psi + w'\cos\psi \,, \qquad C_{22} = 1. \tag{2.3.7}$$

2.3.2. Geometry of the deformed section.

In subsequent sections we shall resolve the stress resultants into components relative to the moving frame to give physical forces and moments. It is therefore important to keep track of the motions of this moving frame.

Since an axisymmetric shell does not deform in the direction normal to the meridian plane in Fig. 2.2, a vector originally lying in the hoop direction of the shell remains in the same direction after deformation, although the magnitude of this vector may change. We label this vector in the deformed state by $\mathbf{l}_\theta$, and describe the orientation of the deformed section of the shell by the vectors $\mathbf{n}$ and $\mathbf{l}$ (Fig. 2.2).

The unit normal $\hat{\mathbf{n}}$ is related to the unit base vector $\mathbf{G}_1$ ($=\hat{\mathbf{G}}_1$, see (A1.7)) by

$$\frac{d\omega}{d\Omega}\hat{\mathbf{n}} = J\mathbf{F}^{-T}\hat{\mathbf{G}}_1 \tag{2.3.8}$$

where ω and Ω are cross sectional areas in the deformed and the reference configurations, respectively. The quantity $\mathbf{F}^{-T}$, computed from $\mathbf{F}$ in (2.3.4), takes the form:

$$\mathbf{F}^{-T} = (F^{-T})^a{}_A\,\mathbf{g}_a\otimes\mathbf{G}^A \tag{2.3.9}$$

where

$$\left[(F^{-T})^{a}{}_{A}\right] = \frac{\tau}{RJ}\begin{bmatrix}\cos\psi & -(w'-X^2\psi'\sin\psi) & 0\\ \sin\psi & 1+u'-X^2\psi'\cos\psi & 0\\ 0 & 0 & J\frac{R^3}{\tau^3}\end{bmatrix}.$$

Evaluation of (2.3.8) using (2.3.9) gives the result

$$\frac{d\omega}{d\Omega}\hat{\mathbf{n}} = \frac{\tau}{R}(\cos\psi\mathbf{g}_1 + \sin\psi\mathbf{g}_2)\,. \tag{2.3.10}$$

Since the base vectors $\mathbf{g}_1$ and $\mathbf{g}_2$ are unit vectors, it follows that

$$\frac{d\omega}{d\Omega} = \frac{\tau}{R}\,, \qquad \hat{\mathbf{n}} = \cos\psi\mathbf{g}_1 + \sin\psi\mathbf{g}_2\,. \tag{2.3.11}$$

The other unit base vectors $\hat{\mathbf{G}}_2$ $(=\mathbf{G}_2)$ and $\hat{\mathbf{G}}_3$ $(=\mathbf{G}_3/R)$ are mapped by the deformation gradient $\mathbf{F}$ onto the vectors $\mathbf{l}$ and $\mathbf{l}_3$:

$$\mathbf{l} = \mathbf{F}\hat{\mathbf{G}}_2 = -\sin\psi\mathbf{g}_1 + \cos\psi\mathbf{g}_2 \equiv \hat{\mathbf{l}}\,, \tag{2.3.12a}$$

$$\mathbf{l}_3 = \mathbf{F}\hat{\mathbf{G}}_3 = \mathbf{F}\frac{\mathbf{G}_3}{R} = \frac{1}{R}\mathbf{g}_3 = \frac{\tau}{R}\hat{\mathbf{g}}_3 \equiv \frac{\tau}{R}\hat{\mathbf{l}}_3\,. \tag{2.3.12b}$$

where the vectors $\hat{\mathbf{l}}$ and $\hat{\mathbf{l}}_3$ above are the unit vectors of $\mathbf{l}$ and $\mathbf{l}_3$, respectively. It is worth noting that $\mathbf{l}\times\mathbf{l}_3 = \frac{d\omega}{d\Omega}\hat{\mathbf{n}}$ and that the unit vectors $\hat{\mathbf{n}}$, $\hat{\mathbf{l}}$, and $\hat{\mathbf{l}}_3$ form an orthogonal triad for the moving frame.

From (2.3.11) and (2.3.12), we can now describe the geometry of the deformed section by a transformation matrix $\mathbf{\Lambda}(X^1)$:

$$\mathbf{\Lambda}(X^1) \equiv \begin{bmatrix}\cos\psi & -\sin\psi & 0\\ \sin\psi & \cos\psi & 0\\ 0 & 0 & 1\end{bmatrix}, \tag{2.3.13}$$

such that

$$\begin{Bmatrix}\hat{\mathbf{n}}\\ \hat{\mathbf{l}}\\ \hat{\mathbf{l}}_3\end{Bmatrix} = \mathbf{\Lambda}^T(X^1)\begin{Bmatrix}\mathbf{g}_1\\ \mathbf{g}_2\\ \hat{\mathbf{g}}_3\end{Bmatrix}. \tag{2.3.14}$$

Since this theory does not account for the effect of warping of the section, $\mathbf{\Lambda}(X^1)$ appears here as a function of X^1 only. If warping of the section was included, $\mathbf{\Lambda}$ would also be a function of X^2 (see Simo [1982]).

2.4. Stresses and stress resultants.

In the study of large deformations of shells, the meanings of the quantities such as stresses, and stress resultants must be further clarified from those used in the infinitesimal case. Distinctions need to be made regarding the state of deformation these defined quantities are referred to. Our derivations of the stress resultants will be based on the *first Piola-Kirchhoff* stresses. Stress resultants derived using these stresses will take on the direct physical meanings of forces and moments, as we shall illustrate in this section.

2.4.1. Areas and stresses. Physical components.

We first evaluate the physical components of areas and stresses. These quantities will be used for computing the stress resultants. Among the base vectors employed here, only $\mathbf{G}_3$ and $\mathbf{g}_3$ are not dimensionless unit vectors. Therefore, only the components associated with this direction are not in physical dimensions.

Areas. We define an infinitesimal area vector $\mathbf{dA}^{(I)}$ as an area whose normal vector is parallel to the contravariant base vector $\mathbf{G}^I$. Those for the cases I=1 and I=3 are illustrated in Fig. 2.3. The area vector expressed in component form is

$$\mathbf{dA}^{(I)} = dA_I \mathbf{G}^I ; \quad I=1,3 \quad \text{(no summation on } I\text{)}. \tag{2.4.1}$$

For I=1,

$$\mathbf{dA}^{(1)} = dX^2\mathbf{G}_2 \times dX^3\mathbf{G}_3 = \varepsilon_{231} dX^2 dX^3 \mathbf{G}^1 = R dX^2 dX^3 \mathbf{G}^1. \tag{2.4.2a}$$

The last member in (2.4.2a) is computed using (A1.14a). Similarly,

$$\mathbf{dA}^{(2)} = R dX^1 dX^3 \mathbf{G}^2 , \qquad \mathbf{dA}^{(3)} = R dX^1 dX^3 \mathbf{G}^3 . \tag{2.4.2b,c}$$

Comparison of (2.4.1) and (2.4.2) gives the expressions for the area components dA_I. The corresponding *physical* area components, $dA_{<I>}$, can be determined by applying (A1.7) to (2.4.2). We then obtain the following result:

$$\begin{aligned} dA_{<1>} &= dA_1 = R dX^2 dX^3 , \\ dA_{<2>} &= dA_2 = R dX^1 dX^3 , \\ dA_{<3>} &= dA_3 / R = dX^1 dX^2 . \end{aligned} \tag{2.4.3}$$

Stresses. The *first Piola-Kirchhoff* stress tensor $\mathbf{P}$ is related to the Cauchy stress tensor $\boldsymbol{\sigma}$ by $\boldsymbol{\sigma} = \frac{1}{J}\mathbf{FP}$, where $\mathbf{F}$ is the deformation gradient tensor. The tensor $\mathbf{P}$ is a two-point tensor, which can be expressed in component form as

$$\mathbf{P} = P^{Ij}\, \mathbf{G}_I \otimes \mathbf{g}_j . \tag{2.4.4}$$

Its superscript j is associated with the force acting in the direction of $\mathbf{g}_j$ in the current configuration, while the superscript I with the area in the reference configuration whose normal lies in the direction of $\mathbf{G}_I$. For the axisymmetric shell considered here, P^{Ij} takes the form

$$\left[P^{Ij}\right] = \begin{bmatrix} P^{11} & P^{12} & 0 \\ P^{21} & P^{22} & 0 \\ 0 & 0 & P^{33} \end{bmatrix} . \tag{2.4.5}$$

The component P^{33} in (2.4.5) is not in physical dimensions. Its physical component, $P^{<33>}$, will be determined next.

We first consider the forces acting on the sections of the shell. We denote the vector $\mathbf{dF}^{(I)}$ as an infinitesimal force acting over an area $\mathbf{dA}^{(I)}$ with its normal vector parallel to $\mathbf{G}^I$, as illustrated in Fig. 2.3a. Expressed in terms of

stresses,

$$\mathbf{dF}^{(I)} = P^{Ij} dA_I \, \mathbf{g}_j \,. \tag{2.4.6}$$

Utilizing (A1.7) and (2.4.2c) for the case I=3,

$$\mathbf{dF}^{(3)} = P^{33} dA_3 \, \mathbf{g}_3 = P^{33} (R dX^1 dX^2) \tau \, \hat{\mathbf{g}}_3 \,. \tag{2.4.7a}$$

The same force vector can be expressed in terms of physical components by using (2.4.3c),

$$\mathbf{dF}^{(3)} = P^{<33>} dA_{<3>} \hat{\mathbf{g}}_3 = P^{<33>} dX^1 dX^2 \hat{\mathbf{g}}_3 . \tag{2.4.7b}$$

Comparing the last members of (2.4.7a) and (2.4.7b) gives the desired result:

$$P^{<33>} = P^{33} R \tau . \tag{2.4.8}$$

2.4.2. Stress resultants — forces.

The definitions of the normal and shear forces acting on the shell will be determined here. Again, we consider the infinitesimal force vector in (2.4.6). Inserting the area definition (2.4.2a) into this expression for the case I=1,

$$\mathbf{dF}^{(1)} = P^{1j} dA_1 \, \mathbf{g}_j = P^{1\beta} R \, dX^2 dX^3 \, \mathbf{g}_\beta \,, \tag{2.4.9}$$

where the repeated index β implies summation over indices 1 and 2 only, in view of (2.4.5). The stress components of $\mathbf{P}$ acting on the section of the shell (i.e. on the face normal to $\mathbf{G}_1$) can be resolved into components along the directions $\hat{\mathbf{n}}$ and $\hat{\mathbf{l}}$ according to the following:

$$\sigma = \hat{\mathbf{n}} \cdot (\mathbf{P}^T \mathbf{G}_1) \,, \qquad \tau = \hat{\mathbf{l}} \cdot (\mathbf{P}^T \mathbf{G}_1) \,, \tag{2.4.10}$$

where σ is the normal stress and τ the shear stress. By rewriting $\mathbf{\Lambda}(X^1)$ in (2.3.14) as a 2 × 2 matrix, such that

$$\begin{Bmatrix} \mathbf{g}_1 \\ \mathbf{g}_2 \end{Bmatrix} = \mathbf{\Lambda}(X^1) \begin{Bmatrix} \hat{\mathbf{n}} \\ \hat{\mathbf{l}} \end{Bmatrix} , \qquad \mathbf{\Lambda}(X^1) = \begin{bmatrix} \cos\psi & -\sin\psi \\ \sin\psi & \cos\psi \end{bmatrix} , \tag{2.4.11}$$

equation (2.4.10) becomes

$$\begin{Bmatrix} \sigma \\ \tau \end{Bmatrix} = \mathbf{\Lambda}^T(X^1) \begin{Bmatrix} P^{11} \\ P^{12} \end{Bmatrix} . \tag{2.4.12}$$

Thus we can rewrite $\mathbf{dF}^{(1)}$ in (2.4.9) as

$$\mathbf{dF}^{(1)} = (\sigma \hat{\mathbf{n}} + \tau \hat{\mathbf{l}})\, R\, dX^2 dX^3 . \tag{2.4.13}$$

Integrating (2.4.13) over the thickness of the shell, and defining $\mathbf{F}^{(1)}$ as the force vector per radian gives

$$\mathbf{F}^{(1)} = N^{mn} \hat{\mathbf{n}} + V^{ml} \hat{\mathbf{l}} \tag{2.4.14}$$

where

$$N^{mn} \equiv \frac{1}{R} \int_{-h/2}^{h/2} \sigma R dX^2 , \qquad V^{ml} \equiv \frac{1}{R} \int_{-h/2}^{h/2} \tau R dX^2 . \tag{2.4.15}$$

N^{mn} and V^{ml} are the normal and the shear forces respectively, acting on the deformed section of the shell.

Similarly, by defining $\mathbf{F}^{(3)}$ as the force per unit length and integrating (2.4.7b) over the shell thickness, the result is

$$\mathbf{F}^{(3)} = \int_{-h/2}^{h/2} \mathbf{P}^{<33>} dX^2 \hat{\mathbf{g}}_3 = N^{\phi\phi} \hat{\mathbf{g}}_3 . \tag{2.4.16}$$

In the above,

$$N^{\phi\phi} \equiv \int_{-h/2}^{h/2} P^{<33>} dX^2 \tag{2.4.17}$$

is the normal force in the hoop direction.

2.4.3. Stress resultants -- moments.

Applying the analogous treatment as above, we can systematically establish the definitions of the moment resultants acting on the shell. The infinitesimal moment vector $\mathbf{dM}^{(I)}$ induced by those stress components acting on face I can be expressed as

$$\mathbf{dM}^{(I)} = \varepsilon_{ijk}\, d^i P^{Ij}\, dA_I\, \mathbf{g}^k \tag{2.4.18}$$

where the moment arm $\mathbf{d}$ above is

$$\mathbf{d}(\mathbf{x}) = \mathbf{x} - \mathbf{x}_o = \Phi(\mathbf{X}) - \Phi(\mathbf{X})\big|_{X^2=0}\,. \tag{2.4.19a}$$

Employing the expression of $\Phi(\mathbf{X})$ in (2.3.1), the components of $\mathbf{d}(\mathbf{x})$ are

$$d^1 = -X^2 \sin\psi\,, \qquad d^2 = X^2 \cos\psi\,. \tag{2.4.19b}$$

Using (2.4.2a), (A1.7), and (A1.13a) for the case I=1, (2.4.18) becomes

$$\mathbf{dM}^{(1)} = \varepsilon_{\alpha\beta 3}\, d^\alpha P^{1\beta}\, dA_1\, \mathbf{g}^3 = \varepsilon_{\alpha\beta 3}\, d^\alpha P^{1\beta}\, R\, dX^2 dX^3\, \hat{\mathbf{g}}^3\,. \tag{2.4.20}$$

where the indices α,β are summed over 1 and 2 only, in view of (2.4.5). Defining $\mathbf{M}^{(1)}$ as the moment resultant per radian, and integrating (2.4.20) over the thickness of the shell,

$$\mathbf{M}^{(1)} = \frac{1}{R}\int_{-h/2}^{h/2} (d^1 P^{11} + d^2 P^{12}) R\, dX^2\, \hat{\mathbf{g}}_3. \tag{2.4.21}$$

Substitution of (2.4.19b) into (2.4.21) yields a simple expression

$$\mathbf{M}^{(1)} = -\frac{1}{R}\int_{-h/2}^{h/2} (P^{12}\sin\psi + P^{11}\cos\psi)\, X^2\, R\, dX^2\, \mathbf{g}^3 = -M^{mn}\, \mathbf{g}^3 \tag{2.4.22}$$

where

$$M^{mn} \equiv \frac{1}{R}\int_{-h/2}^{h/2} \sigma X^2\, R\, dX^2 \tag{2.4.23}$$

is the moment acting on the deformed section of the shell, in the direction of $\hat{\mathbf{g}}^3$ (note that $\mathbf{g}_3 \parallel \mathbf{g}^3$). The relation of σ to $P^{1\beta}$ in (2.4.12) has been utilized in establishing (2.4.23).

Next we consider the infinitesimal moment $\mathbf{dM}^{(3)}$. From (2.4.18), and taking into account the form of $\mathbf{P}$ in (2.4.5), this moment can be expressed as:

$$\mathbf{dM}^{(3)} = \varepsilon_{\alpha 3\beta}\, d^\alpha P^{33}\, dA_3\, \mathbf{g}^\beta = \varepsilon_{\alpha 3\beta}\, d^\alpha P^{33}\, R\, dX^1 dX^2\, \mathbf{g}^\beta. \tag{2.4.24}$$

In terms of the physical component $P^{<33>}$ in (2.4.8),

$$\mathbf{dM}^{(3)} = r\, e_{\alpha 3\beta}\, d^\alpha \frac{P^{<33>}}{Rr} R\, dX^1 dX^2\, \mathbf{g}^\beta = e_{\alpha 3\beta}\, d^\alpha P^{<33>}\, dX^1 dX^2\, \mathbf{g}^\beta. \tag{2.4.25}$$

Integrating (2.4.25) over the shell thickness, and defining $\mathbf{M}^{(3)}$ as the moment per unit length, we obtain

$$\mathbf{M}^{(3)} = \int_{-h/2}^{h/2} (d^2\mathbf{g}^1 - d^1\mathbf{g}^2) P^{<33>} dX^2. \tag{2.4.26}$$

Since $\mathbf{g}^1 = \mathbf{g}_1$, and $\mathbf{g}^2 = \mathbf{g}_2$ (Appendix 1), substituting (2.4.11) and (2.4.19b) into (2.4.26) gives

$$\mathbf{M}^{(3)} = M^{\phi\phi}\, \hat{\mathbf{n}} \tag{2.4.27}$$

where

$$M^{\phi\phi} \equiv \int_{-h/2}^{h/2} X^2 P^{<33>} dX^2 \tag{2.4.28}$$

is the moment acting on the deformed section of the shell in the direction normal to this section.

We shall denote the set of force and moment resultants derived above as $\mathbf{S}$, where

$$\mathbf{S} \equiv [N^{nn}\ N^{\phi\phi}\ M^{nn}\ M^{\phi\phi}\ V^{nl}]^T. \tag{2.4.29}$$

Box 2.4.1 contains a summary of the definitions of the components of **S**. It is noted that our approach here not only gives the magnitude of the forces and moments acting on the shell, but also the directions in which they act. Fig. 2.3b illustrates the orientations of these resultants graphically.

Box 2.4.1. Definitions of the stress resultants acting on the shell.

$$\mathbf{S} \equiv [N^{\alpha n}\ N^{\alpha\delta}\ M^{\alpha n}\ M^{\alpha\delta}\ V^{nl}]^T$$

$$N^{\alpha n} \equiv \frac{1}{R}\int_{-h/2}^{h/2} \sigma R dX^2$$

$$N^{\alpha\delta} \equiv \int_{-h/2}^{h/2} P^{<33>} dX^2$$

$$M^{\alpha n} \equiv \frac{1}{R}\int_{-h/2}^{h/2} \sigma X^2 R\, dX^2$$

$$M^{\alpha\delta} \equiv \int_{-h/2}^{h/2} X^2 P^{<33>} dX^2$$

$$V^{nl} \equiv \frac{1}{R}\int_{-h/2}^{h/2} \tau R dX^2$$

2.5. Balance of forces and moments.

2.5.1. Momentum balance.

Neglecting the inertial effects, the balance of linear momentum equation in the material form is

$$DIV\,\mathbf{P} + \rho_{ref}(\mathbf{X})\mathbf{B}(\mathbf{X}) = \mathbf{0}\,, \tag{2.5.1}$$

where **P** is the first Piola-Kirchhoff stress tensor, $\rho_{ref}(\mathbf{X})$ the density in the reference configuration B, and $\mathbf{B}(\mathbf{X}) = B^i\mathbf{g}_i$ the body forces per unit volume in B. In view of (2.4.4)

$$DIV\,\mathbf{P} = \mathbf{G}^J \frac{\partial}{\partial X^J}\cdot \mathbf{P} = \mathbf{G}^J \cdot \frac{\partial P^{Ii}}{\partial X^J}\mathbf{G}_I \otimes \mathbf{g}_i + \mathbf{G}^J \cdot P^{Ii}\frac{\partial \mathbf{G}_I}{\partial X^J}\otimes \mathbf{g}_i + \mathbf{G}^J \cdot P^{Ii}\mathbf{G}_I \otimes \frac{\partial \mathbf{g}_i}{\partial X^J}\,.$$

Utilizing the Christoffel symbols defined in (A1.15), the identities $\mathbf{G}_I \cdot \mathbf{G}^J = \delta_I{}^J$ and $F^\alpha{}_A = \dfrac{\partial x^\alpha}{\partial X^A}$, the above expression can be simplified to become

$$DIV\mathbf{P} = \left[\frac{\partial P^{Ji}}{\partial X^J} + \Gamma_{IJ}{}^J P^{Ii} + P^{Jk}\gamma_{kj}{}^i F^j{}_J\right]\mathbf{g}_i\,. \tag{2.5.2}$$

The Christoffel symbols for the shell coordinate system are given in (A1.21) and (A1.22). Substituting these into (2.5.2), and using the expressions for the deformation gradient in (2.3.4), the component form of the linear momentum balance equation in (2.5.1) becomes

$$\frac{1}{R}\left[\frac{\partial}{\partial X^A}(RP^{A\beta})\right] - r\frac{\partial r}{\partial x^\beta}P^{33} + \rho_{ref}B^\beta = 0 \quad ;\ \beta = 1,2\,, \tag{2.5.3}$$

where the repeated index A implies summation over 1 and 2, and

$$\frac{\partial r}{\partial x^1} = \sin\alpha\,, \qquad \frac{\partial r}{\partial x^2} = \cos\alpha\,. \tag{2.5.4}$$

In terms of the physical component $P^{<33>}$ in (2.4.8), (2.5.3) becomes

$$\frac{1}{R}\left[\frac{\partial}{\partial X^A}(RP^{<A\beta>})\right] - \frac{1}{R}\frac{\partial r}{\partial x^\beta}P^{<33>} + \rho_{ref}B^\beta = 0 \quad ;\ \beta = 1,2\,. \tag{2.5.5}$$

In the above, $P^{<A\beta>} = P^{A\beta}$ for $A,\beta < 3$. For simplicity, the brackets for their superscripts will be dropped.

The linear moment balance equation (2.5.5) forms a basis on which the balance of forces and of moments are determined. In the following development the stress resultants will be referred to frequently. See Box 2.4.1 for reference.

2.5.2. Balance of forces.

The balance of forces acting on the shell can be obtained simply by the integration of the linear moment balance equation (2.5.5) over the shell thickness

$$\int_{-h/2}^{h/2}\left\{\frac{1}{R}\left[\frac{\partial}{\partial X^A}(RP^{A\beta})\right] - \frac{1}{R}\frac{\partial r}{\partial x^\beta}P^{<33>} + \rho_{ref}B^\beta\right\}RdX^2 = 0 \quad ; \ \beta = 1,2$$

Performing the above integration and dividing the expression by the factor R, we obtain

$$\frac{1}{R}\frac{\partial}{\partial X^1}\int_{-h/2}^{h/2}RP^{1\beta}dX^2 - \frac{1}{R}\frac{\partial r}{\partial x^\beta}\int_{-h/2}^{h/2}P^{<33>}dX^2 + \frac{1}{R}\int_{-h/2}^{h/2}\rho_{ref}RB^\beta dX^2 + p^\beta(X^1) = 0 \quad (2.5.6)$$

where the last term above is the surface traction acting on the shell and is defined as

$$p^\beta(X^1) \equiv P^{2\beta}\Big|_{-h/2}^{h/2}.$$

The third term represents the loading induced by the body force; we shall not include this effect in this study. The remaining terms can now be replaced by the stress resultants N^{mn}, V^{mi}, and $N^{\theta\theta}$, giving the final form of the force equilibrium equations for the shell:

$$\frac{1}{R}\frac{\partial}{\partial X^1}\left[R\Lambda(X^1)\begin{Bmatrix}N^{mn}\\V^{mi}\end{Bmatrix}\right] - \frac{N^{\theta\theta}}{R}\begin{Bmatrix}\sin\alpha\\\cos\alpha\end{Bmatrix} + \begin{Bmatrix}p^1(X^1)\\p^2(X^1)\end{Bmatrix} = \begin{Bmatrix}0\\0\end{Bmatrix}. \quad (2.5.7)$$

2.5.3. Balance of moments.

The equilibrium equation for the resultant moments acting on the deformed section of the shell can also be derived from the linear momentum balance equation (2.5.5). First we consider the moment M^{mn} defined in (2.4.23) by rewriting it in the form:

$$M^{mn} = -\frac{1}{R}e_{ij3}\int_{-h/2}^{h/2} d^i P^{1j} R dX^2 \tag{2.5.8}$$

where d^i is given in (2.4.19). We differentiate the quantity $M^{mn}R$ with respect to X^1,

$$\frac{\partial(M^{mn}R)}{\partial X^1} = -e_{ij3}\int_{-h/2}^{h/2}\left[\frac{\partial d^i}{\partial X^1}(P^{1j}R) + d^i\frac{\partial(P^{1j}R)}{\partial X^1}\right]dX^2 \tag{2.5.9}$$

where indices $(i,j)=(1,2)$ or $(2,1)$ due to the permutation symbol. We now can make use of the linear momentum balance equations to simplify (2.5.9).

Neglecting the term involving the body force, the first of the equilibrium equations in (2.5.5) can be restated as

$$\frac{\partial P^{1j}R}{\partial X^1} = \frac{\partial r}{\partial x^j}P^{<33>} - \frac{\partial(P^{2j}R)}{\partial X^2}.$$

Substituting this into (2.5.9) gives

$$\begin{aligned}\frac{\partial(M^{mn}R)}{\partial X^1} &= -e_{ij3}\int_{-h/2}^{h/2}\left[\frac{\partial d^i}{\partial X^1}(P^{1j}R) + d^i\frac{\partial r}{\partial x^j}P^{<33>} - d^i\frac{\partial(P^{2j}R)}{\partial X^2}\right]dX^2\\ &= -e_{ij3}\int_{-h/2}^{h/2}\left[\frac{\partial d^i}{\partial X^A}(P^{Aj}R) + d^i\frac{\partial r}{\partial x^j}P^{<33>} - \left(d^i\frac{\partial(P^{2j}R)}{\partial X^2} + \frac{\partial d^i}{\partial X^2}(RP^{2j})\right)\right]dX^2\\ &= -e_{ij3}\int_{-h/2}^{h/2}\left[\frac{\partial d^i}{\partial X^A}(P^{Aj}R) + d^i\frac{\partial r}{\partial x^j}P^{<33>} - \frac{\partial}{\partial X^2}(d^i RP^{2j})\right]dX^2\end{aligned} \tag{2.5.10}$$

where the repeated index A implies summation on $A=1,2$. The last term in the above represents the contribution by an applied external moment. This type of loading will not be considered in this development.

We first operate on the first term in (2.5.10). Differentiating the definition of $\mathbf{d}$ in (2.4.19a) gives

$$\frac{\partial d^i}{\partial X^A} = F^i{}_A - \frac{\partial x_o{}^i}{\partial X^1}\delta^1{}_A$$

Using this, and having the Cauchy stress expressed as $J\sigma^{ij} = F^i{}_A P^{Aj}$, the first term in (2.5.10) becomes

$$-e_{ij3}\int_{-h/2}^{h/2}\frac{\partial d^i}{\partial X^A}(P^{Aj}R)dX^2 = e_{ij3}\int_{-h/2}^{h/2}\left[\frac{\partial x_o^i}{\partial X^1}P^{1j}R - J\sigma^{ij}R\right]dX^2 .$$

In the above expression, the product involving the symmetric Cauchy stress and the antisymmetric permutation symbol vanishes. Using (2.3.2) for $\mathbf{x}_o$, (2.4.12) for the stresses σ and τ, and (2.4.15) for the force resultants N^{mn} and V^{ml}, the first term of (2.5.10) can be further simplified as follows:

$$-e_{ij3}\int_{-h/2}^{h/2}\frac{\partial d^i}{\partial X^A}(P^{Aj}R)dX^2 = e_{ij3}\int_{-h/2}^{h/2}\frac{\partial x_o^i}{\partial X^1}P^{1j}RdX^2 = \int_{-h/2}^{h/2}[-w'\ 1+u']\begin{Bmatrix}P^{11}\\P^{12}\end{Bmatrix}RdX^2$$

$$= [-w'\ 1+u']\Lambda(X^1)\int_{-h/2}^{h/2}\begin{Bmatrix}\sigma\\\tau\end{Bmatrix}RdX^2 = -R[w'-(1+u')]\Lambda(X^1)\begin{Bmatrix}N^{mn}\\V^{ml}\end{Bmatrix}.$$

We simplify the second term of (2.5.10) via the substitutions of (2.4.19b) and (2.5.4) for $\mathbf{d}$ and $\frac{\partial r}{\partial x^j}$ respectively, which gives

$$-e_{ij3}\int_{-h/2}^{h/2}d^i\frac{\partial r}{\partial x^j}P^{<33>}dX^2 = \sin(\psi+\alpha)\int_{-h/2}^{h/2}X^2P^{<33>}dX^2 = M^{\phi\phi}\sin(\psi+\alpha) .$$

We can now rewrite (2.5.10) to give the equilibrium equation for the resultant moments:

$$\frac{1}{R}\frac{\partial(M^{mn}R)}{\partial X^1} + [w'-(1+u')]\Lambda(X^1)\begin{Bmatrix}N^{mn}\\V^{ml}\end{Bmatrix} - \frac{M^{\phi\phi}}{R}\sin(\psi+\alpha) = 0 . \qquad (2.5.11)$$

Expressing (2.5.11) in terms of the quantities J_o and C_{12} derived in (2.3.6) and (2.3.7) respectively, one finally gets

$$\frac{1}{R}\frac{\partial(M^{mn}R)}{\partial X^1} + C_{12}N^{mn} - J_o V^{ml} - \frac{M^{\phi\phi}}{R}\sin(\psi+\alpha) = 0 . \qquad (2.5.12)$$

2.6. Conjugate Strain Measures.

Next we identify the strain measures **E** for the shell that are in the work sense conjugate to the stress resultants **S** defined in Section 2.4. For this development, the material of the axisymmetric shell is considered to be hyperelastic, with the strain energy denoted as $W(\mathbf{X},\mathbf{F})$.

By the fact that the transpose of the first Piola-Kirchhoff stress **P** and the deformation gradient **F** are *conjugate* measures, the former can be determined from the strain energy according to

$$\mathbf{P}^T = \frac{\partial W(\mathbf{X},\mathbf{F})}{\partial \mathbf{F}} . \tag{2.6.1}$$

For the same reason, we can also write the variation of the strain energy stored in the shell of volume B as:

$$\delta W = \int_B \mathbf{P}^T : \delta \mathbf{F}\, dV = \int_B \mathbf{P} : \delta \mathbf{F}^T\, dV \tag{2.6.2}$$

where $\delta(\cdot)$ denotes the variation of a quantity.

We shall derive the strain measures **E** such that the stress resultants **S** can be determined from a strain energy potential $W(X^1,\mathbf{E})$ according to

$$\mathbf{S} = \frac{\partial W(X^1,E)}{\partial \mathbf{E}} . \tag{2.6.3}$$

And in analogy to (2.6.2),

$$\delta W(X^1,\mathbf{E}) = \int_0^L \mathbf{S}\cdot\delta\mathbf{E}\, R dX^1 . \tag{2.6.4}$$

2.6.1. Variations of strain measures.

Our derivation proceeds with (2.6.2). The integration of (2.6.2) over the thickness will reduce the expression to the form of (2.6.4). From this the strain measures can be determined. In this derivation, we make use of the first Piola-

Kirchhoff stress $\mathbf{P}$ in (2.4.5), and the deformation gradient $\mathbf{F}$ for the shell in (2.3.4).

The integrand of the last member in (2.6.2) can be expressed in component form as

$$\mathbf{P}:\delta\mathbf{F}^T = (P^{Ij}\mathbf{G}_I\otimes\mathbf{g}_j):(g_{ab}\delta F^b{}_B G^{AB}\mathbf{g}^a\otimes\mathbf{G}_A) = P^{Ij}\delta F^b{}_B g_{jb} G^{AB} G_{IA} = P^{Ij}\delta F^j{}_I g_{jj}$$

where the last member above arises as a result of the diagonal nature of the metric tensors. Using the expression for the metric tensor in (A1.8), the above becomes

$$\mathbf{P}:\delta\mathbf{F}^T = P^{11}\delta F^1{}_1 + P^{12}\delta F^2{}_1 + P^{21}\delta F^1{}_2 + P^{22}\delta F^2{}_2 + (r)^2 P^{33}\delta F^3{}_3 \qquad (2.6.5)$$

$$= P^{11}\delta F^1{}_1 + P^{12}\delta F^2{}_1 + P^{21}\delta F^1{}_2 + P^{22}\delta F^2{}_2 + \frac{r}{R}P^{<33>}\delta F^3{}_3$$

in which (2.4.8) is utilized to convert P^{33} to its physical component $P^{<33>}$.

The variation of the deformation gradient tensor $\delta\mathbf{F}$ is equal to the covariant derivative of the variation of the displacement vector $\delta\mathbf{v}$ (Marsden and Hughes [1983]). In component form

$$(\delta F)^a{}_A = \delta v^a|_A \,. \qquad (2.6.6)$$

In view of (2.3.1), $\delta\mathbf{v} = \delta\mathbf{x} = \delta\mathbf{\Phi}$. Thus,

$$\delta\mathbf{v} = \delta\mathbf{\Phi} = \delta\Phi^1\mathbf{g}_1 + \delta\Phi^2\mathbf{g}_2 \,, \qquad (2.6.7)$$

where

$$\delta\Phi^1 = \delta u - X^2\cos\psi\delta\psi \,, \qquad \delta\Phi^2 = \delta w - X^2\sin\psi\delta\psi \,.$$

Carrying out the covariant differentiation in (2.6.7), (2.6.6) becomes

$$(\delta\mathbf{F})_A = \delta\mathbf{\Phi}|_A = \frac{\partial\delta\Phi^c}{\partial X^A}\mathbf{g}_c + \delta\Phi^c\frac{\partial\mathbf{g}_c}{\partial X^A} = \frac{\partial\delta\Phi^c}{\partial X^A}\mathbf{g}_c + \delta\Phi^c\gamma_{ca}{}^b F^a{}_A\mathbf{g}_b$$

where the summation of $c = 1,2$ is implied above, and $\gamma_{ca}{}^b$ is the Christoffel symbol associated with the deformed configuration. As given in (A1.21), $\gamma_{c3}{}^3$ is the

only nonzero case for the shell coordinate system. Accordingly,

$$(\delta \mathbf{F})_A = \frac{\delta \partial \Phi^1}{\partial X^A}\mathbf{g}_1 + \frac{\delta \partial \Phi^2}{\partial X^A}\mathbf{g}_2 + \frac{\delta\Phi^1 \sin\alpha + \delta\Phi^2 \cos\alpha}{r} F^3{}_A\, \mathbf{g}_3 . \tag{2.6.8}$$

Substituting (2.6.7) and (2.3.4) into (2.6.8) gives

$$\left[\delta F^\alpha{}_A\right] = \begin{bmatrix} \delta F^1{}_1 & \delta F^1{}_2 & 0 \\ \delta F^2{}_1 & \delta F^2{}_2 & 0 \\ 0 & 0 & \delta F^3{}_3 \end{bmatrix} \tag{2.6.9}$$

where

$$\delta F^1{}_1 = \delta u' + X^2\psi'\delta\psi\sin\psi - X^2\delta\psi'\cos\psi , \qquad \delta F^1{}_2 = -\delta\psi\cos\psi ,$$

$$\delta F^2{}_1 = \delta w' - X^2\psi'\delta\psi\cos\psi - X^2\delta\psi'\sin\psi , \qquad \delta F^2{}_2 = -\delta\psi\sin\psi ,$$

$$\delta F^3{}_3 = \frac{(\delta u - X^2\cos\psi\delta\psi)\sin\alpha + (\delta w - X^2\sin\psi\delta\psi)\cos\alpha}{r} = \frac{\delta r}{r} .$$

Thus the variation of the strain energy as defined in (2.6.2) becomes

$$\delta W = 2\pi \int_0^L \left[\int_{-h/2}^{h/2} \left\{ \delta u \left(P^{<33>}\frac{\sin\alpha}{R}\right) + \delta w \left(P^{<33>}\frac{\cos\alpha}{R}\right) + \delta u' P^{11} + \delta w' P^{12} \right. \right. \tag{2.6.10}$$

$$+ \delta\psi \left(X^2\psi' [\sin\psi \; -\cos\psi] \begin{Bmatrix} P^{11} \\ P^{12} \end{Bmatrix} - [\cos\psi \; \sin\psi] \begin{Bmatrix} P^{21} \\ P^{22} \end{Bmatrix} - P^{<33>}\frac{X^2\sin(\psi+\alpha)}{R} \right)$$

$$\left. \left. - \delta\psi' X^2 [\cos\psi \; \sin\psi] \begin{Bmatrix} P^{11} \\ P^{12} \end{Bmatrix} \right\} R dX^2 \right] dX^1$$

We shall rewrite (2.6.10) in terms of the stress resultants in Box 2.4.1. During this process, our references to terms in (2.6.10) will not include the integral sign $\int_0^L dX^1$ for convenience.

The first two terms in (2.6.10) which contain $P^{<33>}$ can be combined to give

$$\int_{-h/2}^{h/2} P^{<33>} dX^2 \, (\sin\alpha\delta u + \cos\alpha\delta w) = N^{\theta\theta} (\sin\alpha\delta u + \cos\alpha\delta w) ,$$

where we make use of the definition of $N^{\phi\phi}$. The next two terms in (2.6.10) are simplified by converting the stresses P^{11} and P^{12} to the stresses σ and τ via (2.4.12), followed by applying the definitions of N^{mn} and V^{ml}. These terms become:

$$\left\{\delta u' \left(\cos\psi N^{mn} - \sin\psi V^{ml}\right) + \delta w' \left(\sin\psi N^{mn} + \cos\psi V^{ml}\right)\right\} R .$$

By a similar approach, the last term in (2.6.10) involving $\delta\psi'$ can be shown to equal $-\delta\psi' M^{mn} R$.

Next consider the terms associated with $\delta\psi$ in (2.6.10). First, the part involving P^{11} and P^{12} equals

$$\int_{-h/2}^{h/2} \delta\psi X^2\psi' [\sin\psi - \cos\psi]\begin{Bmatrix} P^{11} \\ P^{12} \end{Bmatrix} R dX^2 = \int_{-h/2}^{h/2} \delta\psi X^2\psi' [\sin\psi - \cos\psi]\Lambda(X^1)\begin{Bmatrix} \sigma \\ \tau \end{Bmatrix} R dX^2$$

$$= -\int_{-h/2}^{h/2} \delta\psi X^2\psi' \tau R dX^2 .$$

The relation (2.4.12) is used to obtain the second member of the above equation. Next, the part containing P^{21} and P^{22} equals

$$-\int_{-h/2}^{h/2} \delta\psi [\cos\psi \ \sin\psi]\begin{Bmatrix} P^{21} \\ P^{22} \end{Bmatrix} R dX^2 = -\int_{-h/2}^{h/2} \delta\psi \left(\tau J\frac{R}{\tau} - C_{12}\sigma\right) R dX^2 .$$

The detail of the derivation leading to this result above is given in Appendix 2. Finally, the part involving $P^{<33>}$ equals $-\delta\psi M^{\phi\phi}\sin(\psi+\alpha)$ when the definition of $M^{\phi\phi}$ is used. Combining these three expressions, the term involving $\delta\psi$ in (2.6.10) takes the form

$$-\delta\psi\left\{\int_{-h/2}^{h/2} (J_o\tau - C_{12}\sigma) R dX^2 + M^{\phi\phi}\sin(\psi+\alpha)\right\} = -\delta\psi\left\{J_o V^{ml} - C_{12}N^{mn} + \frac{M^{\phi\phi}\sin(\psi+\alpha)}{R}\right\} R$$

where J_0 and C_{12} are defined in (2.3.6) and (2.3.7), respectively.

Inserting the above results into (2.6.10) will give the variation of the strain energy in the form of (2.6.4). Since the coefficients of the stress resultants in the resulting expression are the variations of the corresponding conjugate strain measures; for the stress resultants $\mathbf{S}$ in the form

$$\mathbf{S} = [N^{mn} \;\; N^{\hat{\alpha}\hat{\beta}} \;\; M^{mn} \;\; M^{\hat{\alpha}\hat{\beta}} \;\; V^{nl}]^T , \tag{2.4.29}$$

the variations $\delta\mathbf{E}$ of the corresponding conjugate strain measures $\mathbf{E}$ are

$$\delta\mathbf{E} = \begin{Bmatrix} \cos\psi\delta u' + \sin\psi\delta w' + C_{12}\delta\psi \\ (\sin\alpha\delta u + \cos\alpha\delta w)/R \\ -\delta\psi' \\ -\delta\psi\sin(\psi+\alpha)/R \\ -\sin\psi\delta u' + \cos\psi\delta w' - J_0\delta\psi \end{Bmatrix} . \tag{2.6.11}$$

2.6.2. Strain measures.

We shall demonstrate in the sequel that these derived strain variations in (2.6.11) are in fact associated with stretches bearing physical significance. We proceed by examining the physical meanings of the stretches.

A line on the neutral surface of the shell originally lying parallel to the base vector $\mathbf{G}_1$, assumes the shape described by the vector field $\boldsymbol{\lambda}$ when deformed, where

$$\boldsymbol{\lambda} = \mathbf{F}\mathbf{G}_1\big|_{\chi^2=0} = (1+u')\mathbf{g}_1 + (w')\mathbf{g}_2 . \tag{2.6.12}$$

Resolving $\boldsymbol{\lambda}$ into components in the directions $\hat{\mathbf{n}}$ and $\hat{\mathbf{l}}$ gives,

$$\boldsymbol{\lambda} = \lambda_n\hat{\mathbf{n}} + \lambda_l\hat{\mathbf{l}} \tag{2.6.13}$$

where

$$\lambda_n \equiv \boldsymbol{\lambda}\cdot\hat{\mathbf{n}} = (1+u')\cos\psi + w'\sin\psi = J_o \ , \tag{2.6.14a}$$

$$\lambda_t \equiv \boldsymbol{\lambda}\cdot\hat{\mathbf{t}} = -(1+u')\sin\psi + w'\cos\psi = C_{12} \ . \tag{2.6.14b}$$

These components, λ_n and λ_t, represent the stretching in the direction $\hat{\mathbf{n}}$ and the shearing in the direction $\hat{\mathbf{t}}$, respectively. Similarly, the stretch in the hoop direction λ_ϑ can be found by

$$\lambda_\vartheta = (\mathbf{F}\hat{\mathbf{G}}_3)\cdot\hat{\mathbf{g}}_3\big|_{X^2=0} = (\mathbf{F}\frac{\mathbf{G}_3}{R})\cdot r\,\mathbf{g}_3\big|_{X^2=0} = \frac{(X^1+u)\sin\alpha + w\cos\alpha}{R} \tag{2.6.15}$$

Taking the variations of these stretches in (2.6.14) and (2.6.15) reveals that $\delta\lambda_n$, $\delta\lambda_t$ and $\delta\lambda_\vartheta$ are exactly the coefficients for the stress resultants N^{nn}, V^{nt}, and $N^{\vartheta\vartheta}$ respectively in (2.6.4). The corresponding conjugate strain measures are therefore $\lambda_n - 1$, λ_t and $\lambda_\vartheta - 1$.

The remaining conjugate strain measures can be determined by examining their variations in (2.6.11). Denoting $\delta\kappa_n$ as the variation of the strain measure conjugate to M^{nn}, and $\delta\kappa_\vartheta$ that of $M^{\vartheta\vartheta}$, one can show that the corresponding conjugate strain measures are

$$\kappa_n = -\psi' \ , \qquad \kappa_\vartheta = \frac{\cos(\psi+\alpha)-\cos\alpha}{R} \ . \tag{2.6.16}$$

The term $\cos\alpha$ in the κ_ϑ expression is included so that this strain converges to the appropriate infinitesimal strain in the infinitesimal limit.

In summary, the strain measures $\mathbf{E}$ conjugate to $\mathbf{S}$ in (2.4.29) are

$$\mathbf{E} = \begin{Bmatrix} \lambda_n - 1 \\ \lambda_\vartheta - 1 \\ \kappa_n \\ \kappa_\vartheta \\ \lambda_t \end{Bmatrix} = \begin{Bmatrix} J_o - 1 \\ (u\sin\alpha + w\cos\alpha)/R \\ -\psi' \\ (\cos(\psi+\alpha)-\cos\alpha)/R \\ C_{12} \end{Bmatrix} \tag{2.6.17}$$

2.7. Specialization to membrane theory.

When the thickness of the shell is negligible compared to its radius of curvature, the strain energy contributed by the membrane strains becomes most dominant; the bending and the shear deformations can then be neglected. In this case, the shell theory discussed in the previous sections can be specialized to capture only the membrane action of the shell.

2.7.1. Kinematic description.

Because of the negligible amount of bending and shear deformations that take place in a membrane, the hypothesis of ***straight normal remains straight*** must be augmented with an additional requirement that this straight normal remains normal to the deformed neutral surface. Thus we characterize the deformation with the kinematic variables -- the reference surface displacements $u(X^1)$ and $w(X^1)$. The angle ψ now becomes a function of these two kinematic variables, such that

$$\tan\psi = \frac{w'}{1+u'}. \tag{2.7.1}$$

In addition to $u(X^1)$ and $w(X^1)$, we employ a third kinematic variable $\lambda_h(X^1)$ to characterize the stretching of the thickness of the membrane. This inclusion allows for a broader class of constitutive relations.

Following the same approach outlined in Section 2.3, a point on the membrane after deformation $\mathbf{x} = \Phi(\mathbf{X})$ can be expressed as

$$\mathbf{x} = \Phi(\mathbf{X}) = \Phi_0(X^1,X^3) + \lambda_h(X^1)\Phi_1(X^1,X^2) \tag{2.7.2}$$

where Φ_0 and Φ_1 are defined in (2.3.2) and (2.3.3).

The deformation gradient $\mathbf{F}$ for this deformation map in (2.7.2) is

$$\left[F^{\alpha}{}_{A}\right] = \begin{bmatrix} 1+u'-X^2(\lambda_h\psi'\cos\psi+\lambda_h'\sin\psi) & -\lambda_h\sin\psi & 0 \\ w'-X^2(\lambda_h\psi'\sin\psi-\lambda_h'\cos\psi) & \lambda_h\cos\psi & 0 \\ 0 & 0 & 1 \end{bmatrix}. \tag{2.7.3}$$

where a prime denotes differentiation with respect to X^1.

The corresponding right Cauchy-Green tensor **C** is

$$\left[C^A{}_B\right] = \begin{bmatrix} (1+u')^2+(w')^2 & 0 & 0 \\ 0 & \lambda_h{}^2 & 0 \\ 0 & 0 & \dfrac{r^2}{R^2} \end{bmatrix}. \tag{2.7.4}$$

The above uses the relation (2.7.1) and the fact that the thickness h is much less than the characteristic length of the membrane L. Since the matrix **C** is already in a diagonal form, the three principal stretches are just the square roots of the corresponding diagonal elements of **C**. Following the naming convention used before, we denote λ_n as the stretch along the direction of $\hat{\mathbf{n}}$; λ_ϑ as that in the hoop direction; and λ_h as the stretch of the thickness of the membrane, where

$$\lambda_n = \sqrt{(1+u')^2+w'^2} = (1+u')\cos\psi+w'\sin\psi\,, \qquad \lambda_\vartheta = \frac{r}{R}\,. \tag{2.7.5}$$

2.7.2. Equilibrium equations.

The stress resultants V^{ni}, M^{nn}, and $M^{\vartheta\vartheta}$ vanish in the case of a membrane. The external loading is resisted by the membrane forces N^{nn} and $N^{\vartheta\vartheta}$ only. Thus the stress resultants **S** take the form

$$\mathbf{S} = [N^{nn} \;\; N^{\vartheta\vartheta}]^T \tag{2.7.6}$$

where the definitions of N^{nn} and $N^{\vartheta\vartheta}$ are given in Box 2.4.1. Because of this, the balance of forces in (2.5.7) becomes:

$$\frac{1}{R}\frac{\partial}{\partial X^1}\begin{Bmatrix} R\cos\psi N^{nn} \\ R\sin\psi N^{nn} \end{Bmatrix} - \frac{N^{\vartheta\vartheta}}{R}\begin{Bmatrix}\sin\alpha \\ \cos\alpha\end{Bmatrix} + \begin{Bmatrix} p^1(X^1) \\ p^2(X^1)\end{Bmatrix} = \begin{Bmatrix}0\\0\end{Bmatrix}, \tag{2.7.7}$$

while the balance of moments in (2.5.12) reduces to the result $C^{12}=0$, in agreement to (2.7.1).

2.7.3. Conjugate strain measures.

The analogous treatment of Secton 2.6 results in an energy expression in the form (2.6.10). There are additional terms involving the stretch of the thickness λ_h. Associated with these terms are the moments and shear, which vanish for the membrane case. Also associated with the terms containing λ_h is a pinching force acting normal to the membrane surface. This term also vanish since the membrane is in a state of plane stress. Thus the stretch λ_h has no contributions to the strain energy stored in the system. The strain measures conjugate to the stress resultants $\mathbf{S}$ in (2.7.6) are therefore

$$\mathbf{E} = \begin{Bmatrix} \lambda_n - 1 \\ \lambda_\theta - 1 \end{Bmatrix} = \begin{Bmatrix} J_a - 1 \\ (u\sin\alpha + w\cos\alpha)/R \end{Bmatrix} \tag{2.7.8}$$

2.8. Constitutive relations.

Several constitutive relations will be presented herein. Based on the strain measures $\mathbf{E}$ defined in (2.6.17) for the shell and (2.7.8) for the membrane, and the stress resultants summarized in Box 2.4.1, constitutive equations for the case of hyperelasticity are formulated. The specialization to the membrane allows the implementation of the Mooney-Rivlin material. Finally, a viscoelastic constitutive model developed in terms of these strain measures $\mathbf{E}$ are formulated.

2.8.1. Hyperelastic material.

It is assumed in hyperelasticity that the stress resultants $\mathbf{S}$ are derivable from a potential $W(X^1,\mathbf{E})$ such that

$$\mathbf{S} = \frac{\partial W(X^1,\mathbf{E})}{\partial \mathbf{E}} \tag{2.8.1}$$

"Linear" material. One constitutive relation that satisfies (2.8.1), henceforth referred to as the *"linear"* material, has a potential of the form

$$W(X^1,\mathbf{E}) = \frac{Eh}{2(1-\nu^2)}\left\{(\lambda_n-1)^2 + (\lambda_\vartheta-1)^2 + 2\nu(\lambda_n-1)(\lambda_\vartheta-1)\right\} \tag{2.8.2}$$

$$+ \frac{Eh^3}{24(1-\nu^2)}\left\{\kappa_n{}^2 + \kappa_\vartheta{}^2 + 2\nu\kappa_n\kappa_\vartheta\right\} + \frac{\kappa Gh}{2}\lambda_l{}^2$$

where the parameters E, G, h, ν and κ are the Young's and the shear moduli, the thickness of the shell, the Poisson's ratio, and the shear coefficient, respectively. From this, the generalized stress-strain relation takes the form

$$\mathbf{S} = \mathbf{D}\mathbf{E} \tag{2.8.3}$$

where

$$\mathbf{D} = \frac{Eh}{(1-\nu^2)}\begin{bmatrix} 1 & \nu & 0 & 0 & 0 \\ \nu & 1 & 0 & 0 & 0 \\ 0 & 0 & h^2/12 & \nu h^2/12 & 0 \\ 0 & 0 & \nu h^2/12 & h^2/12 & 0 \\ 0 & 0 & 0 & 0 & \kappa G\left(\frac{1-\nu^2}{E}\right) \end{bmatrix}. \tag{2.8.4}$$

In the case of a membrane, only the terms containing λ_n and λ_ϑ in (2.8.2) are retained. The constitutive matrix $\mathbf{D}$ now becomes

$$\mathbf{D} = \frac{Eh}{(1-\nu^2)}\begin{bmatrix} 1 & \nu \\ \nu & 1 \end{bmatrix}. \tag{2.8.5}$$

Mooney-Rivlin material. We shall only formulate the *Mooney-Rivlin* material for the membrane theory. Here, the material is assumed to be incompressible and the membrane is considered to be in a state of plane stress.

For this material, the potential $W(X^1,\mathbf{E})$ takes the form

$$W = W(X^1,C_1,C_2) = hA_1(C_1-3) + hA_2(C_2-3) \tag{2.8.6}$$

where C_1 and C_2 are the invariants of the right Cauchy-Green tensor, A_1 and A_2 are material constants, and h is the thickness of the membrane. Using the form of $\mathbf{C}$ for membranes in (2.7.4),

$$C_1 = C^A{}_A = \lambda_n{}^2 + \lambda_h{}^2 + \lambda_\vartheta{}^2 \tag{2.8.7}$$

$$C_2 = -\tfrac{1}{2}(C^I{}_J C^I{}_J - C^I{}_I C^J{}_J) = \lambda_n{}^2\lambda_h{}^2 + \lambda_n{}^2\lambda_\vartheta{}^2 + \lambda_h{}^2\lambda_\vartheta{}^2$$

To incorporate the incompressibility condition $\lambda_n\lambda_\vartheta\lambda_h = 1$, we modify the strain energy potential W by adding in the constraint condition, so that

$$\overline{W}(X^1, C_1, C_2) = W(X^1, C_1, C_2) + p(1-\lambda_n\lambda_\vartheta\lambda_h) \tag{2.8.8}$$

Here, the parameter p is the Lagrangian multiplier. From (2.8.8), the stress resultants can now be determined:

$$N^{nn} = \frac{\partial \overline{W}}{\partial \lambda_n} = 2h\lambda_n\left\{A_1 + A_2(\lambda_h{}^2+\lambda_\vartheta{}^2)\right\} - p/\lambda_n \tag{2.8.9}$$

$$N^{\vartheta\vartheta} = \frac{\partial \overline{W}}{\partial \lambda_\vartheta} = 2h\lambda_\vartheta\left\{A_1 + A_2(\lambda_h{}^2+\lambda_n{}^2)\right\} - p/\lambda_\vartheta$$

Enforcing the plane stress condition, i.e. $\frac{\partial \overline{W}}{\partial \lambda_h} = 0$, will give the Lagrangian multiplier p:

$$p = 2h\lambda_h{}^2\left\{A_1 + A_2(\lambda_n{}^2+\lambda_\vartheta{}^2)\right\} \tag{2.8.10}$$

Combining (2.8.9) and (2.8.10) gives the relations

$$N^{nn} = \frac{2hA_1}{\lambda_n}(\lambda_n{}^2 - \lambda_h{}^2)\left(1 + \frac{A_2}{A_1}\lambda_\vartheta{}^2\right) \tag{2.8.11a}$$

$$N^{\vartheta\vartheta} = \frac{2hA_1}{\lambda_\vartheta}(\lambda_\vartheta{}^2 - \lambda_h{}^2)\left(1 + \frac{A_2}{A_1}\lambda_n{}^2\right) \tag{2.8.11b}$$

Although the results in (2.8.11) may appear at first glance to be different from those recorded in the literature (see Green and Adkins [1960]), they are in

fact identical results. One should recall that the stress resultants derived here are the *first Piola-Kirchhoff* type, which are different from the *Cauchy* type stress resultants workers often use.

2.8.2. Viscoelastic material.

We first establish the appropriate measures of the stress and strain rates. For this we rewrite the moving frame quantities $\mathbf{S}$ and $\mathbf{E}$ as $\mathbf{S}_m$ and $\mathbf{E}_m$, such that

$$\mathbf{S}_m = \begin{Bmatrix} N^{\theta\theta} \\ V^{nl} \\ N^{\theta\theta} \\ M^{\theta\theta} \\ 0 \\ M^{\theta\theta} \end{Bmatrix}, \qquad \mathbf{E}_m = \begin{Bmatrix} \lambda_n - 1 \\ \lambda_l \\ \lambda_\theta - 1 \\ \kappa_n \\ 0 \\ \kappa_\theta \end{Bmatrix}. \tag{2.8.12}$$

Equation (2.8.3) now reads as

$$\mathbf{S}_m = \mathbf{D}_m \mathbf{E}_m \tag{2.8.13}$$

where elements of $\mathbf{D}$ are reordered to form $\mathbf{D}_m$. These stress and strain quantities $\mathbf{S}_m$ and $\mathbf{E}_m$ in the *moving* frame can be expressed in terms of their counterparts $\mathbf{S}_f$ and $\mathbf{E}_f$ in the *fixed* spatial frame, such that

$$\mathbf{S}_f = \mathbf{T}(\psi)\mathbf{S}_m\,, \qquad \mathbf{E}_f = \mathbf{T}(\psi)\mathbf{E}_m \tag{2.8.14}$$

where $\mathbf{T}(\psi)$ is a transformation matrix constructed based on $\mathbf{\Lambda}(\psi)$ in (2.3.13):

$$\mathbf{T}(\psi) = \begin{bmatrix} \mathbf{\Lambda}(\psi) & \mathbf{0} \\ \mathbf{0} & \mathbf{\Lambda}(\psi) \end{bmatrix}.$$

Equation (2.8.13) can then be written as

$$\mathbf{T}^T \mathbf{S}_f = \mathbf{D}_m \mathbf{T}^T \mathbf{E}_f \tag{2.8.15}$$

Taking the time derivative of (2.8.15) and making use of the identity $\mathbf{T}\mathbf{T}^T = \mathbf{I}$, one obtains

$$\mathbf{T}^T(\dot{\mathbf{S}}_f - \dot{\mathbf{T}}\mathbf{T}^T\mathbf{S}_f) = \mathbf{D}_m\,\mathbf{T}^T(\dot{\mathbf{E}}_f - \dot{\mathbf{T}}\mathbf{T}^T\mathbf{E}_f) \tag{2.8.16a}$$

$$\dot{\mathbf{S}}_f - \dot{\mathbf{T}}\mathbf{T}^T\mathbf{S}_f = \mathbf{T}\mathbf{D}_m\,\mathbf{T}^T(\dot{\mathbf{E}}_f - \dot{\mathbf{T}}\mathbf{T}^T\mathbf{E}_f) \tag{2.8.16b}$$

From (2.8.16), we can define the stress rates $\overset{\blacksquare}{\mathbf{S}}_m$ and $\overset{\blacksquare}{\mathbf{S}}_f$ as

$$\overset{\blacksquare}{\mathbf{S}}_f = \dot{\mathbf{S}}_f - \dot{\mathbf{T}}\mathbf{T}^T\mathbf{S}_f\,, \qquad \overset{\blacksquare}{\mathbf{S}}_m = \mathbf{T}^T\overset{\blacksquare}{\mathbf{S}}_f \tag{2.8.17a}$$

and the corresponding strain rate $\overset{\blacksquare}{\mathbf{E}}_m$ and $\overset{\blacksquare}{\mathbf{E}}_f$ as

$$\overset{\blacksquare}{\mathbf{E}}_f = \dot{\mathbf{E}}_f - \dot{\mathbf{T}}\mathbf{T}^T\mathbf{E}_f\,, \qquad \overset{\blacksquare}{\mathbf{E}}_m = \mathbf{T}^T\overset{\blacksquare}{\mathbf{E}}_f \tag{2.8.17b}$$

such that

$$\overset{\blacksquare}{\mathbf{S}}_m = \mathbf{D}_m\overset{\blacksquare}{\mathbf{E}}_m\,, \qquad \overset{\blacksquare}{\mathbf{S}}_f = \mathbf{T}\mathbf{D}_m\mathbf{T}^T\overset{\blacksquare}{\mathbf{E}}_f\,. \tag{2.8.18}$$

Taking the derivative of (2.8.14), rewritten as $\mathbf{S}_m = \mathbf{T}^T(\psi)\mathbf{S}_f$, we find that the stress rate $\overset{\blacksquare}{\mathbf{S}}_m$ is simply the material time derivative of $\mathbf{S}_m$. Both $\overset{\blacksquare}{\mathbf{S}}_m$ and $\overset{\blacksquare}{\mathbf{S}}_f$ are objective rates; moreover, $\overset{\blacksquare}{\mathbf{S}}_m$ has the stronger property of being invariant under superposed rigid body motion (Simo *et al* [1983]). This same conclusion holds for the strain rate.

We propose here a viscoelastic model that is defined by the rate equation

$$\mathbf{S} = \int_0^t \mathbf{D}(t-\tau)\,\overset{\blacksquare}{\mathbf{E}}(\tau)\,d\tau \tag{2.8.19}$$

where t denotes time; the components of $\mathbf{S}$ and $\mathbf{E}$ (subscript m implied) are now arranged as in (2.4.29) and (2.6.17), respectively; and

$$\mathbf{D}(t) = \frac{E_{ve}(t)\,h}{(1-\nu^2)}\begin{bmatrix} 1 & \nu & 0 & 0 & 0 \\ \nu & 1 & 0 & 0 & 0 \\ 0 & 0 & h^2/12 & \nu h^2/12 & 0 \\ 0 & 0 & \nu h^2/12 & h^2/12 & 0 \\ 0 & 0 & 0 & 0 & \kappa G\left(\dfrac{1-\nu^2}{E_{ve}(t)}\right) \end{bmatrix}. \tag{2.8.20}$$

Here, the viscoelastic material assumes the behavior of a ***standard solid*** model, so that E_{ve} takes the form:

$$E_{ve} = E_l + (E_s - E_l)e^{-\beta t} \,. \tag{2.8.21}$$

2.9. Solution procedure. The finite element method.

Box 2.9.1. Summary of Equations for Axisymmetric Shell/Membrane*.

Equations	Shell theory	Membrane theory
kinematic variables	$\mathbf{w} = [u \;\; w \;\; \psi]^T$	$\mathbf{w} = [u \;\; w]^T$
Strains	$\mathbf{E} = \begin{Bmatrix} \lambda_n - 1 \\ \lambda_\theta - 1 \\ \kappa_n \\ \kappa_\theta \\ \lambda_l \end{Bmatrix} = \begin{Bmatrix} J_o - 1 \\ (u\sin\alpha + w\cos\alpha)/R \\ -\psi' \\ (\cos(\psi+\alpha) - \cos\alpha)/R \\ C_{12} \end{Bmatrix}$	$\mathbf{E} = \begin{Bmatrix} \lambda_n - 1 \\ \lambda_\theta - 1 \end{Bmatrix} = \begin{Bmatrix} J_o - 1 \\ (u\sin\alpha + w\cos\alpha)/R \end{Bmatrix}$
Stress resultants	$\mathbf{S} = [N^{nn} \;\; N^{\theta\theta} \;\; M^{nn} \;\; M^{\theta\theta} \;\; V^{nl}]^T$	$\mathbf{S} = [N^{nn} \;\; N^{\theta\theta}]^T$
Equil. Eq.	$\frac{1}{R}\frac{\partial}{\partial X^1}\left[R\mathbf{A}\begin{Bmatrix} N^{nn} \\ V^{nl} \end{Bmatrix}\right] - \frac{N^{\theta\theta}}{R}\begin{Bmatrix} \sin\alpha \\ \cos\alpha \end{Bmatrix} + \begin{Bmatrix} p^1 \\ p^2 \end{Bmatrix} = \begin{Bmatrix} 0 \\ 0 \end{Bmatrix}$ $\frac{1}{R}\frac{\partial(M^{nn}R)}{\partial X^1} + C_{12}N^{nn} - J_o V^{nl} - \frac{M^{\theta\theta}}{R}\sin(\psi+\alpha) = 0$	$\frac{1}{R}\frac{\partial}{\partial X^1}\begin{Bmatrix} R\cos\psi N^{nn} \\ R\sin\psi N^{nn} \end{Bmatrix}$ $-\frac{N^{\theta\theta}}{R}\begin{Bmatrix} \sin\alpha \\ \cos\alpha \end{Bmatrix} + \begin{Bmatrix} p^1 \\ p^2 \end{Bmatrix} = \begin{Bmatrix} 0 \\ 0 \end{Bmatrix}$
Constit. Eq.	"Linear" material $\mathbf{S} = \mathbf{D}\mathbf{E}$ Viscoelastic material $\mathbf{S} = \int_0^t \mathbf{D}(t-\tau)\dot{\mathbf{E}}(\tau)\,d\tau$	"Linear" material $\mathbf{S} = \mathbf{D}\mathbf{E}$ Viscoelastic material $\mathbf{S} = \int_0^t \mathbf{D}(t-\tau)\dot{\mathbf{E}}(\tau)\,d\tau$ Mooney-Rivlin material $\mathbf{S} = \hat{\mathbf{S}}(\mathbf{E})$
Boundary conditions	$\mathbf{w} = \tilde{\mathbf{w}}$ at displacement boundaries $\partial_{\mathbf{w}}$ $\mathbf{S} = \hat{\mathbf{S}}$ at traction boundaries $\partial_{\mathbf{S}}$ $\partial_{\mathbf{w}} \cup \partial_{\mathbf{S}} = 0$	

The equilibrium equations, the kinematic description, and the constitutive relations given previously form the set of equations governing the response of

an axisymmetric shell subjected to axisymmetric torsionless loading. These equations, including the boundary conditions, are summarized in Box 2.9.1.

The solution procedure for these equations is presented here. We circumvent the shear locking effect common in finite element analyses of beams, plates and shells by employing a mixed method† based on the Reissner-Hellinger variational formulation (Reissner [1950a]). In contrast to the displacement type formulation in which the constitutive equations are enforced to hold strongly (pointwise), this mixed method assumes these equations to be satisfied in a weak (weighted) sense. Accordingly, we construct the weak form of the equilibrium equations as in the displacement type formulation, and augment it with the weak form of the constitutive equations.

Because of the geometrical nonlinearity due to the large deformation, and the additional nonlinearity due to the material behavior, these two weak forms are generally nonlinear scalar differential equations. Consistent linearization procedures, as described in Hughes and Pister [1978], are employed to obtain the linear parts of these weak forms. The resulting equations are then readily adapted to an incremental formulation. For this mixed formulation, an additional step is required to *condense* out the stress variables, so that the final set of algebraic equations is expressed entirely in terms of the displacement variables.

• $J_0 = (1+u')\cos\psi + w'\sin\psi$,
$C_{12} = -(1+u')\sin\psi + w'\cos\psi$,
$\Lambda(X^1) = \begin{bmatrix} \cos\psi & -\sin\psi \\ \sin\psi & \cos\psi \end{bmatrix}$.

† Other applications of the mixed formulations in finite element analyses can be found in Pian [1983].

2.9.1. Admissible variations. Weak forms of equilibrium and constitutive equations.

2.9.1.1. Admissible variations.

The mixed formulation treats both the displacements $\mathbf{w}$ and the stress resultants $\mathbf{S}$ as independent variables. Thus, a configuration in this case has to be described by the pair $(\mathbf{w},\mathbf{S})$. We select the admissible displacement variations $\delta\mathbf{w}$ and the admissible stress variations $\delta\mathbf{S}$ to be arbitrary, with the requirement that $\delta\mathbf{w}$ vanish at the displacement boundary $\partial_{\mathbf{w}}$.

2.9.1.2. Weak form of the equilibrium equations.

We specialize here to the case of the shell, and report only the final result for the membrane case, which are derived in an analogous manner. Let $G(\mathbf{w},\mathbf{S},\delta\mathbf{w})$ represent the weak form of the equilibrium equations for a structure modeled by a number of elements, and let $G_e(\mathbf{w},\mathbf{S},\delta\mathbf{w})$ represent the contribution from each element. We denote the assembly operator over all the elements by $\sum_e$, such that

$$G(\mathbf{w},\mathbf{S},\delta\mathbf{w}) = \sum_e G_e(\mathbf{w},\mathbf{S},\delta\mathbf{w}) = 0 . \tag{2.9.1}$$

Multiplying the equilibrium equations in (2.5.7) and (2.5.12) by the corresponding variations $\delta\mathbf{w}$, we obtain the weak form for each element as follows:

$$G_e(\mathbf{w},\mathbf{S},\delta\mathbf{w}) = 2\pi \int_0^L \left\{ [\delta u \;\; \delta w] \left(\frac{1}{R}\frac{\partial}{\partial X^1}[R\Lambda(\psi)\begin{Bmatrix} N^{mn} \\ V^{nl} \end{Bmatrix}] - \frac{N^{\theta\theta}}{R}\begin{Bmatrix} \sin\alpha \\ \cos\alpha \end{Bmatrix} + \begin{Bmatrix} p^1 \\ p^2 \end{Bmatrix} \right) \right.$$

$$\left. + \delta\psi \left(\frac{1}{R}\frac{\partial(M^{mn}R)}{\partial X^1} + C_{12}N^{mn} - J_o V^{nl} - \frac{M^{\theta\theta}}{R}\sin(\psi+\alpha) \right) \right\} R dX^1 .$$

When integration by part is carried out, the above becomes

$$G_e(\mathbf{w},\mathbf{S},\delta\mathbf{w}) = -2\pi\int_0^L \left\{ [\delta u' \ \delta w'] \mathbf{A}(\psi) \begin{Bmatrix} N^{nn} \\ V^{nt} \end{Bmatrix} + [\delta u \ \delta w] \left[\frac{N^{\theta\theta}}{R} \begin{Bmatrix} \sin\alpha \\ \cos\alpha \end{Bmatrix} - \begin{Bmatrix} p^1 \\ p^2 \end{Bmatrix} \right] \right. \tag{2.9.2}$$

$$\left. - \delta\psi' M^{nn} + \delta\psi \left[C_{12} N^{nn} - J_o V_{nt} - M^{\theta\theta} \frac{\sin(\psi+\alpha)}{R} \right] \right\} R dX^1 + 2\pi \delta\mathbf{w}^T \tilde{\mathbf{P}}$$

where $\tilde{\mathbf{P}} = [\cos\psi \tilde{N}^{nn} - \sin\psi \tilde{V}^{nt}, \ \sin\psi \tilde{N}^{nn} + \cos\psi \tilde{V}^{nt}, \ -\tilde{M}^{nn}]^T|_{\partial_{\mathbf{S}}}$ is the prescribed tractions over the boundary $\partial_{\mathbf{S}}$. By defining $\delta\mathbf{W}$, $\mathbf{P}$ and $\mathbf{A}$ as

$$\delta\mathbf{W} \equiv [\delta\mathbf{w} \ \delta\mathbf{w}']^T, \qquad \mathbf{P} \equiv [p^1 \ p^2 \ 0 \ 0 \ 0 \ 0]^T, \tag{2.9.3a}$$

$$\mathbf{A} \equiv \begin{bmatrix} 0 & \sin\alpha/R & 0 & 0 & 0 \\ 0 & \cos\alpha/R & 0 & 0 & 0 \\ C_{12} & 0 & 0 & -\sin(\psi+\alpha)/R & -J_o \\ \cos\psi & 0 & 0 & 0 & -\sin\psi \\ \sin\psi & 0 & 0 & 0 & \cos\psi \\ 0 & 0 & -1 & 0 & 0 \end{bmatrix}, \tag{2.9.3b}$$

equation (2.9.2) takes the form

$$G_e(\mathbf{w},\mathbf{S},\delta\mathbf{w}) = -2\pi\int_0^L \delta\mathbf{W}^T [\mathbf{AS} - \mathbf{P}] R dX^1 + 2\pi\delta\mathbf{w}^T\tilde{\mathbf{P}}. \tag{2.9.3c}$$

2.9.1.3. Weak form of the constitutive equations.

Let the weak form of the constitutive equations for the structure be represented by $H(\mathbf{w},\mathbf{S},\delta\mathbf{S})$, and let $H_e(\mathbf{w},\mathbf{S},\delta\mathbf{S})$ represent the contribution from each element. Similar to (2.9.1)

$$H(\mathbf{w},\mathbf{S},\delta\mathbf{S}) = \sum_e H_e(\mathbf{w},\mathbf{S},\delta\mathbf{S}) = 0 \tag{2.9.4}$$

In what follows, we shall treat each constitutive model discussed in Section 2.8 separately.

"Linear" material. For this material,

$$\mathbf{S} = \mathbf{DE} \tag{2.8.3}$$

where **S**, **E** and **D** take on their respective forms for the shell and the membrane cases in Box 2.9.1 and Section 2.8. The corresponding weak form equals

$$H_e(\mathbf{w},\mathbf{S},\delta\mathbf{S}) = 2\pi\int_0^L \delta\mathbf{S}^T[\mathbf{E}-\mathbf{D}^{-1}\mathbf{S}]RdX^1 \,. \tag{2.9.5}$$

Mooney-Rivlin material. We shall express the constitutive relation for this material in (2.8.11) as

$$\mathbf{S} = \hat{\mathbf{S}}(\mathbf{E}) \tag{2.9.6}$$

where **E** now represents the stretches $[\lambda_n\ \lambda_\theta]^T$. By casting this constitutive relation in its incremental form

$$\Delta\mathbf{S} = \mathbf{D}(\mathbf{E})\Delta\mathbf{E} \,. \tag{2.9.7}$$

we can formulate the corresponding weak form as

$$H_e(\mathbf{w},\mathbf{S},\delta\mathbf{S}) = 2\pi\int_0^L \delta\mathbf{S}^T\mathbf{D}^{-1}[\hat{\mathbf{S}}(\mathbf{E})-\mathbf{S}]RdX^1 \,. \tag{2.9.8}$$

Viscoelastic material. Since this constitutive model is rate dependent, the solution procedure involves first the temporal discretization of its rate form, (2.8.19). First we combine (2.8.19) through (2.8.21) to give

$$\mathbf{S}(t) = \mathbf{D}_l\mathbf{E}(t) + (\mathbf{D}_s-\mathbf{D}_l)e^{-\beta t}\mathbf{E}(0) + \int_{0^+}^{t}(\mathbf{D}_s-\mathbf{D}_l)e^{-\beta(t-\tau)}\dot{\mathbf{E}}(\tau)\,d\tau \,, \tag{2.9.9}$$

where now **E** and **S** are functions of time t, $\mathbf{D}_l \equiv \frac{E_l}{E_{ve}}\mathbf{D}$ and $\mathbf{D}_s \equiv \frac{E_s}{E_{ve}}\mathbf{D}$. To integrate the last member of (2.9.9), we consider the discrete time interval $[t_n, t_{n+1}]$, where $t_{n+1} = t_n + \Delta t$. Accordingly, we write the response quantities as

$$\mathbf{S}_{n+1} = \mathbf{S}_n + \Delta\mathbf{S} \,, \qquad \mathbf{E}_{n+1} = \mathbf{E}_n + \Delta\mathbf{E} \tag{2.9.10}$$

where the subscripts n and $n+1$ refer to the functions at t_n and t_{n+1}, respectively, and Δ denotes the increment of the function over this time increment.

Next we define

$$\mathbf{I}_n \equiv e^{-\beta t_n}\mathbf{E}(0) + \int_{0^+}^{t_n} e^{-\beta(t_n-\tau)}\,\dot{\mathbf{E}}(\tau)\,d\tau\,, \tag{2.9.11a}$$

$$\Delta\mathbf{I} \equiv \int_{t_n}^{t_{n+1}} e^{-\beta(t_{n+1}-\tau)}\,\dot{\mathbf{E}}(\tau)\,d\tau\,, \tag{2.9.11b}$$

so that the following recursive relation holds

$$\mathbf{I}_{n+1} = e^{-\beta\Delta t}\,\mathbf{I}_n + \Delta\mathbf{I}\,. \tag{2.9.11c}$$

Using the above definitions, and replacing t in (2.9.9) by t_{n+1} and t_n results in the following two expressions:

$$\mathbf{S}_{n+1} = \mathbf{D}_l\,\mathbf{E}_{n+1} + (\mathbf{D}_s - \mathbf{D}_l)\,\mathbf{I}_{n+1} \tag{2.9.12a}$$

$$\mathbf{S}_n = \mathbf{D}_l\,\mathbf{E}_n + (\mathbf{D}_s - \mathbf{D}_l)\,\mathbf{I}_n \tag{2.9.12b}$$

Subtracting (2.9.12b) from (2.9.12a) gives an incremental stress-strain relation

$$\Delta\mathbf{S} = \mathbf{D}_l\,\Delta\mathbf{E} + (\mathbf{D}_s - \mathbf{D}_l)\,\Delta\mathbf{I} \tag{2.9.13}$$

The integral $\Delta\mathbf{I}$ in (2.9.13) can be approximated by the use of the mean value theorem and the mid-point rule, which gives

$$\Delta\mathbf{I} \approx \frac{1-e^{-\beta\Delta t}}{\beta\Delta t}\Delta\mathbf{E}\,.$$

Therefore

$$\Delta\mathbf{S} = \mathbf{D}_{vs}\,\Delta\mathbf{E} \tag{2.9.14a}$$

where

$$\mathbf{D}_{vs} \approx \mathbf{D}_l + \left(\frac{1-e^{-\beta\Delta t}}{\beta\Delta t}\right)(\mathbf{D}_s - \mathbf{D}_l)\,. \tag{2.9.14b}$$

By writing (2.8.19) as $\mathbf{S} = \widehat{\mathbf{S}}(\mathbf{E})$, the corresponding weak form becomes

$$H_s(\mathbf{w},\mathbf{S},\delta\mathbf{S}) = 2\pi\int_0^L \delta\mathbf{S}^T\mathbf{D}_{vs}^{-1}[\widehat{\mathbf{S}}(\mathbf{E}) - \mathbf{S}]\,R dX^1\,. \tag{2.9.15}$$

2.9.2. Consistent linearization.

We carry out the linearization procedures so that the nonlinear problem can be cast into an incremental formulation for computational purpose. First, we designate the current configuration as a composition of an intermediate configuration denoted by the pair $(\bar{\mathbf{w}},\bar{\mathbf{S}})$ and a superposed motion denoted by $(\Delta\mathbf{w},\Delta\mathbf{S})$. In the following, the quantity $\bar{(\cdot)}$ denotes $(\cdot)$ as evaluated at the intermediate configuration.

The linear part of the weak form $G(\mathbf{w},\mathbf{S},\delta\mathbf{w})$ at the intermediate configuration $(\bar{\mathbf{w}},\bar{\mathbf{S}})$ is defined by

$$L[G]_{(\bar{\mathbf{w}},\bar{\mathbf{S}})} = G(\bar{\mathbf{w}},\bar{\mathbf{S}},\delta\mathbf{w}) + \mathbf{D}_1 G(\bar{\mathbf{w}},\bar{\mathbf{S}},\delta\mathbf{w})\cdot\Delta\mathbf{w} + \mathbf{D}_2 G(\bar{\mathbf{w}},\bar{\mathbf{S}},\delta\mathbf{w})\cdot\Delta\mathbf{S} \quad (2.9.16a)$$

where the differentials $\mathbf{D}_1 G$ and $\mathbf{D}_2 G$ can be computed from the definition of the directional derivative:

$$\mathbf{D}_1 G(\bar{\mathbf{w}},\bar{\mathbf{S}},\delta\mathbf{w})\cdot\Delta\mathbf{w} = \frac{d}{d\varepsilon}\Big[G(\bar{\mathbf{w}}+\varepsilon\Delta\mathbf{w},\bar{\mathbf{S}},\delta\mathbf{w})\Big]_{\varepsilon=0}. \quad (2.9.16b)$$

$$\mathbf{D}_2 G(\bar{\mathbf{w}},\bar{\mathbf{S}},\delta\mathbf{w})\cdot\Delta\mathbf{S} = \frac{d}{d\varepsilon}\Big[G(\bar{\mathbf{w}},\bar{\mathbf{S}}+\varepsilon\Delta\mathbf{S},\delta\mathbf{w})\Big]_{\varepsilon=0}. \quad (2.9.16c)$$

The linear part for $H(\mathbf{w},\mathbf{S},\delta\mathbf{w})$ can be obtained in the same manner. The linearized version of equations (2.9.1) and (2.9.4) are

$$L[G]_{(\bar{\mathbf{w}},\bar{\mathbf{S}})} = \sum_e L[G_e]_{(\bar{\mathbf{w}},\bar{\mathbf{S}})} = 0 \quad (2.9.17a)$$

$$L[H]_{(\bar{\mathbf{w}},\bar{\mathbf{S}})} = \sum_e L[H_e]_{(\bar{\mathbf{w}},\bar{\mathbf{S}})} = 0 \quad (2.9.17b)$$

2.9.2.1. Linearization. Equilibrium equations.

We denote that $\Delta\mathbf{W} \equiv [\Delta\mathbf{w}\ \Delta\mathbf{w}']^T$. Substituting (2.9.3c) into (2.9.16) gives

$$L[G_e]_{(\bar{\mathbf{w}},\bar{\mathbf{S}})} = -2\pi\int_0^L \delta\mathbf{W}^T\Big[\overline{\mathbf{AS}} - \mathbf{P} + \bar{\mathbf{A}}_g\Delta\mathbf{W} + \bar{\mathbf{A}}\Delta\mathbf{S}\Big]\,R dX^1 + 2\pi\delta\mathbf{w}^T\tilde{\mathbf{P}} \quad (2.9.18)$$

where the matrix $\bar{\mathbf{A}}_g$ takes the form

$$\bar{\mathbf{A}}_g \equiv \begin{bmatrix} 0 & 0 & 0 & 0 & 0 & 0 \\ 0 & 0 & 0 & 0 & 0 & 0 \\ 0 & 0 & \bar{A}_g{}^{33} & \bar{A}_g{}^{34} & \bar{A}_g{}^{35} & 0 \\ 0 & 0 & \bar{A}_g{}^{34} & 0 & 0 & 0 \\ 0 & 0 & \bar{A}_g{}^{35} & 0 & 0 & 0 \\ 0 & 0 & 0 & 0 & 0 & 0 \end{bmatrix}; \quad \begin{aligned} \bar{A}_g{}^{33} &\equiv -\bar{J}_o \bar{N}^{nn} - \bar{C}_{12} \bar{V}^{nl} - \frac{\cos(\bar{\psi}+\alpha)\bar{M}^{\theta\theta}}{R} \\ \bar{A}_g{}^{34} &\equiv -\sin\bar{\psi}\bar{N}^{nn} - \cos\bar{\psi}\bar{V}^{nl} \\ \bar{A}_g{}^{35} &\equiv \cos\bar{\psi}\bar{N}^{nn} - \sin\bar{\psi}\bar{V}^{nl} \end{aligned} .$$

2.9.2.2. Linearization. Constitutive equations.

We linearize the weak form of the constitutive equations following definition (2.9.16).

"Linear" material. From (2.9.5),

$$L[H_e]_{(\mathbf{w},\mathbf{S})} = 2\pi \int_0^L \delta\mathbf{S}^T \left[\bar{\mathbf{E}} - \mathbf{D}^{-1}\bar{\mathbf{S}} + \bar{\mathbf{A}}^T \Delta\mathbf{W} - \mathbf{D}^{-1}\Delta\mathbf{S} \right] R dX^1 . \tag{2.9.19}$$

Mooney-Rivlin material. From (2.9.7) and (2.9.8),

$$L[H_e]_{(\mathbf{w},\mathbf{S})} = 2\pi \int_0^L \delta\mathbf{S}^T \left[\mathbf{D}^{-1}(\bar{\mathbf{E}})[\hat{\mathbf{S}}(\bar{\mathbf{E}}) - \bar{\mathbf{S}}] + \Delta\mathbf{E} - \mathbf{D}^{-1}(\bar{\mathbf{E}})\Delta\mathbf{S} \right] R dX^1 \tag{2.9.20}$$

Viscoelastic material. From (2.9.14) and (2.9.15),

$$L[H_e]_{(\mathbf{w},\mathbf{S})} = 2\pi \int_0^L \delta\mathbf{S}^T \left[\mathbf{D}_{ve}{}^{-1}(\bar{\mathbf{E}})[\hat{\mathbf{S}}(\bar{\mathbf{E}}) - \bar{\mathbf{S}}] + \Delta\mathbf{E} - \mathbf{D}_{ve}{}^{-1}(\bar{\mathbf{E}})\Delta\mathbf{S} \right] R dX^1 \tag{2.9.21}$$

2.9.3. Spatial discretization.

The spatial discretization for the mixed finite element method requires some attention regarding the choice of the shape functions. Since the stress variables in (2.9.2) appear without any derivatives, they may be discontinuous across the element boundaries. On the other hand, displacement variables have to be continuous across the element boundaries but not their derivatives.

We therefore interpolate the displacement variables by linear shape functions, and the stress variables by constant values.

$$\delta \mathbf{w} = \sum_{I=1}^{2} h_I \delta \mathbf{w}^h{}_I , \qquad \delta \mathbf{S} = \delta \mathbf{S}^h , \tag{2.9.22a}$$

$$\Delta \mathbf{w} = \sum_{I=1}^{2} h_I \Delta \mathbf{w}^h{}_I , \qquad \Delta \mathbf{S} = \Delta \mathbf{S}^h , \tag{2.9.22b}$$

where the shape functions are $h_1 = 1 - X^1/L$ and $h_2 = X^1/L$, and the superscript h is to denote the discretized values.

In terms of the shape functions in (2.9.22), the kinematic variables $\delta\mathbf{W}$ and $\Delta\mathbf{W}$ read as follows:

$$\begin{aligned} \delta \mathbf{W} &= \sum_{I=1}^{2} \mathbf{B}_I \delta \mathbf{w}^h{}_I \\ \Delta \mathbf{W} &= \sum_{I=1}^{2} \mathbf{B}_I \Delta \mathbf{w}^h{}_I \end{aligned} , \qquad \mathbf{B}_I \equiv \begin{bmatrix} h_I & 0 & 0 \\ 0 & h_I & 0 \\ 0 & 0 & h_I \\ h'_I & 0 & 0 \\ 0 & h'_I & 0 \\ 0 & 0 & h'_I \end{bmatrix} \tag{2.9.23}$$

2.9.3.1. Discretization. Equilibrium equations.

In terms of the shape functions in (2.9.23), the linear part $L[G_e]_{(\mathbf{w},\mathbf{N})}$ in (2.9.18) becomes

$$L[G_e]_{(\mathbf{w}^h,\mathbf{N}^h)} = -2\pi \sum_{I=1}^{2} (\delta \mathbf{w}^h{}_I)^T \left[\bar{\mathbf{R}}^{\mathbf{G}}{}_I + \sum_{J=1}^{2} \bar{\mathbf{K}}^{\mathbf{11}}{}_{IJ} \Delta \mathbf{w}^h{}_J + \bar{\mathbf{K}}^{\mathbf{12}}{}_I \Delta \mathbf{S}^h \right] \tag{2.9.24}$$

where

$$\bar{\mathbf{K}}^{\mathbf{11}}{}_{IJ} \equiv \int_0^L \mathbf{B}_I{}^T \bar{\mathbf{A}}_{\mathbf{g}} \mathbf{B}_J \, R dX^1 , \qquad \bar{\mathbf{K}}^{\mathbf{12}}{}_I \equiv \int_0^L \mathbf{B}_I{}^T \bar{\mathbf{A}} R dX^1 , \tag{2.9.25a}$$

$$\bar{\mathbf{R}}^{\mathbf{G}}{}_I = \bar{\mathbf{K}}^{\mathbf{12}}{}_I \bar{\mathbf{S}} - \mathbf{P}_I - \tilde{\mathbf{P}}_I , \qquad \mathbf{P}_I = \int_0^L \mathbf{B}_I^T \mathbf{P} \, R dX^1 . \tag{2.9.25b}$$

The analogous derivation for the membrane theory also leads to results of the form (2.9.24), where now the matrices $\bar{\mathbf{K}}^{11}{}_{IJ}$ and $\bar{\mathbf{K}}^{12}{}_{I}$ are

$$\bar{\mathbf{K}}^{11}{}_{IJ} \equiv \int_0^L \frac{\bar{N}^{mn} h_{I,1} h_{J,1}}{\sqrt{(1+\bar{u}')^2+\bar{w}'^2}} \begin{bmatrix} \sin^2\bar{\psi} & -\sin\bar{\psi}\cos\bar{\psi} \\ -\sin\bar{\psi}\cos\bar{\psi} & \cos^2\bar{\psi} \end{bmatrix} R dX^1 , \qquad (2.9.26a)$$

$$\bar{\mathbf{K}}^{12}{}_{I} \equiv \int_0^L \begin{bmatrix} h_{I,1}\cos\bar{\psi} & h_I \sin\alpha / R \\ h_{I,1}\sin\bar{\psi} & h_I \cos\alpha / R \end{bmatrix} R dX^1 . \qquad (2.9.26b)$$

2.9.3.2. Discretization. Constitutive equations.

When the shape functions in (2.9.23) are substituted into the expressions for the three constitutive equations in Section 2.9.2.2, we obtain the following result:

$$L[H_e]_{(\bar{\mathbf{w}}^h, \bar{\mathbf{S}}^h)} = 2\pi(\delta \mathbf{S}^h)^T \left[\bar{\mathbf{R}}^H + \sum_{J=1}^{2} \bar{\mathbf{K}}^{21}{}_J \Delta \mathbf{w}^h{}_J + \bar{\mathbf{K}}^{22} \Delta \mathbf{S}^h \right] . \qquad (2.9.27)$$

The matrix $\mathbf{K}^{21} = (\mathbf{K}^{12})^T$, where $\mathbf{K}^{12}$ is defined in (2.9.25a) for the shell, and (2.9.26b) for the membrane. This symmetry condition will lead to a symmetric tangent operator. The matrices $\bar{\mathbf{K}}^{22}$ and $\bar{\mathbf{R}}^H$ for each material are listed below.

"Linear" material. Based on (2.9.19),

$$\bar{\mathbf{K}}^{22} \equiv -\int_0^L \mathbf{D}^{-1} R dX^1 , \qquad \bar{\mathbf{R}}^H \equiv \int_0^L [\mathbf{E}(\bar{\mathbf{w}}^h) - \mathbf{D}^{-1}\bar{\mathbf{S}}^h] R dX^1 . \qquad (2.9.28a)$$

Mooney-Rivlin material. Based on (2.9.20),

$$\bar{\mathbf{K}}^{22} = -\int_0^L \mathbf{D}^{-1}(\bar{\mathbf{w}}^h) R dX^1 , \qquad \bar{\mathbf{R}}^H = \int_0^L \mathbf{D}^{-1}(\bar{\mathbf{w}}^h)[\hat{\mathbf{S}}(\bar{\mathbf{w}}^h) - \bar{\mathbf{S}}^h] R dX^1 . \qquad (2.9.28b)$$

Viscoelastic material. Based on (2.9.21),

$$\bar{\mathbf{K}}^{22} = -\int_0^L \mathbf{D}_{ve}{}^{-1} R dX^1 , \qquad \bar{\mathbf{R}}^H = \int_0^L \mathbf{D}_{ve}{}^{-1}[\hat{\mathbf{S}}(\Delta\bar{\mathbf{w}}^h) - \bar{\mathbf{S}}^h] R dX^1 . \qquad (2.9.28c)$$

2.9.4. Iterative algorithm. Finite element matrices.

Dropping the factor of 2π, (2.9.24) and (2.9.27) can be assembled according to (2.9.17) to give the following systems of equations:

$$\sum_e \left\{ [(\delta \mathbf{w}^h)^T \; (\delta \mathbf{S}^h)^T] \left\{ \begin{bmatrix} \bar{\mathbf{K}}^{11} & \bar{\mathbf{K}}^{12} \\ \bar{\mathbf{K}}^{21} & \bar{\mathbf{K}}^{22} \end{bmatrix} \begin{bmatrix} \Delta \mathbf{w}^h \\ \Delta \mathbf{S}^h \end{bmatrix} + \begin{Bmatrix} \bar{\mathbf{R}}^C \\ \bar{\mathbf{R}}^H \end{Bmatrix} \right\} = \begin{Bmatrix} \mathbf{0} \\ \mathbf{0} \end{Bmatrix} \right\} . \tag{2.9.29}$$

Here, the matrix $\bar{\mathbf{K}}^{IJ}$ is the generalized element stiffness matrix. The component $\bar{\mathbf{K}}^{11}$ is commonly referred to as the geometric stiffness matrix which arises because of the geometric nonlinearity in finite deformation analyses. The vectors $\bar{\mathbf{R}}^C$ and $\bar{\mathbf{R}}^H$ are the residual (out-of-balance) load terms from the equilibrium and the constitutive relations, respectively.

The global coordinates, denoted as $\mathbf{u}^h$, are related to the local coordinates $\mathbf{w}^h$ by a coordinate transformation matrix $\mathbf{T}$

$$\mathbf{w}^h = \mathbf{T}\mathbf{u}^h \; . \tag{2.9.30}$$

Substitution of this into (2.9.29) gives

$$\sum_e \left\{ [(\delta \mathbf{u}^h)^T \; (\delta \mathbf{S}^h)^T] \left\{ \begin{bmatrix} \mathbf{T}^T \bar{\mathbf{K}}^{11} \mathbf{T} & \mathbf{T}^T \bar{\mathbf{K}}^{12} \\ \bar{\mathbf{K}}^{21} \mathbf{T} & \bar{\mathbf{K}}^{22} \end{bmatrix} \begin{bmatrix} \Delta \mathbf{u}^h \\ \Delta \mathbf{S}^h \end{bmatrix} + \begin{Bmatrix} \mathbf{T}^T \bar{\mathbf{R}}^C \\ \bar{\mathbf{R}}^H \end{Bmatrix} \right\} = \begin{Bmatrix} \mathbf{0} \\ \mathbf{0} \end{Bmatrix} \right\} . \tag{2.9.31}$$

The form (2.9.31) is not yet an optimal setup for computations. Compared to the form for a displacement type approach, this formulation has the additional stress variables, which results in a sparsely populated stiffness matrix. It is therefore desirable to eliminate these stress variables to reduce the computational effort. Noting that $\delta \mathbf{S}^h$ is discontinuous across the element boundaries, $H = 0$ in (2.9.4) is equivalent to $H_e = 0$. We can extract the incremental stress-displacement relation from (2.9.31) to give

$$\Delta \bar{\mathbf{S}}^h = -(\bar{\mathbf{K}}^{22})^{-1}\left[\bar{\mathbf{R}}^H + \bar{\mathbf{K}}^{21}\mathbf{T}\Delta\mathbf{u}^h\right] \tag{2.9.32}$$

Via this expression, it is now possible to write (2.9.31) entirely in terms of the unknowns $\Delta\mathbf{u}^h$ as

$$\bar{\mathbf{K}}\,\Delta\mathbf{u}^h = \bar{\mathbf{R}} \tag{2.9.33}$$

where the arbitrary variation $\delta\mathbf{u}^h$ is dropped from the above expression; and the stiffness matrix $\bar{\mathbf{K}}$ and the out-of-balance load $\bar{\mathbf{R}}$ are:

$$\bar{\mathbf{K}} = \sum_e \mathbf{T}^T\left[\bar{\mathbf{K}}^{11} - \bar{\mathbf{K}}^{12}(\bar{\mathbf{K}}^{22})^{-1}\bar{\mathbf{K}}^{21}\right]\mathbf{T} \tag{2.9.34a}$$

$$\bar{\mathbf{R}} = \sum_e \mathbf{T}^T\left[\bar{\mathbf{R}}^G - \bar{\mathbf{K}}^{12}(\bar{\mathbf{K}}^{22})^{-1}\bar{\mathbf{R}}^H\right] \tag{2.9.34b}$$

Computationally, it is convenient to enforce the condition $\bar{\mathbf{R}}^H = \mathbf{0}$ in (2.9.32) and (2.9.34b) so that the stresses at the element level may be evaluated directly. Based on (2.9.28), the stresses for the "linear", the Mooney-Rivlin and the viscoelastic materials are

Linear material
$$\bar{\mathbf{S}}^h = \mathbf{D}\int_0^L \mathbf{E}(\bar{\mathbf{w}}^h)R\,dX^1 \Big/ \int_0^L R\,dX^1\,, \tag{2.9.35a}$$

Mooney–Rivlin material
$$\bar{\mathbf{S}}^h = \left[\int_0^L \mathbf{D}^{-1}(\bar{\mathbf{w}}^h)R\,dX^1\right]^{-1}\int_0^L \mathbf{D}^{-1}(\bar{\mathbf{w}}^h)\hat{\mathbf{S}}(\bar{\mathbf{w}}^h)R\,dX^1 \tag{2.9.35b}$$

Viscoelastic material
$$\bar{\mathbf{S}}^h = \int_0^L \hat{\mathbf{S}}(\bar{\mathbf{w}}^h)R\,dX^1 \Big/ \int_0^L R\,dX^1\,. \tag{2.9.35c}$$

Equations (2.9.33), (2.9.34), and (2.9.35) constitute the set of linearized algebraic equations required to construct a Newton-Raphson type iterative algorithm, which is summarized in Box 2.9.2.

Box 2.9.2. Iterative algorithm for axisymmetric shell

For each time step t_n

- evaluate the strains $\mathbf{E}_n$ and stresses $\mathbf{S}_n$
- form out-of-balance load vector $\mathbf{R}_n$
- advance to next time step if $\| \mathbf{R}_n \| \leq tol$, otherwise
- form the tangent stiffness matrix $\mathbf{K}_n$
- solve $\mathbf{K}_n \Delta\mathbf{u}_n = \mathbf{R}_n$ for $\Delta\mathbf{u}_n$
- increment $\mathbf{u}_n$ by $\mathbf{u}_n + \Delta\mathbf{u}_n$

2.10. Further discussions on element loading.

2.10.1. Extension to the follower load.

The loading $\mathbf{P}$ included in the weak form of the equilibrium equations (2.9.3) is assumed to remain constant throughout the deformation history. In this section, we shall extend this to the case in which the orientation of the loading follows the deformation of the shell. Attention will be focused on the case of a uniformly distributed load, with an invariant load magnitude p. One example of this type of follower load is the internal pressure acting on the shell. In that case, the pressure always acts perpendicular to the deformed reference surface of the shell.

The follower load is denoted here as $\mathbf{t}$. We designate the vector $\mathbf{m}$ as the normal to the deformed reference surface $\Phi_0(X^1)$ of the shell. Thus

$$\mathbf{t} = p\,\mathbf{m} \tag{2.10.1}$$

The contribution of $\mathbf{t}$ to the weak form of the equilibrium equation in (2.9.3) can be formulated as follows

$$G_e^{follow} = \int_a \delta\mathbf{w}\cdot\mathbf{t}\,da = p\int_a \delta\mathbf{w}\cdot\mathbf{m}\,da \tag{2.10.2}$$

where $\delta\mathbf{w}$ is the admissible displacement variations introduced in Section 2.9, and da is the deformed surface area element. Let the vector $\mathbf{M}$ denote the normal to the reference surface in the undeformed configuration. With respect to the base vectors $\mathbf{G}_I$, $\mathbf{M}$ has coordinates $[0, 1, 0]^T$. We also denote the undeformed surface area element by dA. Then we can write

$$\mathbf{n}da = (J\mathbf{F}^{-T})|_{X^2=0}\mathbf{M}dA \tag{2.10.3}$$

where the quantities J and $\mathbf{F}^{-T}$ are those defined in (2.3.5) and (2.3.9). It follows that

$$G_e^{follow} = p\int_A \delta\mathbf{w}\cdot(J\mathbf{F}^{-T})|_{X^2=0}\mathbf{M}\,dA = 2\pi p\int_0^L \delta\mathbf{w}\cdot\mathbf{b}\,RdX^1 \tag{2.10.4}$$

where $dA = 2\pi RdX^1$, and $\mathbf{b} \equiv \frac{\tau}{R}[w'\ 1+u'\ 0]^T$.

Following the linearization procedure outlined in the previous section, the linearized form of (2.10.4) is

$$L[G_e^{follow}]_{(\mathbf{w},\mathbf{S})} = 2\pi p\int_0^L \delta\mathbf{w}\cdot\left[\bar{\mathbf{b}} + \bar{\mathbf{L}}\Delta\mathbf{W}\right] RdX^1 \tag{2.10.5}$$

Here $\Delta\mathbf{W} = [\Delta\mathbf{w}\ \Delta\mathbf{w}']^T$, and

$$\bar{\mathbf{L}} \equiv \frac{1}{R}\begin{bmatrix} -\sin\alpha\bar{w}' & -\cos\alpha\bar{w}' & 0 & 0 & -\bar{\tau} & 0 \\ \sin\alpha(1+\bar{u}') & \cos\alpha(1+\bar{u}') & 0 & \bar{\tau} & 0 & 0 \\ 0 & 0 & 0 & 0 & 0 & 0 \end{bmatrix}$$

The discretized form of (2.10.5), employing the shape functions (2.9.23), takes the following form

$$L[G_e^{follow}]_{(\mathbf{w},\mathbf{S})} = 2\pi\sum_{I=1}^{2}(\delta\mathbf{w}_I)^T\left[\bar{\mathbf{P}}_I^{follow} - \sum_{J=1}^{2}\bar{\mathbf{K}}_{IJ}^{follow}\right]\Delta\mathbf{w}_J \tag{2.10.6}$$

In the above expression, the first term $\mathbf{P}^{follow}$ is the load vector here to replace the vector $\mathbf{P}$ in (2.9.3c) for the "non-follower load" case, where

$$\bar{\mathbf{P}}_I^{follow} \equiv \int_0^L p h_I \bar{\mathbf{b}}\, R dX^1 \tag{2.10.7a}$$

The second term $\bar{\mathbf{K}}^{follow}$ is the "load stiffness" matrix arise due to the deformation dependence of the follower load. In terms of the matrix **B** introduced in (2.9.23),

$$\bar{\mathbf{K}}_{IJ}^{follow} \equiv \int_0^L p h_I \bar{\mathbf{L}}\bar{\mathbf{B}}_J\, R dX^1 \tag{2.10.7b}$$

$$= \int_0^L p h_I \begin{bmatrix} \sin\alpha\bar{w}' h_J & \cos\alpha\bar{w}' h_J + \bar{r} h'_J & 0 \\ -\sin\alpha(1+\bar{u}') h_J - \bar{r} h'_J & -\cos\alpha(1+u') h_J & 0 \\ 0 & 0 & 0 \end{bmatrix} R dX^1$$

The "load stiffness" matrix $\bar{\mathbf{K}}_{IJ}$ must be incorporated into (2.9.33) to assure solution convergence when follower load is acting. Note that this "load stiffness" matrix is not symmetric in general. However, in the case of conservative loading, the load stiffness matrix is nonsymmetric only at the element level, and the *global* load stiffness matrix is ***always*** symmetric (see Hibbitt [1979], and Schweizerhof and Ramm [1984]).

2.10.2. Discretization of the loading term.

It was pointed out by Halleux [1980] that the ***consistent*** discretization of the loading term does not necessarily produce the best results in the axisymmetric case. A simple test problem to show this involves the pressurization of a spherical shell. For this case, the spherical shape is preserved, and the deformation only involves the change in the radius of the sphere.

For simplicity, we consider only the loading that does not follow the deformation. The conclusion of this equally applies to the case of the follower load. Consider the situation $p_1=0, p_2=p$ in (2.9.3), such that the contribution of the loading to the weak form is

$$G_e^{load} = 2\pi \int_0^L \delta \mathbf{w} \cdot \begin{Bmatrix} 0 \\ p \\ 0 \end{Bmatrix} R dX^1 = 2\pi \int_0^L pw \; R dX^1 \; . \tag{2.10.8}$$

We shall focus our attention on the 2-node elements, and employ the shape function h_I such that

$$w = \sum_{I=1}^{2} h_I w_I \; . \tag{2.10.9}$$

Substitution of (2.10.9) into (2.10.8) gives

$$G_e^{load} = 2\pi \int_0^L p \sum_{I=1}^{2} h_I w_I \; R dX^1 = 2\pi \sum_{I=1}^{2} p^I w_I \tag{2.10.10}$$

where p^I are the discretized nodal load values. These values p^I are dependent on the choice of the shape function h_I, and the numerical method used in evaluating the integral in (2.10.10). Of course, the quality of the analysis results varies for different choices of p^I. We shall investigate several different possibilities next.

The nodal loads p^I can be parametrized in terms of the coefficient α as follows

$$p^1 = \frac{pL}{2}\left[\alpha r_1 + (1-\alpha) r_2\right], \tag{2.10.11a}$$

$$p^2 = \frac{pL}{2}\left[(1-\alpha) r_1 + \alpha r_2\right]. \tag{2.10.11b}$$

where r_1 and r_2 are the radii at the two nodes. The parameter α takes on a value in the range [0,1]. For example, $\alpha = 2/3$ corresponds to the choice of linear shape (consistent) functions h_I with exact integration in (2.10.10). For the same shape functions, $\alpha = 1/2$ corresponds to one point integration, and $\alpha = 2/3$ is obtained when nodal quadrature is used. Finally, $\alpha = 3/4$ can be derived from exactly integrating (2.10.10) using the shape functions $h_1 = 1$ over [0,L/2], $h_2 = 1$ over [L/2,L] and $h_I = 0$ otherwise. This last example will be

referred to as the case of "lumped load".

The choice of the value α is evaluated via a test problem involving the pressurization of a sphere. We employ four finite element meshes with 5, 10, 20 and 40 shell elements respectively to model the symmetric half of the sphere. The shell elements are subjected to uniformly distributed loading, discretized by the four different choices mentioned above, namely $\alpha = 1,\ 1/2,\ 2/3$ and $3/4$. The results, quantified in terms of the normalized equatorial and the polar displacements u_e and u_p respectively, are tabulated in Table 2.10.1. These results show that the "lumped load" case (a=3/4) performs excellently in providing the most exact answers, and mostly importantly, in predicting a spherical deformed configuration even by the crude mesh with 5 elements. This result is consistent with the finding of Halleux [1980]. The consistent discretization (a=2/3) gives good results, but the deformation is not spherical except for the refined mesh. The other two lumping parameters (a = 1/2, 1) give poor results.

2.11. Numerical examples.

We present here some numerical examples to demonstrate the capabilities of the shell/membrane formulation developed above. The algorithm is implemented in a general purpose finite element program FEAP (see Zienkiewicz [1977], Chapter 24).

The first example illustrates the behavior of the shell undergoing large displacements. For this problem, we also examine the sensitivity of the post-buckling responses to changes in loading and boundary conditions. The next two examples compare the membrane responses to large stretching with known

† u_e = computed equatorial displacement / exact , u_p = computed polar displacement / exact .

‡ see Equation (2.10.11).

Table 2.10.1. Study of load discretization parameter α in (2.10.11).

Pressurization of a Spherical Shell †				
Number of shell elements	nodal quadrature $a^{\ddagger} = 1$	mid-point $a = 1/2$	consistent load $a = 2/3$	lumped load $a = 3/4$
5	$u_e = 1.003$ $u_p = 0.277$	$u_e = 0.973$ $u_p = 1.699$	$u_e = 0.983$ $u_p = 1.225$	$u_e = 0.988$ $u_p = 0.988$
10	$u_e = 1.003$ $u_p = 0.900$	$u_e = 0.991$ $u_p = 1.198$	$u_e = 0.995$ $u_p = 1.064$	$u_e = 0.997$ $u_p = 0.997$
20	$u_e = 1.001$ $u_p = 0.958$	$u_e = 0.998$ $u_p = 1.052$	$u_e = 0.999$ $u_p = 1.016$	$u_e = 0.999$ $u_p = 0.999$
40	$u_e = 1.000$ $u_p = 0.988$	$u_e = 0.999$ $u_p = 1.013$	$u_e = 1.000$ $u_p = 1.000$	$u_e = 1.000$ $u_p = 1.000$

solutions. Both of these examples utilize the follower load (Section 2.10) to simulate the pressure acting on the membrane. The last example demonstrates the viscoelastic behavior of the shell to creep, relaxation and cyclic loading.

The analyses of the post-buckling response proposed above require special handling. Conventional methods that rely on force control algorithms cannot trace the portions of the load-displacement curve having negative slopes. Here,

we employ the displacement control method (details discussed in Riks [1972] and Wempner [1972] for example), adapted to the analysis program FEAP by Karl Schweizerhof.

The Newton-Raphson iteration scheme as outlined in Box 2.9.2 is employed to solve for the solution of the nonlinear equations. This solution method results in a quadratic rate of convergence, based on the Euclidean norm of the out-of-balance load.

Example 2.11.1. Spherical cap under center and ring loads.

The analytical solution based on Reissner [1950b] is provided in Mescall [1965] for the case of a concentrated load applied at the apex of a spherical cap. Our simulations employ the geometric parameters given in Zienkiewicz [1977]. Assuming the material as being elastic, the following parameters are used (see expression (2.8.4) and Fig. 2.4):

E =	10×10^6 *lb/in*^{2}
ν =	0.3
a =	4.758 *in*
h =	0.01576 *in*
ξ =	10.9035 °

The geometric parameter λ^2, defined by Mescall as $\lambda^2 = [12(1-\nu^2)]^{1/2}(\sin\xi)^2 a/h$, is approximately 36 for this case.

We first present the responses of a spherical cap subjected to ring loads of radii $r = 0, 0.225$, and 0.375 *in*. For each case we employ two finite element meshes comprising 12 and 24 shell elements, respectively. The loading is displacement-driven, with the apex displacement advances at 0.01 *in*. per load step. The resulting load-displacement curve shown in Fig. 2.5, compares well with those of Mescall and Zienkiewicz. In Fig. 2.6, the predicted deformed shapes in apex displacement increments of 0.02 *in*. are also illustrated.

The behavior of the shell is quite different if the boundary condition is changed. When the rim of the spherical cap is free to rotate, a concentrated center load causes the shell to "snap-through", as shown in the load-displacement curves (Fig. 2.7) and the corresponding deformed shapes (Fig. 2.8). If the horizontal restraint is also removed, the analysis yields a critical load of 16.8 *lb.* for snap-through instability to occur, in agreement with the prediction of Mescall.

Example 2.11.2. Inflation of a spherical shell.

From equilibrium, the internal pressure p is related to the isotropic tension N as

$$p = \frac{2N}{\lambda^2 R} \tag{2.11.1}$$

where R is the undeformed radius of the sphere, and λ is the isotropic stretch. For the Mooney-Rivlin material in (2.8.11),

$$p = \frac{4h}{\lambda R}\left(1-\frac{1}{\lambda^6}\right)(A_1 + A_2\lambda^2) \tag{2.11.2}$$

where h is the thickness of the membrane. Similarly, we otain for the "linear" material in (2.8.5)

$$p = \frac{2Eh}{(1-\nu)R}\left[\frac{1-\lambda}{\lambda^2}\right]. \tag{2.11.3}$$

We simulate the Mooney-Rivlin case using the following parameters:

$A_1 = 10$
$A_2 = 0,\ 0.1$ and 0.5
R = 1000
h = 1

For the "linear" material case, we use $E = 60$. This value is obtained by comparing the linearized forms of (2.8.5) and (2.8.11) for $\nu = 0.5$, which gives the

following relation between the parameter A_1, A_2 and E

$$E = 6(A_1 + A_2) . \tag{2.11.4}$$

A finite element mesh comprising 10 membrane elements models the symmetric half of the sphere. A uniform follower load is applied over all the elements to simulate the internal pressure.

The results of the simulations, as shown in Fig. 2.9, demonstrate that the ratio A_2/A_1 affect the pressure-stretch relation significantly. For $A_2/A_1 = 0.5$, the pressure increases monotonically with the stretch. On the other hand, for $A_2/A_1 = 0$ and 0.1, the pressure reaches a peak and decreases with increased stretching. For $A_2/A_1 = 0.1$, this pressure decrease is again followed by an increase at higher stretch. The response of the "linear" case is similar in form to the case $A_2/A_1 = 0$; although the pressure of the former is three to four times that of the latter.

In all of the simulations, the pressure-stretch graphs are traced to be within 0.3% error. Because only the radius of the sphere is changed from pressurization, the Newton-Raphson method converges to the solution in one iteration.

Example 2.11.3. Inflation of a circular plane sheet.

The analytic solution for this problem is given in Green and Adkins [1960], and numerical simulations have also been performed by various workers (Oden [1972] and Argyris [1969]).

A circular plane sheet of radius R and thickness h is modeled with two finite element meshes comprising 10 and 30 elements, respectively. The region near the fixed outer rim, over which significant straining is anticipated, is represented by a finer meshing for the 30-element model. We assume the material to be the Mooney-Rivlin material in (2.8.11), and employ the following

geometric and material data for the simulation:

$$\begin{aligned} A_1 &= 9.5\ kp/cm^2 \\ A_2 &= 1.75\ kp/cm^2 \\ h &= 0.02cm. \\ R &= 5.08cm. \end{aligned}$$

The predicted pressure versus center vertical displacement curve, shown in Fig. 2.10, agrees well with the results of Argyris [1969]. Despite the difference in mesh refinement, the predictions by the two models here are almost identical. The deformed shapes for several load levels, as shown superimposed in Fig. 2.11, indicate that the two models predict the same extent of deformation at the nodes. As expected, the more refined model provides smoother contours of the deformed configurations.

We also consider the cases with $A_2/A_1 = 0.1$ and 0 using the 30-element model. The results are in accordance with the finding of Green and Adkin [1960], that the response is very sensitive to the material constants A_2. This is illustrated by the drastic differences in the strain distributions between the two cases, as shown in Figs. 2.12. The deformed shapes for these cases are also shown in Fig. 2.13.

Example 2.11.4. Viscoelastic responses of the shell.

We demonstrate here the creep, relaxation and cyclic responses of the viscoelastic shell. For illustration purposes, we again consider the inflation of a spherical shell, which results in isotropic stress σ and strain ε states.

When a constant stress σ is suddenly applied at time $t = 0$, the strain history $\varepsilon(t)$ is:

$$\varepsilon(t) = \sigma\left[\left(\frac{1}{E_a} - \frac{1}{E_l}\right)e^{-\frac{E_l}{E_a}\beta t} + \frac{1}{E_l}\right] \tag{2.11.5}$$

where β is a material time constant, and E_s and E_l are the instantaneous (short term) and the asymptotic (long term) moduli. The creep function $C(t)$ is defined by $C(t) \equiv \frac{\varepsilon(t)}{\sigma}$, and the creep time constant $\tau_{creep} \equiv \frac{E_s}{E_l \beta}$. Interchanging the roles of σ and ε, when a constant strain ε is suddenly applied at time $t = 0$, the stress history $\sigma(t)$ is:

$$\sigma(t) = [E_l + (E_s - E_l)e^{-\beta t}]\varepsilon \ . \tag{2.11.6}$$

The relaxation function $E(t)$ is defined by $E(t) \equiv \frac{\sigma(t)}{\varepsilon}$, and the relaxation time constant $\tau_{relaxation} \equiv \frac{1}{\beta}$. Equations (2.11.5) and (2.11.6) are illustrated in Figs. 2.14 and 2.15 for $E_s / E_l = 5$ and 10. As shown in these figures, the results from simulations based on equation (2.9.14) are in good agreement with these analytical results.

When this viscoelastic shell is subjected to a sinusoidal strain input $\varepsilon(t) = \varepsilon_0 \sin\omega t$, the stress history $\sigma(t)$ is:

$$\sigma(t) = \varepsilon_0 \left\{ \left[\frac{E_l + \frac{\omega^2}{\beta^2} E_s}{1 + \frac{\omega^2}{\beta^2}} \right] \sin\omega t + \left[\frac{E_s - E_l}{1 + \frac{\omega^2}{\beta^2}} \right] \frac{\omega}{\beta} \cos\omega t \right\} . \tag{2.11.7}$$

As shown in Fig. 2.16, our simulation result closely approximates (2.11.7).

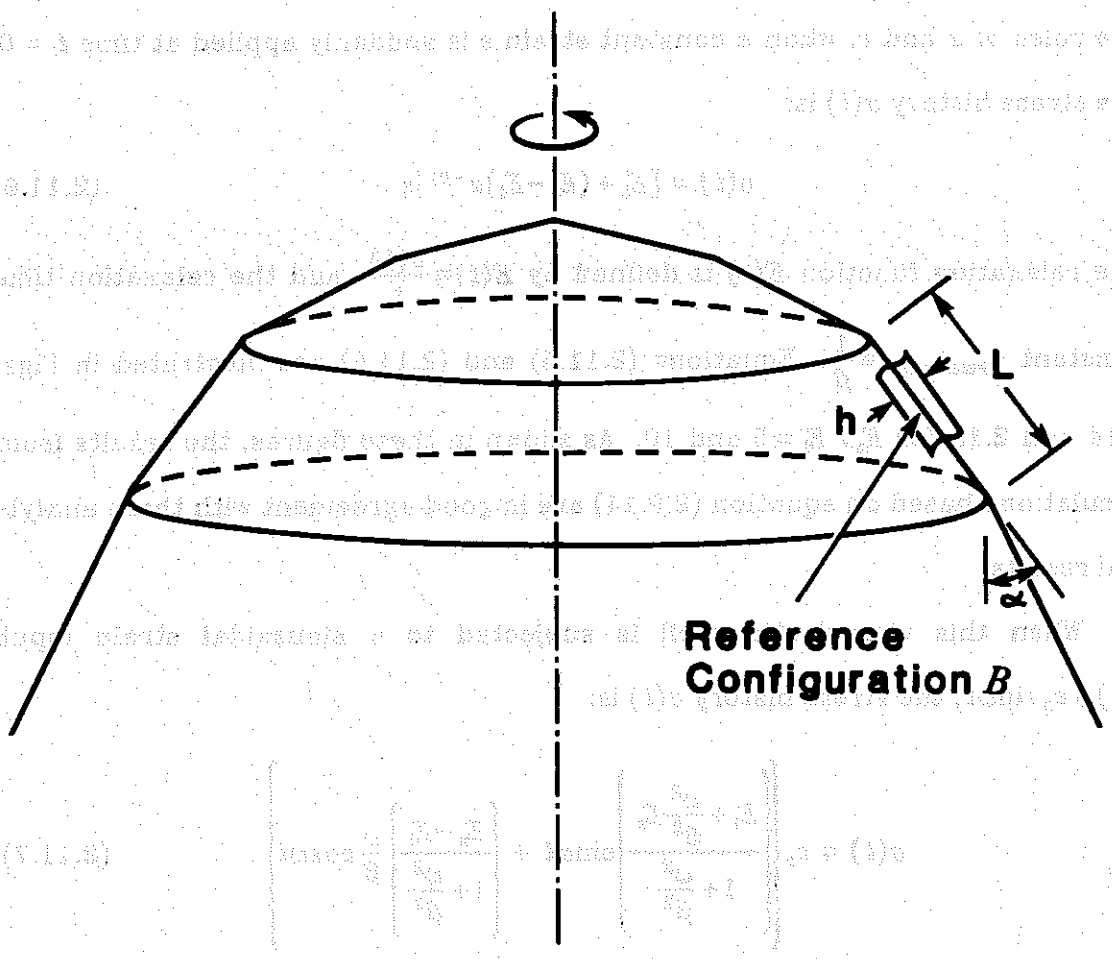

Fig. 2.1. The reference configuration for an axisymmetric shell-like body.

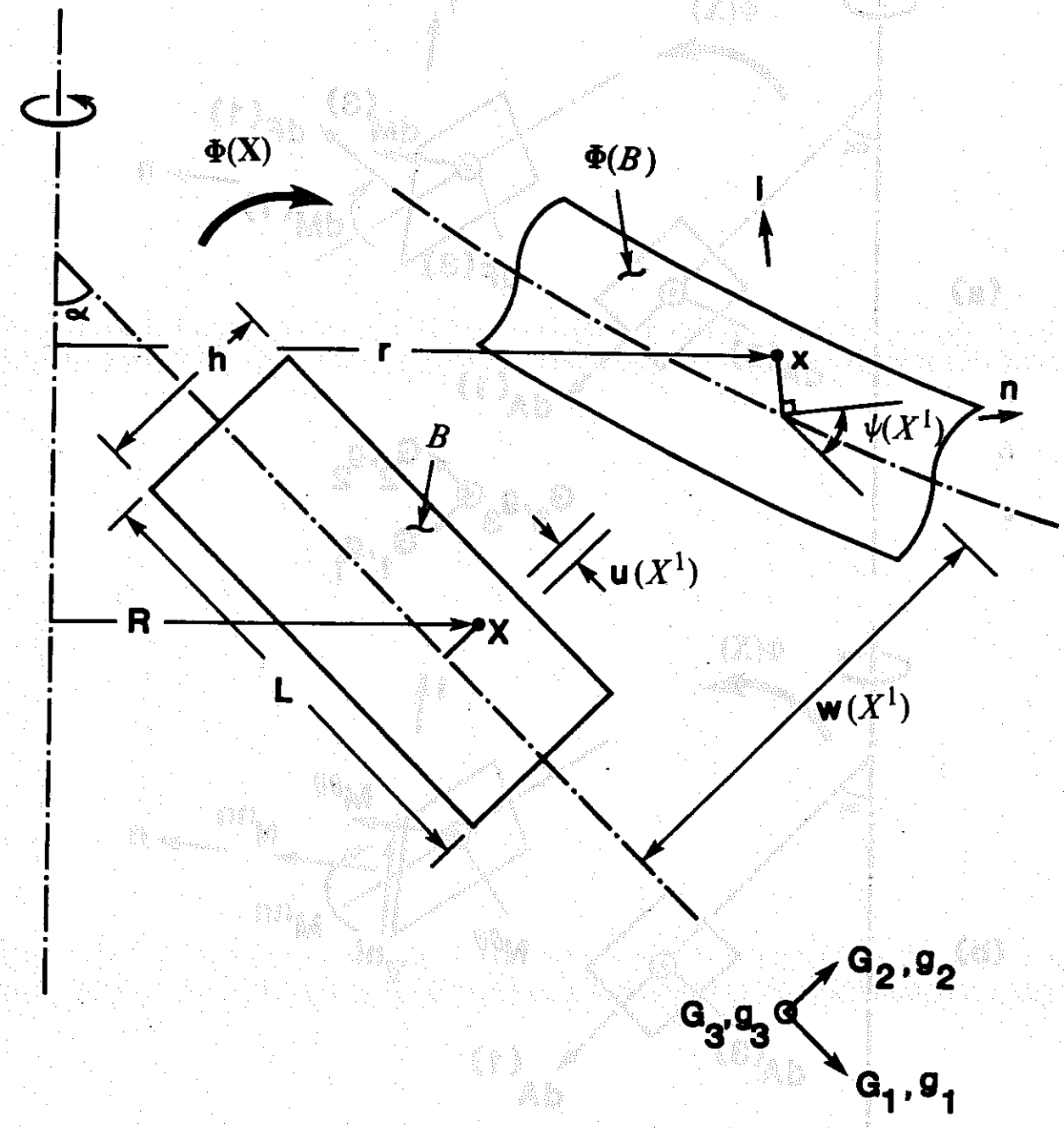

Fig. 2.2. Kinematics of an axisymmetric shell on the meridian plane.

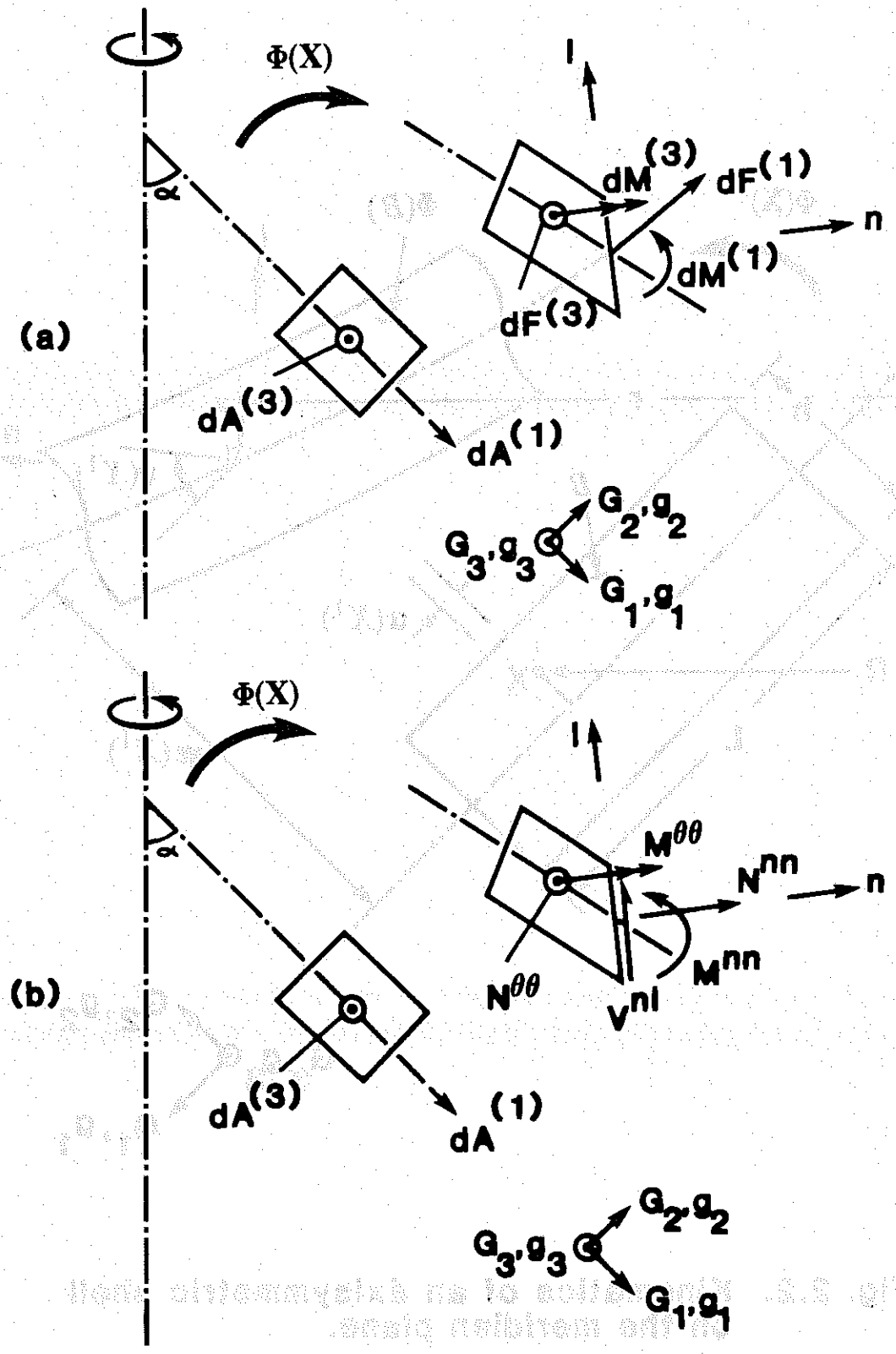

Fig. 2.3. (a) Forces and moments (b) stress resultants acting on a volume of a shell.

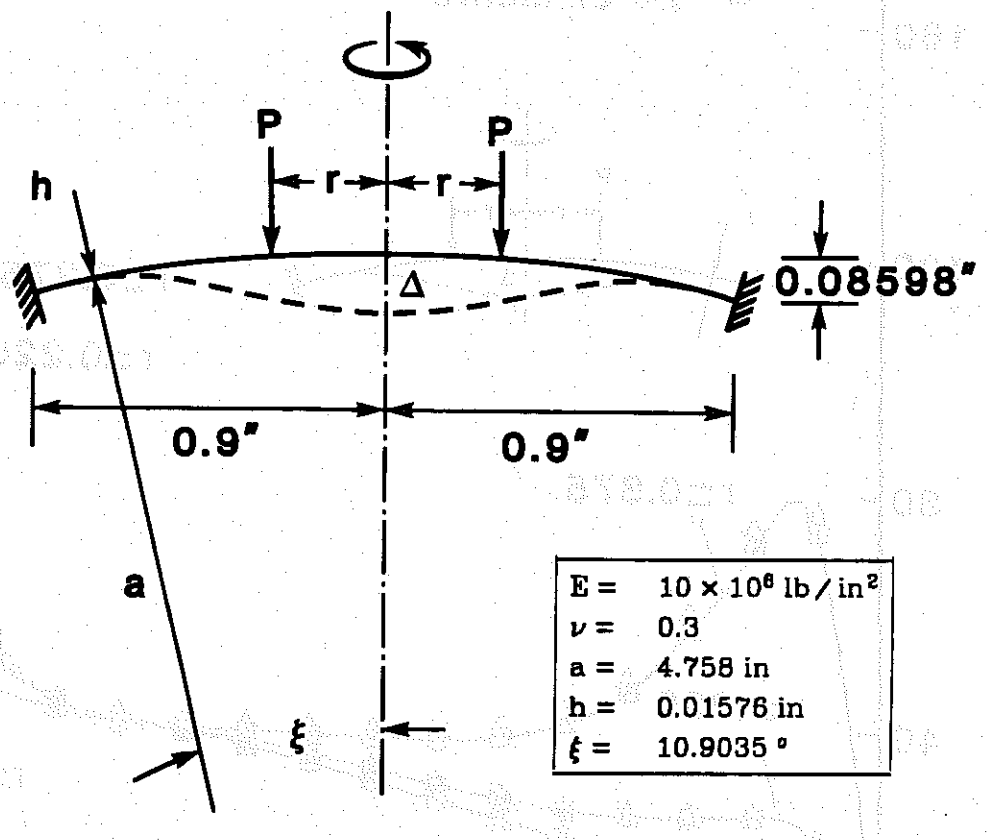

Fig. 2.4. Spherical cap under ring loads. Geometry and data.

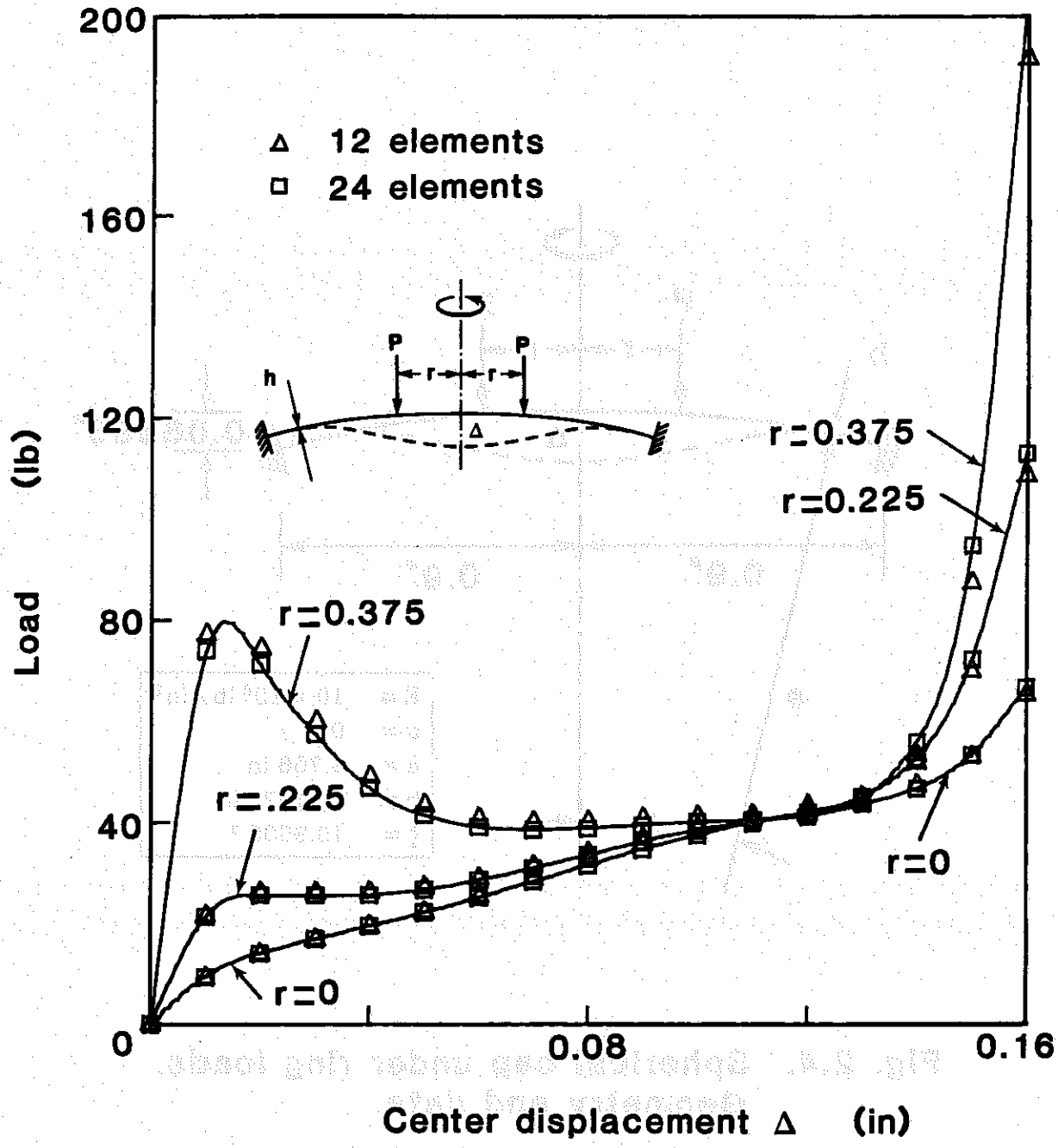

Fig. 2.5. Spherical cap under ring loads.
Force-displacement curve.

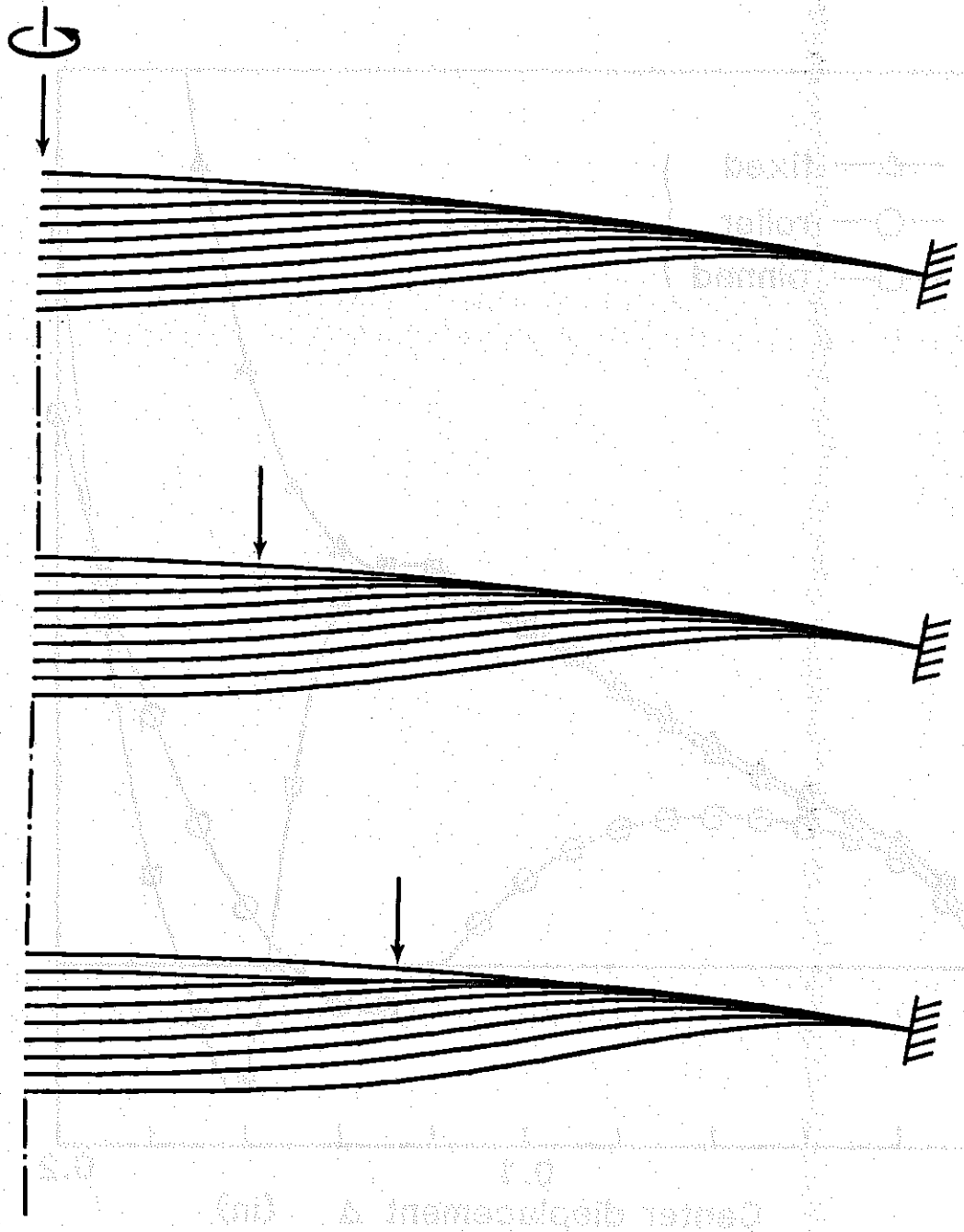

Fig. 2.6. Spherical cap under ring loads. Deformed shapes.

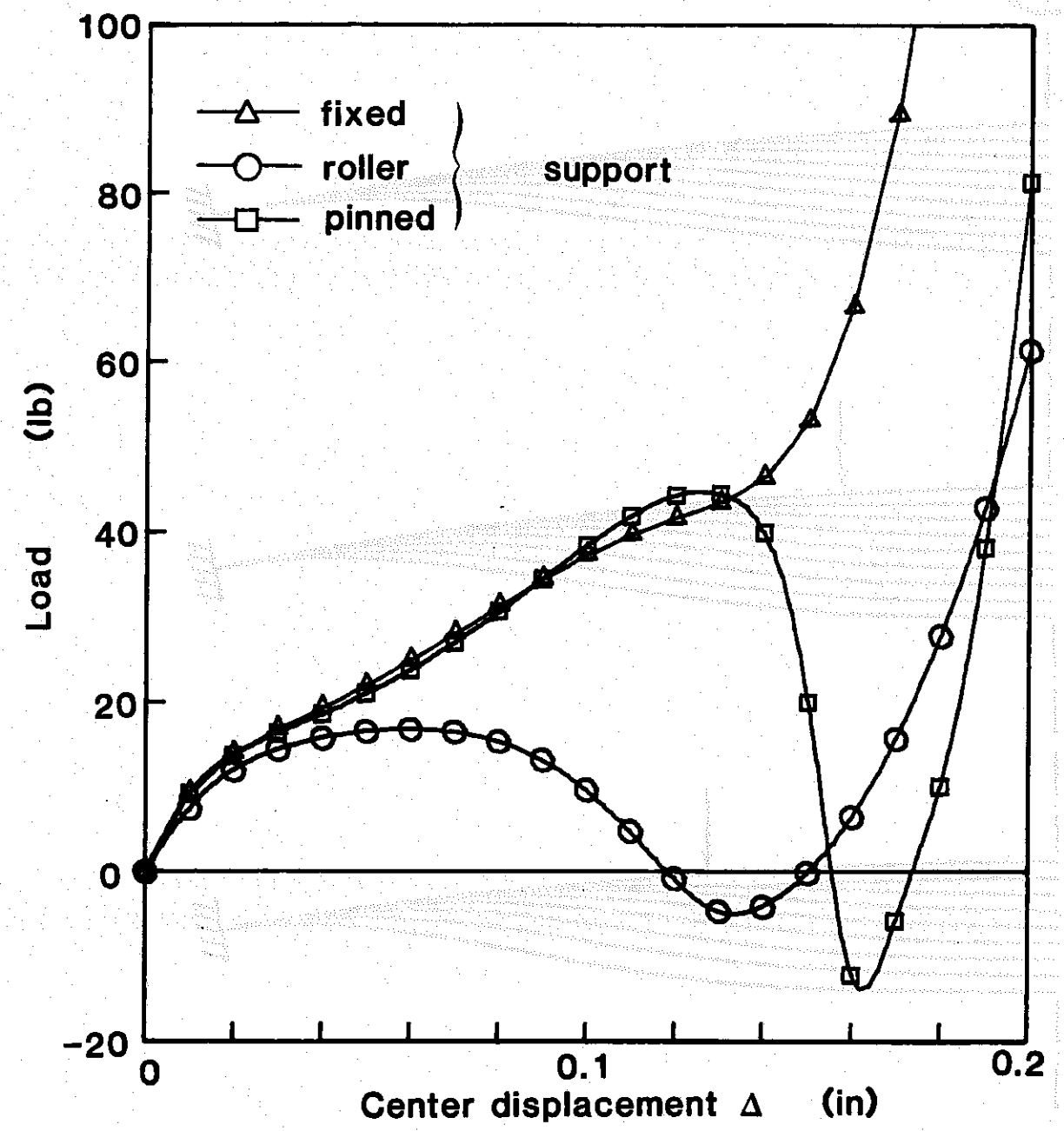

Fig. 2.7. Spherical cap under center load. Force-displacement curve.

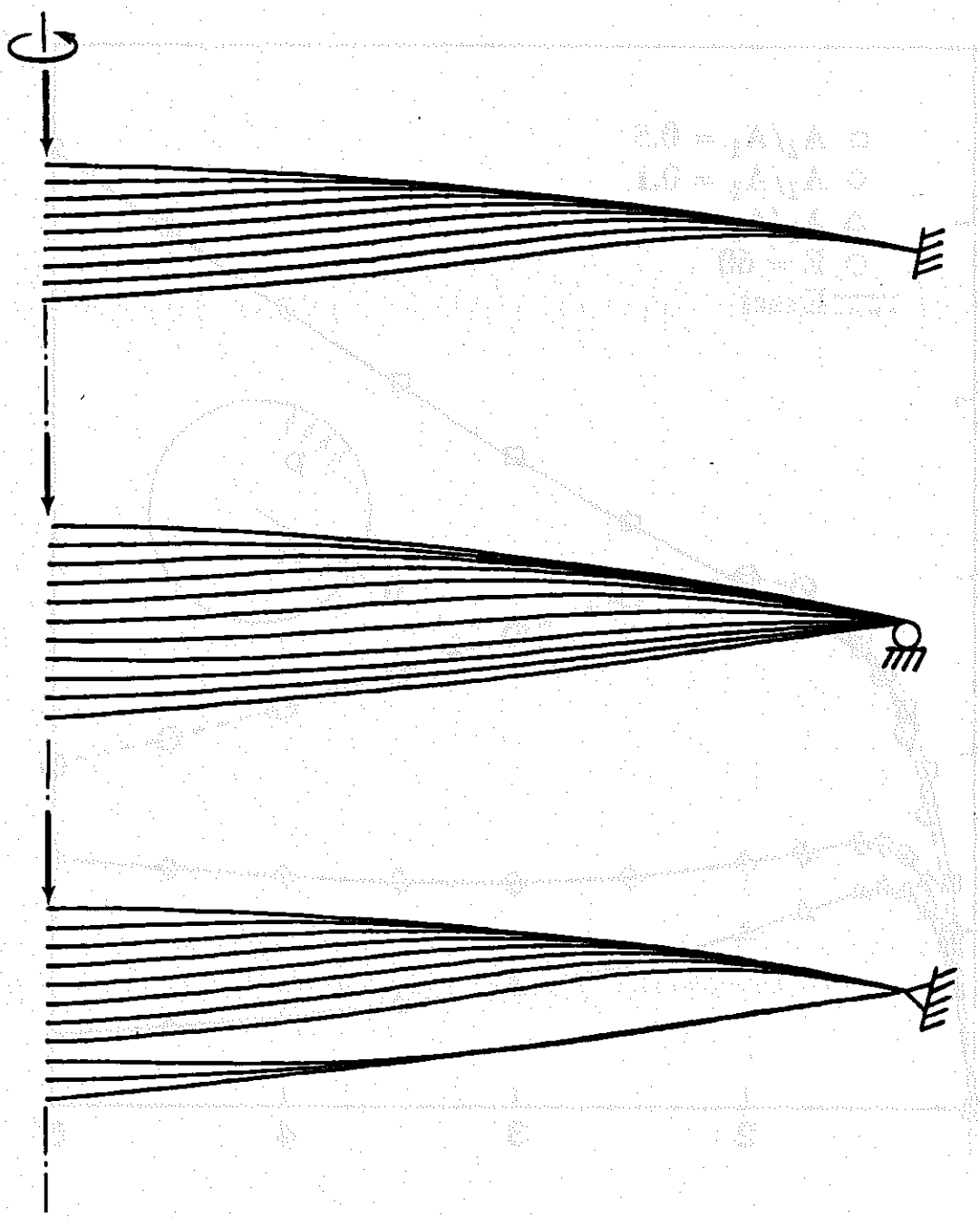

Fig. 2.8. Spherical cap under center load. Deformed shapes.

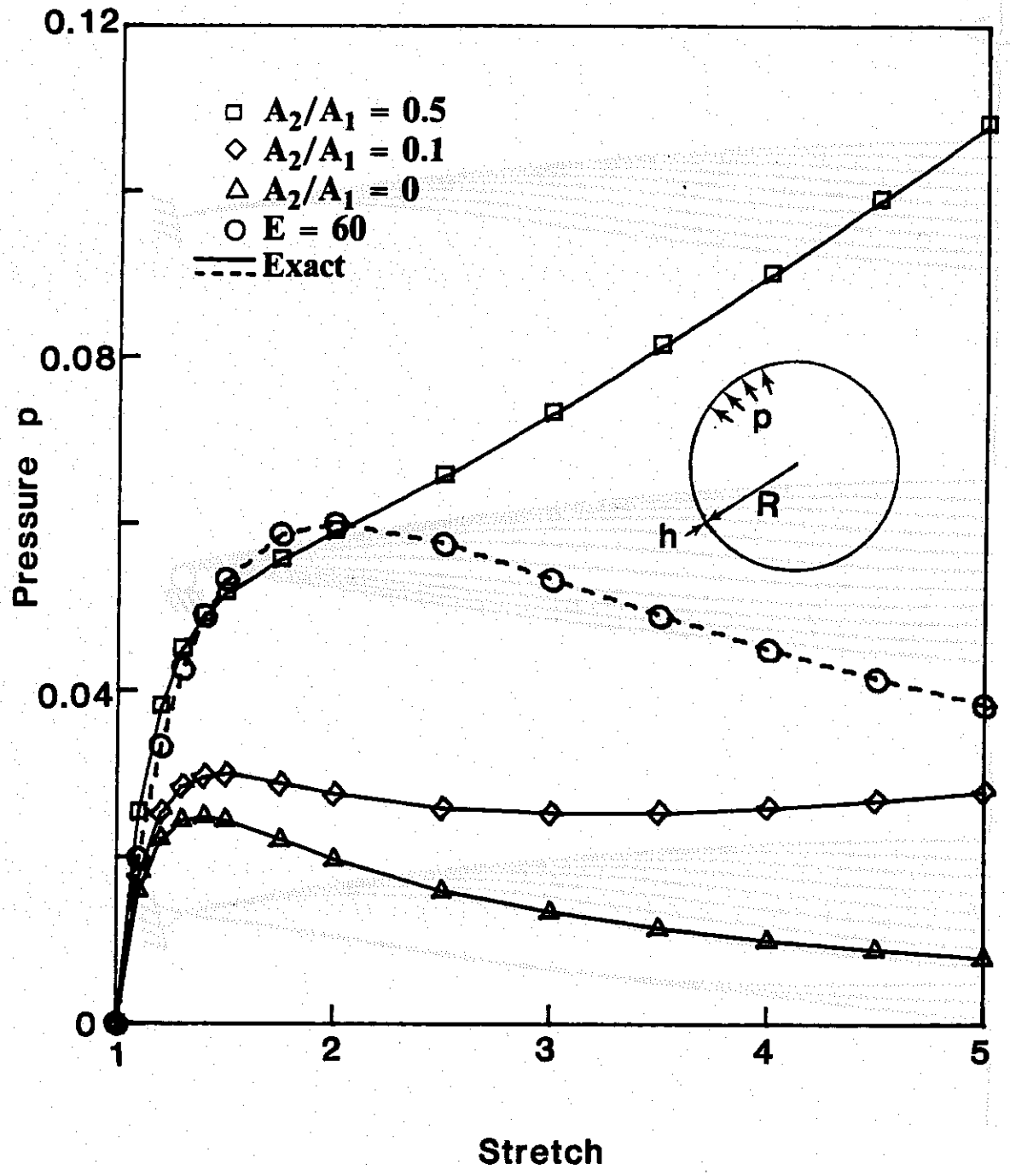

Fig. 2.9. Inflation of a spherical shell. Pressure–displacement curve.

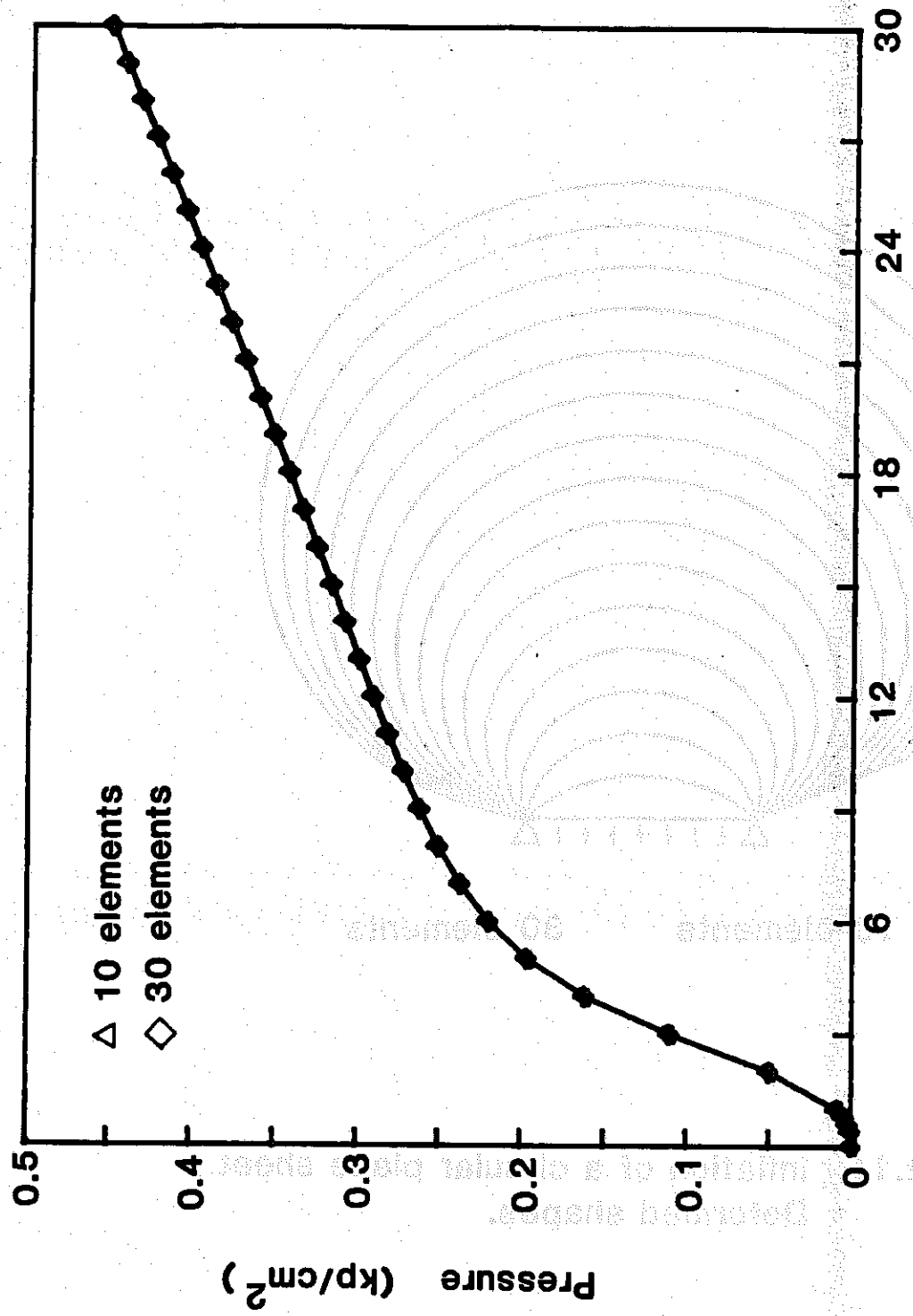

Fig. 2.10. Inflation of a circular plane sheet. Pressure–displacement curve.

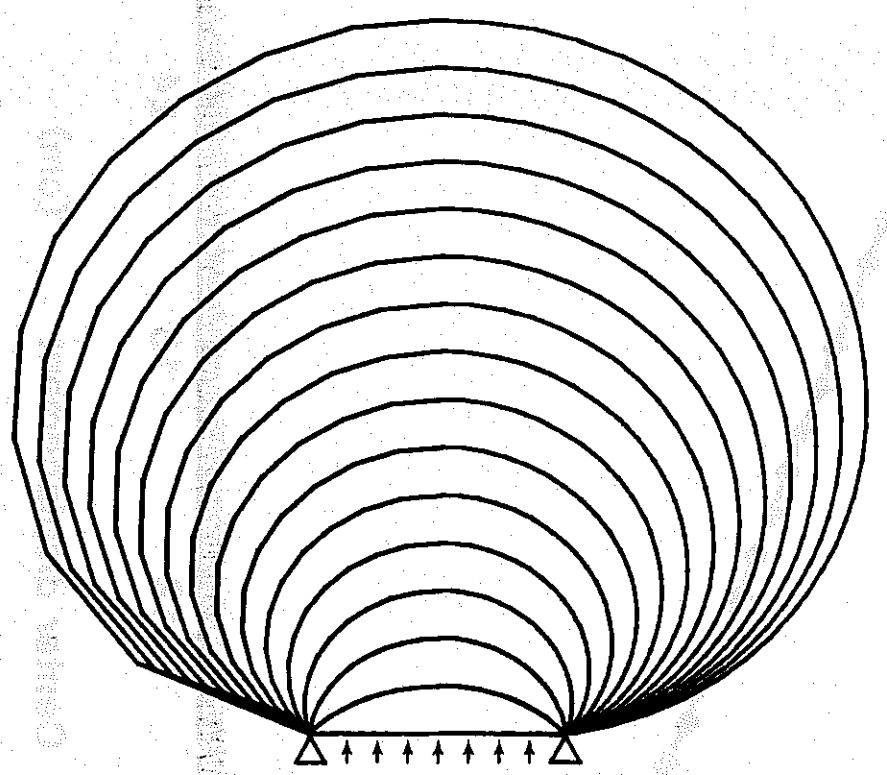

10 elements 30 elements

Fig. 2.11. Inflation of a circular plane sheet. Deformed shapes.

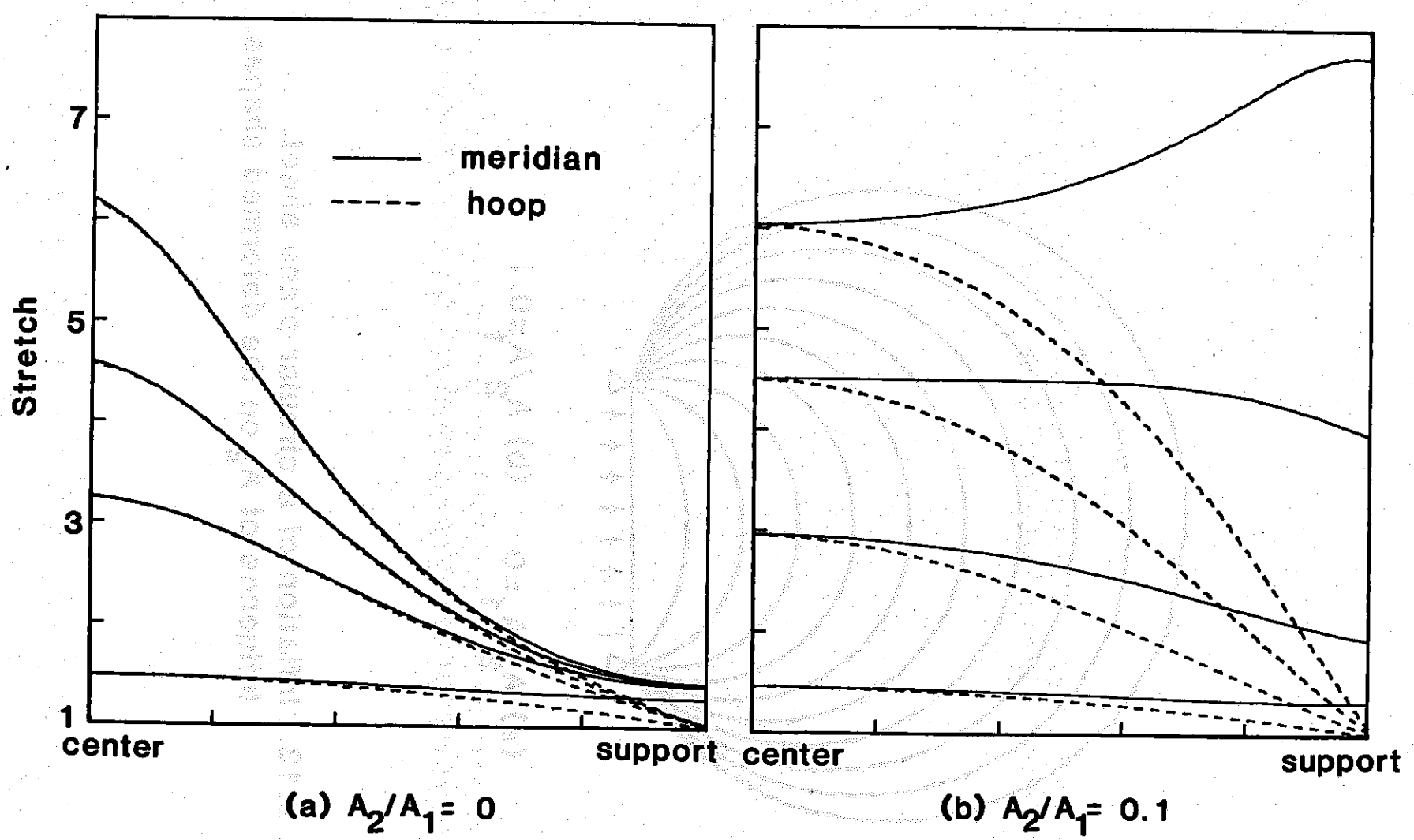

Fig. 2.12. Inflation of a circular plane sheet. Profiles of stretch.

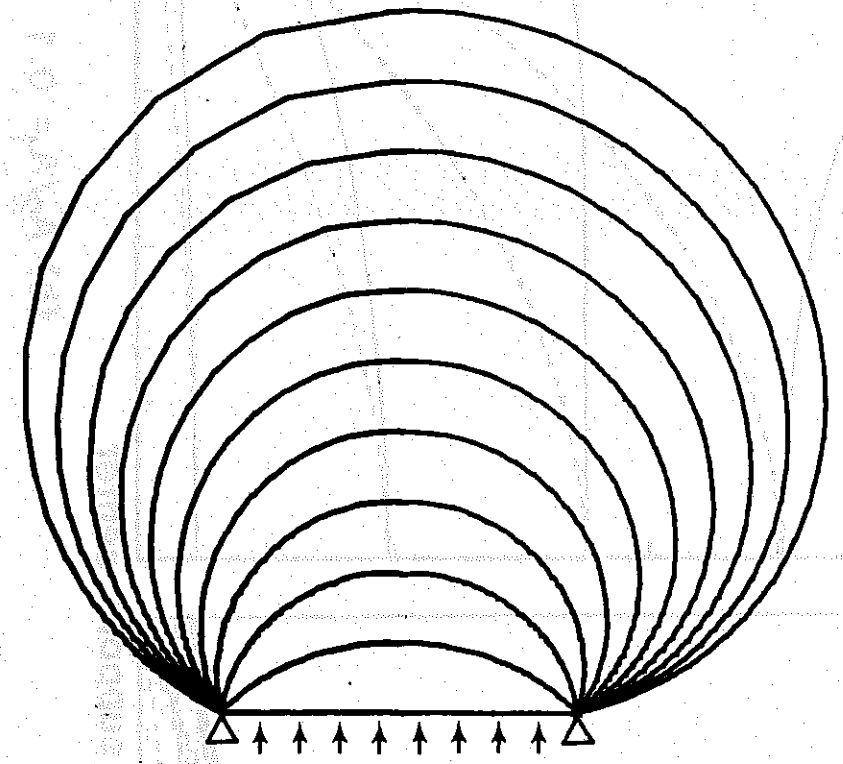

(a) $A_2/A_1=0$ (b) $A_2/A_1=0.1$

Fig. 2.13. Inflation of a circular plane sheet. Influence of A_2 on the deformed shapes.

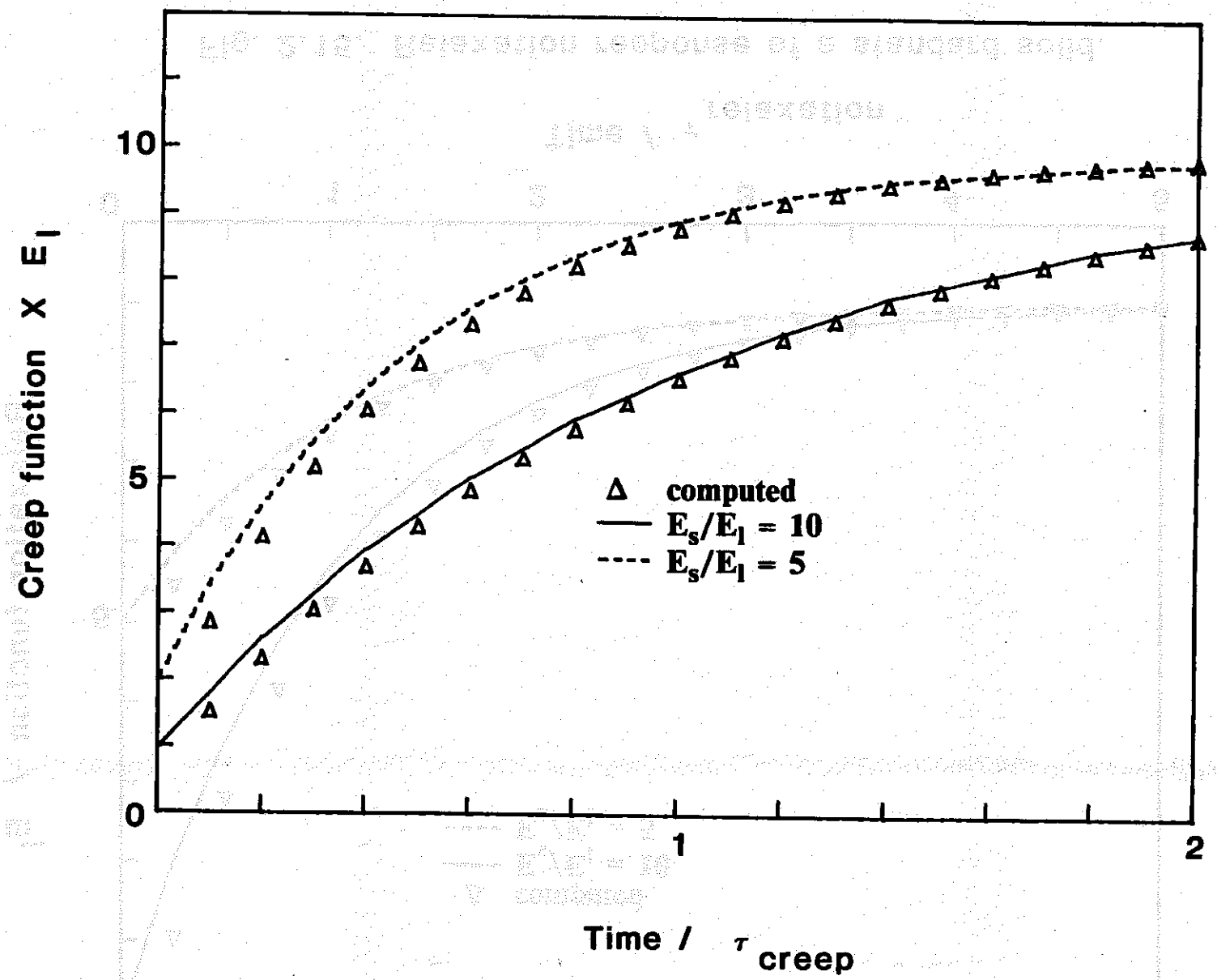

Fig. 2.14. Creep response of a standard solid.

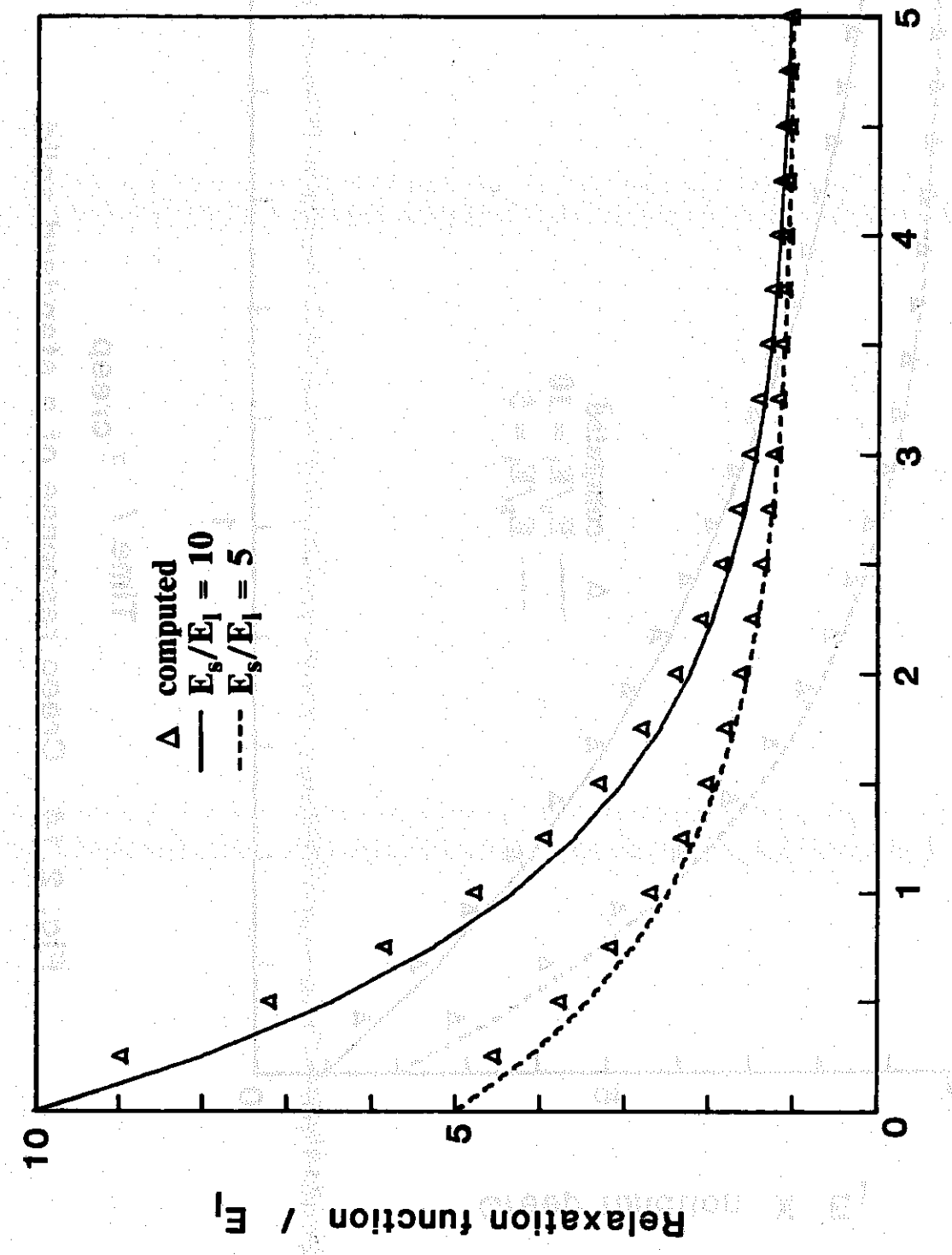

Fig. 2.15. Relaxation response of a standard solid.

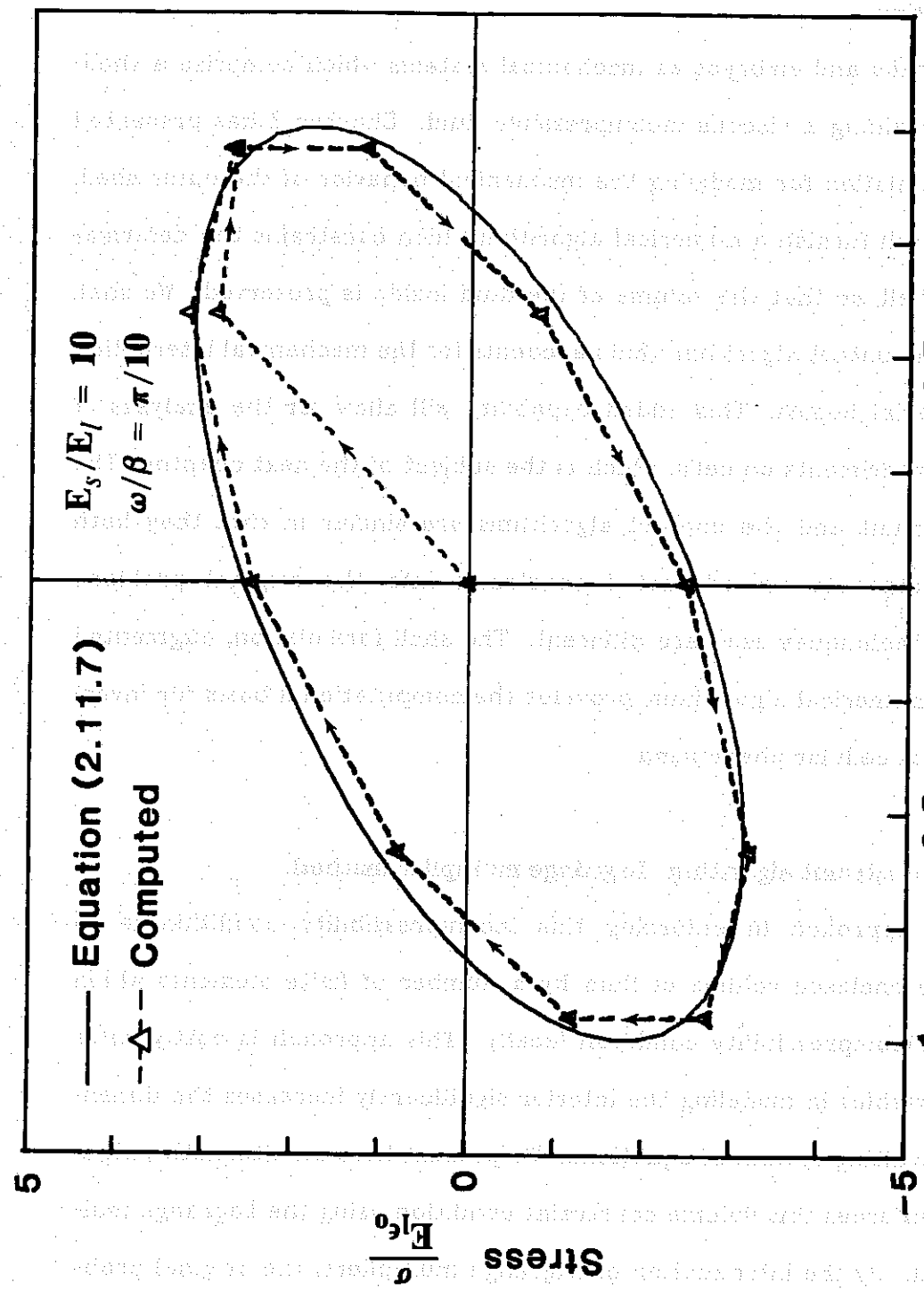

Fig. 2.16. Response of a standard solid to cyclic loading.
$\epsilon = \epsilon_0 \sin\omega t$

Chapter 3

Volume Constraint and Contact Algorithms

3.1. Introduction.

We view cells and embryos as mechanical systems which comprise a shell-like body containing a viscous incompressible fluid. Chapter 2 has presented the shell formulation for modeling the mechanical behavior of the outer shell. This chapter will furnish a numerical algorithm which constrains the deformation of this shell, so that the volume of the fluid inside is preserved. We shall also present a contact algorithm which accounts for the mechanical interaction between material bodies. This added capability will allow for the analyses of mechanical experiments on cells, which is the subject of the next chapter. The volume constraint and the contact algorithms are similar in that they both serve to incorporate an additional constraint into the original problem, although the techniques used are different. The shell formulation, augmented by these two numerical algorithms, provides the computational basis for investigating various cellular phenomena.

3.2. Volume constraint algorithm. Lagrange multiplier method.

A usual approach in enforcing this incompressibility condition is to represent the enclosed volume of fluid by a number of finite elements which ensures the incompressibility condition locally. This approach is costly since the added variables in modeling the interior significantly increases the dimension of the resulting system of equations. We present here an alternative algorithm which enforces this volume constraint condition using the Lagrange multiplier method. By the introduction of Lagrange multipliers, the original problem subjected to one or more volume constraints is transformed into an

unconstrained problem. For typical problems which involve a single volume constraint, this approach increases the total number of equations by one. Thus, the constraint can be incorporated using this approach without any appreciable increase in the computational effort.

3.2.1. Lagrange multiplier method.

The description below will assume the case of a single volume constraint, for simplicity. We denote $\mathbf{X}$ as the position vector of a typical point on the surface enclosing the volume of interest, in the reference configuration. The position vector of the same point in the deformed configuration is denoted by $\mathbf{x}$. During the loading process, the volume enclosed by the undeformed surface $V(\mathbf{X})$ takes on the value $v(\mathbf{x})$. The objective here is to constrain the deformation pattern, so that $v(\mathbf{x}) = V(\mathbf{X})$. Our appoach using the Lagrange multiplier proceeds as follows:

We first augment the total potential energy in the variational formulation by an additional term

$$\Pi^{vol}(\mathbf{x},p) = p\,[v(\mathbf{x}) - V(\mathbf{X})]\,. \tag{3.2.1}$$

Within the framework of the Lagrange multiplier method, p is the Lagrange multiplier, which can be interpreted as the pressure acting on the surface enclosing the volume of interest. The term $v(\mathbf{x}) - V(\mathbf{X})$ is the constraint condition being imposed.

The weak form corresponding to (3.2.1) is evaluated next. We first select the admissible variation of the configuration, $\delta\mathbf{x}$, as being arbitrary everywhere but vanishes at the prescribed displacement boundary, and denote the arbitrary pressure variation as δp. Then the following weak form can be constructed:

$$G^{vol}(\mathbf{x},p,\delta\mathbf{x},\delta p) = \mathbf{D}_1\Pi^{vol}(\mathbf{x},p)\cdot\delta\mathbf{x} + \mathbf{D}_2\Pi^{vol}(\mathbf{x},p)\cdot\delta p \tag{3.2.2}$$

where the differentials $\mathbf{D}_1\Pi^{vol}$ and $D_2\Pi^{vol}$ are computed from the definition of the directional derivative:

$$\mathbf{D}_1\Pi^{vol}(\mathbf{x},p)\cdot\delta\mathbf{x} = \frac{d}{d\varepsilon}\Big[\Pi^{vol}(\mathbf{x}+\varepsilon\delta\mathbf{x},p)\Big]_{\varepsilon=0}, \tag{3.2.3}$$

$$\mathbf{D}_2\Pi^{vol}(\mathbf{x},p)\cdot\delta p = \frac{d}{d\varepsilon}\Big[\Pi^{vol}(\mathbf{x},p+\varepsilon\delta p)\Big]_{\varepsilon=0}.$$

By evaluating (3.2.2) using (3.2.1) and (3.2.3), we obtain

$$G^{vol}(\mathbf{x},p,\delta\mathbf{x},\delta p) = p\,\delta\mathbf{x}\cdot\frac{\partial v(\mathbf{x})}{\partial\mathbf{x}} + \delta p\,[v(\mathbf{x}) - V(\mathbf{X})]. \tag{3.2.4}$$

In the above, $v(\mathbf{x})$ is typically a nonlinear function of the configuration $\mathbf{x}$. Thus, expression (3.2.4) has to be cast in an incremental form for computational purpose. For this, we employ the linearization procedures in Hughes and Pister [1978]. Accordingly, the current configuration is decomposed into an intermediate configuration $(\bar{\mathbf{x}},\bar{p})$ and a superposed motion $(\Delta\mathbf{x},\Delta p)$. The linear part of the weak form $G^{vol}(\mathbf{x},p,\delta\mathbf{x},\delta p)$ at the intermediate configuration $(\bar{\mathbf{x}},\bar{p})$ is defined by

$$L[G^{vol}]_{(\bar{\mathbf{x}},\bar{p})} = G^{vol}(\bar{\mathbf{x}},\bar{p},\delta\mathbf{x},\delta p) + \mathbf{D}_1 G^{vol}(\bar{\mathbf{x}},\bar{p},\delta\mathbf{x},\delta p)\cdot\Delta\mathbf{x} + D_2 G^{vol}(\bar{\mathbf{x}},\bar{p},\delta\mathbf{x},\delta p)\cdot\Delta p \tag{3.2.5}$$

By computing the differentials $\mathbf{D}_1 G^{vol}$ and $D_2 G^{vol}$ analogous to (3.2.3), the following results are obtained. First, the term $G^{vol}(\bar{\mathbf{x}},\bar{p},\delta\mathbf{x},\delta p)$ that contributes to the residual of the weak form of the equilibrium equation takes the form

$$G^{vol}(\bar{\mathbf{x}},\bar{p},\delta\mathbf{x},\delta p) = \delta\mathbf{x}\cdot p\frac{\partial v(\bar{\mathbf{x}})}{\partial\mathbf{x}} + \delta p\,[v(\bar{\mathbf{x}}) - V(\mathbf{X})] \tag{3.2.6}$$

The remaining terms contribute to the tangent stiffness, where

$$\mathbf{D}_1 G^{vol}\cdot\Delta\mathbf{x} + D_2 G^{vol}\cdot\Delta p = \delta\mathbf{x}\cdot\left[\bar{p}\frac{\partial^2 v(\bar{\mathbf{x}})}{\partial\mathbf{x}\partial\mathbf{x}}\Delta\mathbf{x} + \frac{\partial v(\bar{\mathbf{x}})}{\partial\mathbf{x}}\Delta p\right] + \delta p\frac{\partial v(\bar{\mathbf{x}})}{\partial\mathbf{x}}\cdot\Delta\mathbf{x} \tag{3.2.7}$$

Note that the "volume" tangent stiffness in (3.2.7) is symmetric.

3.2.2. Numerical procedure. Axisymmetric case.

The derivation described above is valid for a general geometrical setting. Here, we focus our attention on axially symmetric problems. For this case, the surface enclosing the volume is obtained by rotation of a prescribed meridian about an axis of symmetry. For simplicity, we shall consider the meridian to be piecewise linear.

The coordinates of each point describing the meridian have two components for axisymmetric problems -- the radial and the longitudinal components. They are referred to in what follows by the pairs $(r_I^{(i)}, z_I^{(i)})$ and $(R_I^{(i)}, Z_I^{(i)})$ for the deformed and the reference configurations, respectively. Here, the superscript (i) refers to the ith line segment (or *volume element*) making up the meridian, while I=1,2 refers to the two nodes associated with this line segment. The volume of a disc obtained by rotation of the ith line segment about the axis of symmetry is

$$V^{(i)} = \frac{\pi}{3}(Z_J - Z_I)(R_I^2 + R_I R_J + R_J^2)\Big|_{(i)} \qquad (3.2.8a)$$

for the reference configuration. The analogous formula for the deformed configuration is

$$v^{(i)} = \frac{\pi}{3}(z_J - z_I)(r_I^2 + r_I r_J + r_J^2)\Big|_{(i)} \qquad (3.2.8b)$$

The total volume, in both cases, can be obtained by summing the contributions from all the volume elements. For convenience, we shall drop the factor of $\pi/3$ in (3.1.8) in what follows, and references to line segment (i) will be implied.

We describe the deformed and the reference configurations with a fixed common frame, so that the displacement field $\mathbf{u}$ relates these two

configurations by

$$\mathbf{x} = \mathbf{X} + \mathbf{u} \tag{3.2.9}$$

It follows that

$$\delta\mathbf{x} = \delta\mathbf{u}\,, \qquad \Delta\mathbf{x} = \Delta\mathbf{u} \tag{3.2.10}$$

For each line segment (i), we write $\delta\mathbf{u}$ and $\Delta\mathbf{u}$ as

$$\delta\mathbf{u} = [\delta u_{rI}\ \ \delta u_{zI}\ \ \delta u_{rJ}\ \ \delta u_{zJ}]^T\,, \tag{3.2.11}$$

$$\Delta\mathbf{u} = [\Delta u_{rI}\ \ \Delta u_{zI}\ \ \Delta u_{rJ}\ \ \Delta u_{zJ}]^T\,,$$

where u_r and u_z denote the displacements in the r and z directions respectively. By arranging the components of $\mathbf{x}$ in the form (3.2.11), we can show using (3.2.8b) that

$$\frac{\partial v(\bar{\mathbf{x}})}{\partial \mathbf{x}} = \bar{\mathbf{K}}^{vp} \tag{3.2.12}$$

where

$$\bar{\mathbf{K}}^{vp} = [(2\bar{r}_I+\bar{r}_J)(\bar{z}_J-\bar{z}_I)\quad -(\bar{r}_I^2+\bar{r}_I\bar{r}_J+\bar{r}_J^2)\quad (2\bar{r}_J+\bar{r}_I)(\bar{z}_J-\bar{z}_I)\quad (\bar{r}_I^2+\bar{r}_I\bar{r}_J+\bar{r}_J^2)]^T\,.$$

Furthermore

$$\frac{\partial^2 v(\bar{\mathbf{x}})}{\partial \mathbf{x}\partial \mathbf{x}} = \bar{\mathbf{K}}^{vu} \tag{3.2.13}$$

where

$$\bar{\mathbf{K}}^{vu} = \begin{bmatrix} 2(\bar{z}_J-\bar{z}_I) & -(2\bar{r}_I+\bar{r}_J) & (\bar{z}_J-\bar{z}_I) & (2\bar{r}_I+\bar{r}_J) \\ -(2\bar{r}_I+\bar{r}_J) & 0 & -(2\bar{r}_J+\bar{r}_I) & 0 \\ (\bar{z}_J-\bar{z}_I) & -(2\bar{r}_J+\bar{r}_I) & 2(\bar{z}_J-\bar{z}_I) & (2\bar{r}_J+\bar{r}_I) \\ (2\bar{r}_I+\bar{r}_J) & 0 & (2\bar{r}_J+\bar{r}_I) & 0 \end{bmatrix}$$

Let the meridian describing the surface be made up of N line segments, and let $\sum_N$ denotes the assembly operator over all line segments, then the load residual term in (3.2.6) becomes

$$G^{vol}(\bar{\mathbf{x}},\bar{p},\delta\mathbf{x},\delta p) = \sum_N \begin{Bmatrix}\delta\mathbf{u}\\ \delta p\end{Bmatrix}^T \begin{Bmatrix}\bar{p}\,\bar{\mathbf{K}}^{up}\\ v(\bar{\mathbf{x}})-V(\mathbf{X})\end{Bmatrix}. \tag{3.2.14}$$

Similarly, the contribution of the stiffness matrix in (3.2.7) becomes

$$\mathbf{D}_1 G^{vol}\cdot\Delta\mathbf{x} + D_2 G^{vol}\cdot\Delta p = \sum_N \begin{Bmatrix}\delta\mathbf{u}\\ \delta p\end{Bmatrix}^T \begin{bmatrix}\bar{p}\,\bar{\mathbf{K}}^{uu} & \bar{\mathbf{K}}^{up}\\ (\bar{\mathbf{K}}^{up})^T & \mathbf{0}\end{bmatrix}\begin{Bmatrix}\Delta\mathbf{u}\\ \Delta p\end{Bmatrix} \tag{3.2.15}$$

From (3.2.14) and (3.2.15), we can extract the expressions for the stiffness matrix $\bar{\mathbf{K}}^{vol}$ and the out-of-balance load vector $\bar{\mathbf{R}}^{vol}$ to be added to their counterparts in (2.9.34):

$$\bar{\mathbf{R}}^{vol} = -\sum_N \begin{Bmatrix}\bar{p}\,\bar{\mathbf{K}}^{up}\\ v(\bar{\mathbf{x}})-V(\mathbf{X})\end{Bmatrix}. \tag{3.2.16a}$$

$$\bar{\mathbf{K}}^{vol} = \sum_N \begin{bmatrix}\bar{p}\,\bar{\mathbf{K}}^{uu} & \bar{\mathbf{K}}^{up}\\ (\bar{\mathbf{K}}^{up})^T & \mathbf{0}\end{bmatrix}. \tag{3.2.16b}$$

3.3. Contact Algorithm. Penalty Method.

Contact problems can be analyzed by the finite element method based on a number of approaches. Two commonly used approaches are the Lagrangian multiplier method (Hughes *et al* [1976] for example) and the penalty method (Kikuchi and Oden [1984] for example). Both of these methods transform the original constrained problem into an unconstrained one. The Lagrangian multiplier method incorporates the constraint by introducing additional variables to the problem. While this method ensures the contact condition to be satisfied exactly, the added variables not only increase the computational effort, but also result in the presence of zero diagonals in the stiffness matrix that requires special solution procedures. The penalty method, on the other hand, overcomes these difficulties by enforcing the contact condition approximately. The accuracy of the approximation depends on the magnitude of the penalty parameter used, although the conditioning of the problem deteriorates as this

parameter becomes large. More recent studies have tried to combine the attractive features of the two approaches. See Simo, Wriggers and Taylor [1984] and Landers and Taylor [1985] for example.

We analyze the contact problems in this study based on the penalty method. The detail of the method is furnished below for completeness.

3.3.1. Problem statement.

A contact problem involves the interaction of two bodies, in accord with the principles of continuum mechanics. For the two bodies coming into contact, the current configuration of each body is denoted by $b^\alpha, \alpha=1,2$; and the corresponding boundary of body α by ∂b^α. When portions of ∂b^1 and ∂b^2, denoted by $\partial c = \partial b^1 \cap \partial b^2$, come into contact with each other, kinematic and static requirements have to be imposed on these contact boundaries.

Let $\mathbf{n}$ denote a unit normal to ∂c. We also denote $\mathbf{X}$ and $\mathbf{x}$ as the position vectors of points in the reference and the current configurations, respectively. The position vectors for points on ∂b^α are denoted with a superscript α. Further, let $\mathbf{t}^\alpha$ be the traction vectors acting on $\partial b^\alpha, \alpha=1,2$. The contact condition can then be stated as follows:

$$\mathbf{x}^1 \cdot \mathbf{n} = \mathbf{x}^2 \cdot \mathbf{n} \tag{3.3.1}$$

$$\mathbf{t}^1 + \mathbf{t}^2 = \mathbf{0}$$

The first condition above is a kinematic requirement that no material overlapping should take place when the two bodies come into contact with each other; the second requires that equilibrium should be maintained at the same time.

3.3.2. Penalty method.

The contact condition in (3.3.1) represents an additional constraint to be imposed on the original problem. Computationally, it is convenient to transform this constrained problem to an unconstrained one, so that no special restrictions need to be imposed on the admissible displacement field.

The penalty method enforces (3.3.1) by the insertion of stiff (penalty) springs over regions where contacts are established, and the removal of these springs whenever contacts no longer persist. Mathematically, this can be achieved by augmenting the total potential energy in the variational formulation by the strain energy stored in these contact springs:

$$\Pi^{contact}(\mathbf{x}) = \frac{\tau}{2}\int_{\partial c} \mathbf{g}^T(\mathbf{x})\,\mathbf{g}(\mathbf{x})\,d\Gamma\,. \tag{3.3.2}$$

In the above, $\mathbf{g}(\mathbf{x})$ represents the amount of material overlapping over the contact region; its formal definition will be provided later. The extent of material penetration depends on the penalty parameter τ. While the impenetrability condition $\mathbf{g}\to\mathbf{0}$ can be satisfied as $\tau\to\infty$ ideally, τ can only be a large but finite number computationally. Thus the impenetrability condition is only satisfied approximately in the penalty method. Note also that (3.3.1b) is satisfied implicitly by this approach.

3.3.3. Spatial discretization.

Standard finite element techniques can be employed to discretize the bodies b^a. Here, we restrict the displacement fields to be approximated by bilinear shape functions. Thus the contact boundaries ∂b^a are represented by piecewise linear segments.

In anticipating contact problems involving large deformations, the current logic does not place the restrictive assumption of node-on-node contacts. In

this general setting, one has to consider the potential contact of an *impacting* node with a *target (master)* surface, as illustrated in Fig. 3.1. For the algorithm discussed below, the surface of the stiffer body should always be assigned as the target surface. In the case when the two bodies possess comparable stiffness, a symmetric treatment should be employed to avoid bias in the solution.

Let $\mathbf{I}$, $\mathbf{T}^\alpha$, $\alpha = 1,2$ be the position vectors of an impacting node and two nodes on a target surface, in the current configuration. The assumption of a flat target surface allows the position vector for any point on this surface $\mathbf{T}$ to be parametrized by $\xi \in [-1,1]$:

$$\mathbf{T}(\xi) = N^\alpha(\xi)\mathbf{T}^\alpha = \tfrac{1}{2}(\mathbf{T}^1 + \mathbf{T}^2) + \tfrac{1}{2}\xi\,(\mathbf{T}^2 - \mathbf{T}^1) \tag{3.3.3}$$

where

$$N^1 = \tfrac{1}{2}(1-\xi)\,; \qquad N^2 = \tfrac{1}{2}(1+\xi)\,.$$

The gap (or penetration) between the impacting node I and any point on the target place $\mathbf{T}(\xi)$ then becomes

$$\mathbf{g} = \mathbf{I} - \mathbf{T}(\xi) = \mathbf{I} - N^\alpha(\xi)\mathbf{T}^\alpha\,. \tag{3.3.4}$$

Denoting the unit vectors normal and tangent to the target surface as $\mathbf{n}$ and $\mathbf{s}$ respectively, the gaps in these directions, g_n and g_s, can be expressed as:

$$g_n = \mathbf{g}\cdot\mathbf{n} = \mathbf{I}\cdot\mathbf{n} - N^\alpha\mathbf{T}^\alpha\cdot\mathbf{n} = \mathbf{I}\cdot\mathbf{n} - \tfrac{1}{2}\bar{\mathbf{T}}\cdot\mathbf{n} \tag{3.3.5}$$

$$g_s = \mathbf{g}\cdot\mathbf{s} = \mathbf{I}\cdot\mathbf{s} - N^\alpha\mathbf{T}^\alpha\cdot\mathbf{s}$$

where $\bar{\mathbf{T}} \equiv \mathbf{T}^1 + \mathbf{T}^2$; $\mathbf{L} \equiv \mathbf{T}^2 - \mathbf{T}^1$; and $\mathbf{L}\cdot\mathbf{n} = 0$ since $\mathbf{L}$ lies normal to $\mathbf{n}$.

The case $g_n > tol$ implies the existence of gap; while $g_n \le tol$ constitutes contact. The parameter *tol* is a tolerance used to act as a safeguard against roundoff error. The case $g_n < (-tol)$ implies that penetration occurs. This occurrence is quite common in the numerical simulation of contact problems, especially those where the bodies initially have a finite gap. The penalty method

will effectively reduce the penetration to near zero, so that the true condition of contact $abs(g_n) \le tol$ is maintained.

For $\mathbf{T}(\xi)$ to be an orthogonal projection of the vector $\mathbf{I}$ onto the target surface, $g_s = 0$ has to hold. The value of ξ in this case can be determined from (3.3.5b) as:

$$\xi = \frac{\mathbf{I}\cdot\mathbf{s} - \tfrac{1}{2}\bar{\mathbf{T}}\cdot\mathbf{s}}{\tfrac{1}{2}\mathbf{L}\cdot\mathbf{s}} \tag{3.3.6}$$

A contact condition for an impacting node approaching a target surface can now be stated:

$$g \le tol \; ; \qquad abs(\xi) \le 1 \; . \tag{3.3.7}$$

3.3.4. Contact stiffness matrix and load vector.

With the definition of $\mathbf{g}$ established in (3.3.4), the potential energy of the contact springs in (3.3.2) can be rewritten in a discrete form:

$$\Pi^{contact}(\mathbf{x}) = \frac{\tau}{2}\sum_{M}(\mathbf{x}^c)^T(\Phi^c)^T\Phi^c\mathbf{x}^c \tag{3.3.8}$$

where $\mathbf{x}^c \equiv [\mathbf{I}\ \mathbf{T}^1\ \mathbf{T}^2]^T \in \mathbf{x}$; $\Phi^c \equiv [1\ -N^1\ -N^2]$; M is the total number of target surface segments currently in contact with the opposite surface, and $\sum_M$ represents an assembly operator over M surface segments.

The finite element formulation following this is standard for nonlinear problems. First, we select the admissible variation of the configuration, $\delta\mathbf{x}$, as being arbitrary everywhere but vanishes at the prescribed displacement boundary. The weak form associated with (3.3.8) takes the following form:

$$G^{contact}(\mathbf{x},\delta\mathbf{x}) = \mathrm{D}\Pi^{contact}(\mathbf{x})\cdot\delta\mathbf{x} = \frac{d}{d\varepsilon}\Big[\Pi^{contact}(\mathbf{x}+\varepsilon\delta\mathbf{x})\Big]_{\varepsilon=0} \tag{3.3.9}$$

$$= \tau\sum_{M}(\delta\mathbf{x}^c)^T(\Phi^c)^T\Phi^c\mathbf{x}^c$$

where $\delta\mathbf{x}^c \in \delta\mathbf{x}$.

Equation (3.3.9) is nonlinear because the contact area varies nonlinearly with the applied loading; its solution therefore requires a linearization procedure. Again we employ that as outlined in Hughes and Pister [1978], in which the current configuration is decomposed into an intermediate configuration $\bar{\mathbf{x}}$ and a superposed motion $\Delta\mathbf{x}$. The linear part of the weak form $G^{contact}(\mathbf{x},\delta\mathbf{x})$ at the intermediate configuration $\bar{\mathbf{x}}$ is therefore

$$L[G^{contact}]_{\bar{\mathbf{x}}} = G^{contact}(\bar{\mathbf{x}},\delta\mathbf{x}) + DG^{contact}(\bar{\mathbf{x}},\delta\mathbf{x})\cdot\Delta\mathbf{x} \tag{3.3.10}$$

By describing the deformed and the reference configurations with a fixed common frame, the displacement field $\mathbf{u}$ can be expressed as

$$\mathbf{x} = \mathbf{X} + \mathbf{u}\,. \tag{3.3.11}$$

It follows that

$$\delta\mathbf{x} = \delta\mathbf{u}\,; \qquad \Delta\mathbf{x} = \Delta\mathbf{u}\,. \tag{3.3.12}$$

Thus, the *contact force* vector $\bar{\mathbf{F}}^{contact}$ and the *contact tangent stiffness* matrix $\bar{\mathbf{K}}^{contact}$ can be extracted from (3.3.10). These contributions, as listed below, are to be added to the tangent stiffness matrix and the load vector in (2.9.34):

$$\bar{\mathbf{F}}^{contact} = -\tau \sum_{M} (\bar{\boldsymbol{\Phi}}^c)^T \bar{\boldsymbol{\Phi}}^c \bar{\mathbf{x}}^c \tag{3.3.13a}$$

$$\bar{\mathbf{K}}^{contact} = \tau \sum_{M} (\bar{\boldsymbol{\Phi}}^c)^T \bar{\boldsymbol{\Phi}}^c \tag{3.3.13b}$$

The additional contributions do not affect the size of the original problem. However, changes in the profile of the tangent stiffness matrix are likely because of the additional coupling of the degrees of freedom associated with the contacted nodes.

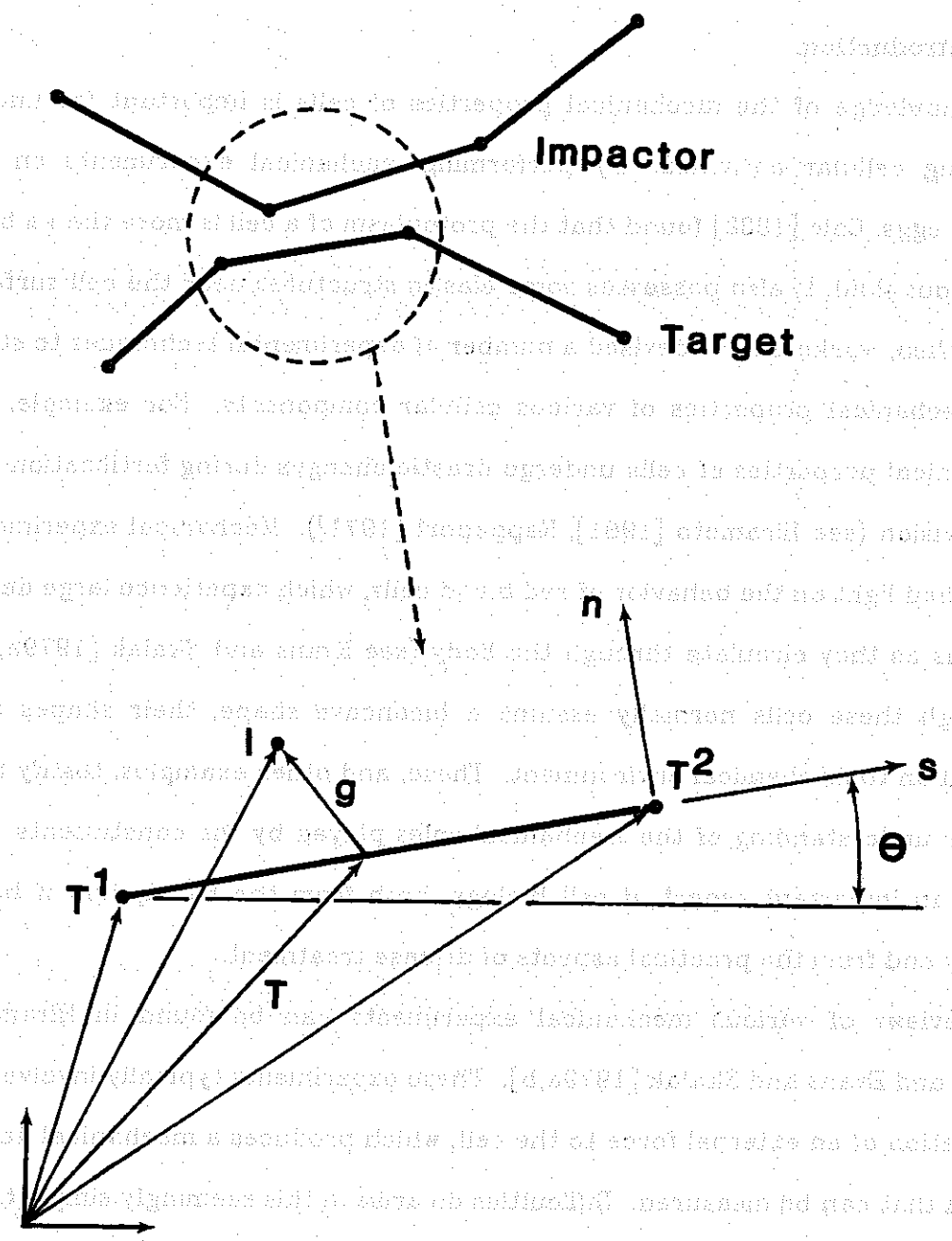

Fig. 3.1. Geometry of Contact.

Chapter 4

Analyses of Mechanical Experiments on Sea Urchin Eggs

4.1. Introduction.

Knowledge of the mechanical properties of cells is important for understanding cellular activities. By performing mechanical experiments on sea urchin eggs, Cole [1932] found that the protoplasm of a cell is more than a body of viscous fluid, it also possesses some elastic structures near the cell surface. Since then, workers have devised a number of experimental techniques to study the mechanical properties of various cellular components. For example, the mechanical properties of cells undergo drastic changes during fertilization and cell division (see Hiramoto [1981], Rappaport [1971]). Mechanical experiments have shed light on the behavior of red blood cells, which experience large deformations as they circulate through the body (see Evans and Skalak [1979a,b]). Although these cells normally assume a biconcave shape, their shapes also depend on their chemical environment. These, and other examples, testify that a clear understanding of the mechanical roles played by the constituents of a cell is an important aspect of cell biology, both from the standpoint of basic biology and from the practical aspects of disease treatment.

Reviews of various mechanical experiments can be found in Hiramoto [1970] and Evans and Skalak [1979a,b]. These experiments typically involve the application of an external force to the cell, which produces a mechanical deformation that can be measured. Difficulties do arise in this seemingly simple task. First, the size of many cells is extremely small. At this microscopic level, accurate control and measurement of forces and displacements becomes a major obstacle for the experimentalist. Second, the experiments only measure properties of a cell as a whole; unless one can design *extremely* small and sensitive

strain gauges, the mechanical properties of cells must be deduced analytically. The analysis of these mechanical experiments is the focus of this chapter.

Analyses of mechanical experiments presented in the past have largely relied on simplifying assumptions made so that the mathematics remains tractable. Implicit in many of these analyses is the assumption that the tension in the membrane of the cell is uniformly distributed over the cell surface. Another common assertion is that at every point on the surface the dominant force resultant in the membrane is the *isotropic* tension (equal tensions in all directions tangent to the membrane surface). While these assumptions are appropriate for some situations, they are not valid in general.

Other issues also arise from these approximate analyses. Often the material property in question, e.g. the Young's modulus of the membrane, is correlated with data that are difficult to measure accurately, leading to large uncertainties in the result.

In the following section we present a model for analyzing mechanical experiments based on the finite element method (see Zienkiewicz [1977]). By minimizing the total energy in the mechanical system, this method automatically computes the deformed configuration as well as the distributions of stress and strain resulting from the applied loading. This avoids a number of assumptions made in earlier approximate analyses. Furthermore, since the method can be applied to problems with arbitrary geometry, it is capable of treating a number of mechanical experiments in a unified manner. Thus given an estimate of the mechanical property data, several mechanical experiments can be simulated to provide a broad basis for assessment, which increases our confidence in the reliability of the data.

To illustrate the use of the finite element analysis method, three commonly used mechanical experiments will be analyzed: (1) the compression experiment;

(2) the suction (micropipette aspiration) experiment; and (3) the magnetic particle experiment. Discussions presented here are based on unfertilized sea urchin eggs as experimental materials, although the analysis method is not limited to this particular species.

We shall simulate only the deformation of the egg at steady state, when all viscous effects have vanished. During that time, the egg can be viewed mechanically as a body of incompressible material enclosed by an elastic membrane layer. This thin membrane layer (on the order of several μm thick) is assumed to resist only in-plane tensions; the bending stiffness of the membrane neglected (see Evans and Skalak [1979a]).

The simulations of these mechanical experiments consist of three ingredients whose details have been presented in the previous chapters. First, we model the cortex of the egg by the axisymmetric membrane elements described in Chapter 2. The material within this membrane is assumed to be linearly elastic (see eq. (2.8.5)). Second, we ensure that the volume enclosed by the membrane is constant throughout the deformation history by using the volume constraint algorithm discussed in Chapter 3. Finally, we simulate the mechanical contact condition between the egg and the loading apparatus by the contact algorithm discussed in Chapter 3. In all cases, the analysis is valid for large deformations.

The mechanical data for unfertilized sea urchin eggs are obtained from published reports on deformation experiments. We assume the diameter of an egg to be 100 μm (95-100 μm based on Yoneda [1964] and Hiramoto [1970]) and that the egg membrane is initially stretched. For unfertilized sea urchin eggs, Mitchison and Swann [1954a] estimated the upper limit of this initial stretch to be roughly 14 percent. Here, a representative value of 5 percent, as assumed by Hiramoto [1963], is used. By assuming that a material is isotropic and linearly

elastic, its behavior can be characterized by two elastic constants: the Young's modulus (E) and the Poisson's ratio (ν). Workers studying membrane elasticity frequently use the ***surface elasticity modulus*** (Et), defined by the product of the Young's modulus times the membrane thickness, rather than the Young's modulus itself, since the cortical thickness is not easily measureable. The value of Et derived from various mechanical experiments ranges from 0.37 - 1.6 ***dyn/cm*** (Hiramoto [1970]). Here, we assume the surface elasticity modulus (Et) and the Poisson's ratio (ν) to be 0.5 ***dyn/cm*** and 0.5, respectively. This set of mechanical data for unfertilized sea urchin eggs are summarized in Box 4.1. We shall employ this same set of mechanical data for simulations of the three mechanical experiments described next.

Box 4.1. Mechanical property data for unfertilized sea urchin egg

Diameter	100 μm
Initial stretch	5%
Elasticity modulus Et	0.5 dyn/cm
Poisson's ratio ν	0.5

4.2. Compression Experiment.

The compression experiment involves squeezing an egg between two parallel plates, as illustrated in Fig. 4.1a. Cole [1932] first used the experiment to establish that the cortex of a sea urchin egg possesses some elastic structure. Hiramoto [1963] and Yoneda [1964], and more recently Evans and Skalak [1979b], have further analyzed the experiment and provided estimates of the surface forces as well as the elastic modulus of the cell membrane.

The method of calculation by Cole [1932], and later modified by Hiramoto [1963], is as follows. Given the current geometry of the egg, the surface forces $N^{\eta\eta}$ (or N_φ) and $N^{\vartheta\vartheta}$ (or N_ϑ) in directions of the meridian and the equator, respectively, can be derived based on equilibrium considerations alone. Consider a typical point on the equator; let $A = \pi R_c^{\,2}$ be the area of contact; F be the total applied force; and R_1 and R_2 be the principal radii of curvature at that point, as shown in Fig. 4.1a. The equilibrium equations are:

$$\frac{N^{\vartheta\vartheta}}{R_2} + \frac{N^{\eta\eta}}{R_1} = \frac{F}{A} \tag{4.1a}$$

$$2\pi R_2 N^{\eta\eta} + F = \pi R_2^{\,2} F / A \tag{4.1b}$$

In the above expression, A, R_1 and R_2 are experimentally measured from photographs of the eggs. These quantities, together with the known applied force F, can be used to compute the surface forces $N^{\eta\eta}$ and $N^{\vartheta\vartheta}$. Hiramoto [1963] further developed the equation to determine the Young's modulus based on these data.

As pointed out by Mitchison and Swann [1954b], the major difficulty associated with this approach lies in the accurate measurement of the area of contact from photographs. Other procedures developed by Yoneda [1964] and Evans and Skalak [1979b] were able to eliminate the dependence on the area A. However, these analyses had to assume that the egg membrane was in a state of isotropic tension. The numerical simulation discussed below does not require such an assumption, since it automatically computes the area of contact based on kinematics and equibrium considerations. Therefore this method allows more accurate representation of the experiment, and provides an assessment of various approximations employed by workers.

4.2.1. Compression experiment -- modeling.

As shown in Fig. 4.1b, the model represents the symmetric half of an egg compressed by a rigid flat plate. We model the membrane of the egg with forty membrane elements; and maintain the volume enclosed by these elements to be constant. We consider the plates compressing the egg to be rigid, and the friction between the plates and the egg as negligible.

In the simulation, we apply the loads to the egg numerically over a number of load steps. The first step prestretches a stress-free spherical egg by 5 percent. As prestretching is completed, the egg reaches a diameter of 100 μm, and each pole of the egg touches the plate. The subsequent load steps simulate the compression of the egg at a closure increment of 10 μm per step. The force required to produce this prescribed deformation is then computed in the analysis.

4.2.2. Compression experiment -- results and discussions.

Fig. 4.2 shows the deformed shapes of the egg superimposed throughout the loading history. To compare these predicted geometric forms with measurements from experiments, the graph of the relative radius $r_2 \equiv R_2 \,/\, Z_o$ versus the relative thickness $z \equiv Z \,/\, Z_o$ is plotted in Fig. 4.3, where Z_o is the initial diameter of the egg. These results are in close agreement with those obtained from the average of about twenty photographic records.

The force-closure displacement curve in Fig. 4.4 shows that the response of the egg to compression is stiffer at large closures. This data trend, as well as the actual magnitude of the forces, compare well with the experimental data. At large closures, the computed curve deviates more from the experimental curve. This possibly reflects the gradual weakening of the cortex as observed by Yoneda [1964], which has not been accounted for in this simulation.

Figs. 4.5 and 4.6 show the comparisons of the computed contact area with results from experiments. It may appear that these results deviate more for larger radius. In fact, the contact area is computed by squaring the contact radius obtained from the computation. Thus, any deviation of the computed from the experimental data is magnified in proportion to the radius squared. Nevertheless, the predictions agree well with the data measured photographically, and roughly form an upper bound for the Brownian motion data of Yoneda [1964]. The simulation also shows that the pressure distribution over the contact surface is approximately uniform.

The distribution of the surface forces over the entire surface of the egg at various heights are shown superimposed in Fig. 4.7. These results support the findings of Cole [1932] and Hiramoto [1963] that surface forces increase with increasing closures. At low to moderate closure displacements ($z \leq 0.5$), tensions remain roughly uniform over the region of the egg which is not yet in contact with the plate. This is because the influence of the contact region is not significantly felt near the equator at these stages. As the egg is further compressed, the state of tension becomes nonuniform.

There has been much dispute regarding the state of tension in the egg membrane. Cole [1932], Yoneda [1964] and Evans and Skalak [1979b] concluded that isotropic tension was dominant because the membrane at the equator exhibited constant total curvature; whereas Hiramoto [1963] estimated that the ratio of hoop tension to meridianal tension was about 1.5 to 2 based on the calculation outlined above. The results in Fig. 4.7 support Hiramoto's view. The tension ratio is about 1.5 at various closure displacements.

This result can be better understood by examining the strain variation at the equator throughout the deformation history, as shown in Fig. 4.8. At small closure displacement, Fig. 4.8 reveals that the meridianal strain actually

decreases while the hoop strain increases. This finding is in accord with the observation of Hiramoto [1967]. As a result, the hoop strain is larger than the meridianal strain by as much as sevenfold. For an elastic membrane, the surface forces computed from strains with this large difference are not likely to be isotropic.

In summary, employing estimates of the membrane elastic properties by Hiramoto [1963], the present study has predicted results that are consistent with various experimental observations. Therefore, one can conclude that the contact area measurement of Hiramoto [1963] is roughly correct, despite others' doubt about its accuracy. Furthermore, the simulations have shown that the membrane is not in isotropic tension when compressed. Methods that rely on this assumption need to be reexamined. Hiramoto [1967] has pointed out that the analysis of Yoneda [1964] would lead to a serious error in estimating the surface forces if the membrane was not in isotropic tension. The results here show that this is indeed the case.

4.3. Suction Experiment.

This method of measuring the elastic properties of sea urchin eggs was introduced by Mitchison and Swann [1954a]. Rand and Burton [1964] later utilized the technique for work on red blood cells. Since then, the method has gained wide acceptance in both fields, and has become one of the standard methods for determining the elastic properties of cell membranes. By employing a pipette with internal diameter smaller than that of the cell, a suction pressure is applied to a part of the cell surface, as shown in Fig. 4.9a. The displacement of the cell surface into the pipette caused by this pressure provides a measure of the "stiffness" of the cell surface.

Various attempts have been made to convert this "stiffness" value into elastic properties of the cell membrane. Mitchison and Swann [1954a] analyzed the problem based on membrane theory. They assumed that no adhesion or friction existed between the pipette and the cell membrane, so that the membrane tension was uniform over the entire cell surface. This surface tension was further considered as isotropic. Their analysis is as follows. Equations of equilibrium for the cell membranes inside and outside the pipette are:

$$P_i - P_p = \frac{2T}{r} \tag{4.2a}$$

$$P_i - P_o = \frac{2T}{R} \tag{4.2b}$$

where T is the isotropic surface tension; P_i, P_o and P_p are the fluid pressures inside and outside the cell and in the pipette, respectively, as shown in Fig. 4.9b. The radii of curvature of the cell surface inside and outside the pipette (r and R respectively) characterizes the geometry of the deformed cell, as illustrated in Fig. 4.9a. By eliminating P_i in (4.2a) and (4.2b), an expression for the pipette aspiration pressure P ($= P_o - P_p$) is established:

$$P = P_o - P_p = 2T\left(\frac{1}{r} - \frac{1}{R}\right) \tag{4.3}$$

Another relation can be derived from the egg's geometry shown in Fig. 4.9a:

$$r^2 = \left(\frac{d}{2}\right)^2 + (r-x)^2 . \tag{4.4}$$

Combining (4.3) and (4.4) gives

$$P = 2T\left[\frac{2x}{x^2 + d^2/4} - \frac{1}{R}\right] \tag{4.5}$$

Equation (4.5) gives a relation of P versus x. However, a plot of (4.5) shows that this curve is concave towards the x-axis, whereas the experimental curves

are almost linear (Mitchison and Swann [1954a]). This discrepancy seems to result from the assumption that tension remains as constant with increasing deformation, when it probably increases due to the elasticity of the cell surface (Hiramoto [1970]).

Evans *et al* [1976] also used (4.3) as the basis for their study of preswollen red blood cells, which experience large isotropic tensions. Together with the data for p versus x, they derived the relation of the membrane isotropic tension versus fractional increase in area of the cell surface.

Richardson [1975] employed a different approach to determine the elastic moduli for red blood cell membranes. Assuming the cell membrane "sticks" to the pipette mouth (i.e. no-slip assumption), the deformity of the cell membrane inside the pipette was modeled as the inflation of a spherical cap. The solution of this problem was obtained by solving the membrane equations with an iterative procedure. Among other findings, the results showed that the state of tension was not isotropic at every point on the cell membrane.

Analyses such as these have provided workers with estimates of the elastic properties of cell membranes. However, the quality of these estimates largely depends on whether the various assumptions made in the analytical model are valid. One of the most important, but perhaps the least understood assumptions regards the frictional interaction between the cell membrane and the pipette.

It is very difficult to assess directly the effect of friction on stiffness measurements. Mitchison and Swann [1954a] observed that the surface of a sea urchin egg does slip over the edge of the pipette; however, most other cells of interest are too small for direct observation. Furthermore, the amount of friction (or slipping) may vary from one test specimen to another, and from one species to another. An alternative to studying friction directly is to investigate

the extreme situations: (1) the case in which friction is very large, allowing no slip, and (2) the case in which no friction exists at the interface.

Most previous analyses have assumed either the no-slip or the no-friction condition; however, the theoretical analyses were often specialized to the point that only one of the two extreme situations could be treated. As a result, no direct comparisons of these two extreme cases have been made. The finite element method developed here is capable of analyzing both of these situations, and so it provides a means for their direct comparisons. The results of the simulations suggest that friction has a subtle effect on the response of a cell to suction pressure.

4.3.1. Suction experiment – modeling.

Similar models are employed for the case of no-slip and that of no-friction. For both cases, we assume a spherical initial configuration (Fig. 4.10). We model the portion of the membrane inside the pipette using ten membrane elements, and the remaining portion by thirty membrane elements. For the no-friction case, in which slipping of the egg membrane over the pipette mouth is anticipated, meshing is finer near that region. We also maintain the volume enclosed by the entire surface of the egg as constant at all times.

The analyses employ pipettes with inner diameter of 50 μm for suctioning sea urchin eggs, whose diameter is roughly 100 μm. Mitchison and Swann [1954a] found this pipette/egg diameter ratio to give the best accuracy in measuring deformations. Here, the inner wall of the pipette plays the role of a contact surface, and is assumed to be rigid. Accordingly, the contact algorithm constrains the inflation of the egg surface to take place within the inner space of the pipette.

The relative positioning of the egg membrane and the pipette depends on the following factors. First, the egg is to be prestretched by 5 percent to reach a diameter of 100 μm, and that the prestretched egg and the pipette mouth then contact each other. Another issue is the contact condition (no-slip or no-friction) at the egg membrane/pipette mouth interface. For the no-slip case, the egg and the pipette are placed such that they are in contact at the stress-free stage (Fig. 4.10a), and a point on the egg is held fixed at the pipette mouth at all times. This not only accounts for the no-slip assertion, but also provides a boundary condition that eliminates rigid body motions. For the no-friction case, in which points on the egg surface are allowed to move over the pipette mouth, the rigid body motions have to be excluded in a different way. For this, the model employs an artificial spring with very little stiffness at the top of the egg, as shown in Fig. 4.10b. We add this spring in such a way that the accuracy of the solution to the original problem is maintained, at the expense of somewhat compromising the convergence rate of the solution (contribution only added to the stiffness matrix, but not to the unbalanced load). For this no-friction case, we prescribe a gap between the egg and the pipette, as illustrated in Fig. 4.10b, so that they touch each other after the egg is prestretched. Once this contact is established, the artificial spring is no longer required.

The simulation of the suction experiment proceeds in a sequence of loading steps. The first step involves prestretching the egg by 5 percent. The suction pressure is then applied to the membrane inside the pipette at increments of 30 dyn/cm^2, based on the formulation outlined in Section 2.10.

4.3.2. Suction experiment -- results and discussions.

Fig. 4.11 shows the superposed aspirated shapes of the egg, for the cases of no-slip and of no-friction. Comparison of these shapes indicates that friction does not significantly affect the deformations of the egg. A close-up view of the predicted membrane movements near the pipette mouth is shown in Fig. 4.12. Here, the outline of the egg membrane is traced by a number of nodes. Arrows are drawn to trace the path that each of these nodes takes throughout the deformation history. For the no-slip case, all arrows are found inside the pipette. Nodes inside the pipette converge towards the pipette wall, and adhere to the location of first contact on the wall, whereas those outside of the pipette mouth tend to remain stationary. Examination of the no-friction case shows that the nodes move over the pipette mouth and progress downward along the pipette wall. This was observed on sea urchin eggs by Mitchison and Swann [1954a].

This difference in the sliding characteristics between the two cases has virtually no influence on the pressure/displacement curve, as shown in Fig. 4.13. Both curves exhibit near linear behavior, and compare well with the experimental data of Mitchison and Swann [1954a]. In the figure, the slope of the no-slip curve is slightly steeper than that of the no-friction curve. This is reasonable since the no-slip condition constrains the deformation of the egg, thereby stiffening its response to external loadings.

Figs. 4.14 and 4.15 provide side-by-side comparisons of the spatial distributions of tensions and strains in their principal directions. While workers have believed that friction may significantly affect the distribution of tension over the egg surface, the results indicate that the distributions are almost identical for the two cases. Furthermore, the tension exerted on the membrane inside the pipette far exceeds that outside the pipette. This implies that the combined

actions of the tension of the membrane inside the pipette and the reaction force exerted by the pipette mouth nearly counterbalance the net force due to the suction pressure. The difference between these force components is then taken up by the tension in the membrane outside the pipette. A force balance check at the pipette mouth shows that this is indeed the case.

Despite all indications that the effect of friction is not important to the overall response of the egg to suction pressure, there remains an important difference between the no-slip and the no-friction cases. This requires a close examination of Figs. 4.14 and 4.15. While the membrane is stretched over the entire egg surface in the no-slip case, it is not so in the no-friction case. In the region near the pipette mouth, the membrane is stretched along the meridianal direction, yet compressed along the hoop direction. Compression in the membrane arises here since the model has assumed that the membrane has equal resistance for both tension and compression. In reality, thin membranes have extremely low resistance to compression; thus any slight amount of compression causes the membrane to fold. When this type of instability takes place, the aspirated shape may not remain axisymmetric. Therefore, this seemingly minor difference between the two cases has significant implications to the behavior of the egg. Since some degree of friction exists in most cases, the egg may therefore deform in an axisymmetric mode initially. Folding may then occur at some point, beyond which the deformation assumes an asymmetric buckled mode. Although this phenomenon has not been reported for sea urchin eggs, it is commonly observed when red blood cells are aspirated (see Evans [1983]).

4.4. Magnetic Particle Experiment.

Hiramoto first introduced this experiment to study the mechanical properties of protoplasm in sea urchin eggs (Hiramoto [1969a,1969b,1970]). An iron particle of 5 to 7 μm in diameter is first placed inside the egg, and an electromagnetic force is applied to induce movements of the particle. The speed at which the particle moves inside the protoplasm gives a measure of the viscoelastic properties of the egg. Hiramoto [1974] employed the same technique to measure the mechanical properties of the cortical membrane. There, the particle is first drawn near the surface of the egg. Applying the electromagnetic force results in the bulging of the egg membrane near the particle. This gives the relation between the height of this bulge and the applied force, which measures the stiffness of the membrane.

It is difficult to establish an approximate solution for this mechanical problem. Evans and Skalak [1979b] employed a numerical solution to compute the force-displacement relation. They assumed the tensions in the egg membrane to be dominated by isotropic tension. Here, we employ the finite element method to analyze the experiment, to demonstrate further the applications of the method.

4.4.1. Magnetic particle experiment -- modeling.

The model employs 30 membrane elements to represent the top half of the egg, as shown in Fig. 4.16. In order to capture the detailed deformed shapes at large deformations, the mesh is more refined at the region near the particle. The egg membrane is restrained from vertical movements at the equator. Throughout the analysis, the volume of the entire egg is constrained to be constant. The model assumes the iron particle to be rigid; the contact algorithm simulates the mechanical contact at the particle-membrane interface

accordingly.

As in the previous simulations, the loading sequence is carried out in a sequence of load steps. The first step involves prestressing the egg by 5 percent. The unstressed egg is sized such that its diameter is 100 μm when stressed. Following this prestress operation, the entire particle is displaced upward at a constant rate. The force required to stretch the egg membrane is later determined in the analysis.

4.4.2. Magnetic particle experiment -- results and discussions.

The deformed shapes for increasing electromagnetic force are shown superimposed in Fig. 4.17. While the applied force draws out the egg surface near the particle, the displacement of the internal volume causes the lateral dimension of the egg to decrease slightly, so that the total volume of the egg is conserved. As a result, the hoop tension near the equator drops when tensions near the particle continue to rise (see Fig. 4.18).

Figure 4.18 also illustrates that membrane stretching mainly occurs near the particle. The stiffness value of the membrane obtained by this method therefore reflects a local membrane property. For this reason, the method is useful to detect possible difference in mechanical preperties over various regions of the egg.

The applied force versus the height of the bulge shown in Fig. 4.19 exhibits a stiffening behavior. This agrees with the prediction of Evans and Skalak [1979b]. However, there is hardly any experimental data available for comparison purposes. The curve in Fig. 4.19 compares well with the single force-displacement data given in Hiramoto [1974]. More data are needed to judge the quality of the predictions this simulation makes.

4.5. Closure.

We have demonstrated here that the finite element tools developed in Chapters 2 and 3 are useful in analyzing various mechanical experiments on cells. We believe this approach is not only useful for determining mechanical properties of cells, but it also gives insights that approximate analyses cannot provide. Based on the finite element analyses, we now understand the role of friction in the suction experiment. We are better able to judge the validity of various assumptions workers have made in their efforts to determine the mechanical property data. With these insights, we can design improved methods which may yield better data. Since the finite element approach imposes few restrictions on the geometry of the problem, we need not concern ourselves with the geometric complexities while designing improved experiments.

Although we have restricted our discussion to unfertilized sea urchin eggs, the methodology applies equally to other cells and tissues. In modeling red blood cells, we will need to account for its large resistance to area deformation. Details of the formulation have already been worked out in Evans and Skalak [1979a]. By including the bending effect, the method can also analyze experiments on thick tissues. Finally, we can investigate mechanisms underlying various developmental events in fertilized eggs. There, we need to model the simultaneous actions of the natural event (such as cytokinesis, gastrulation, etc.) and the external influence the experiment imposes.

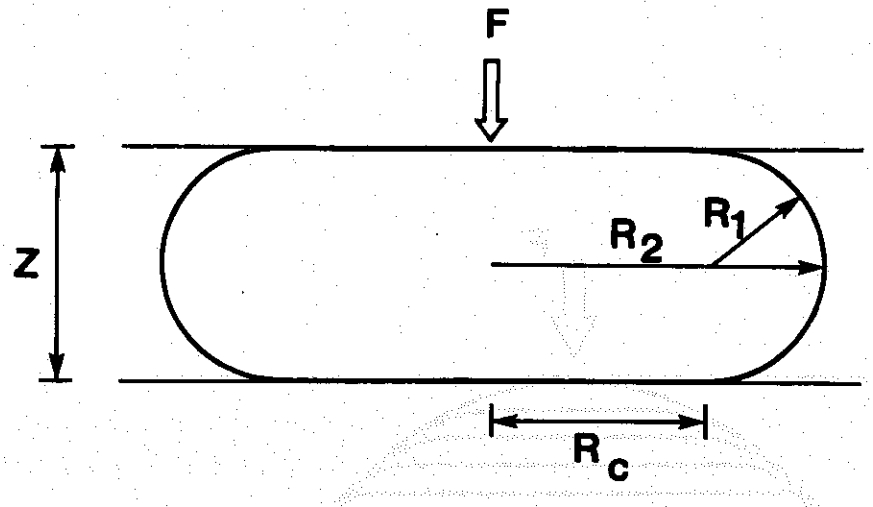

Fig. 4.1a. The compression of an egg.

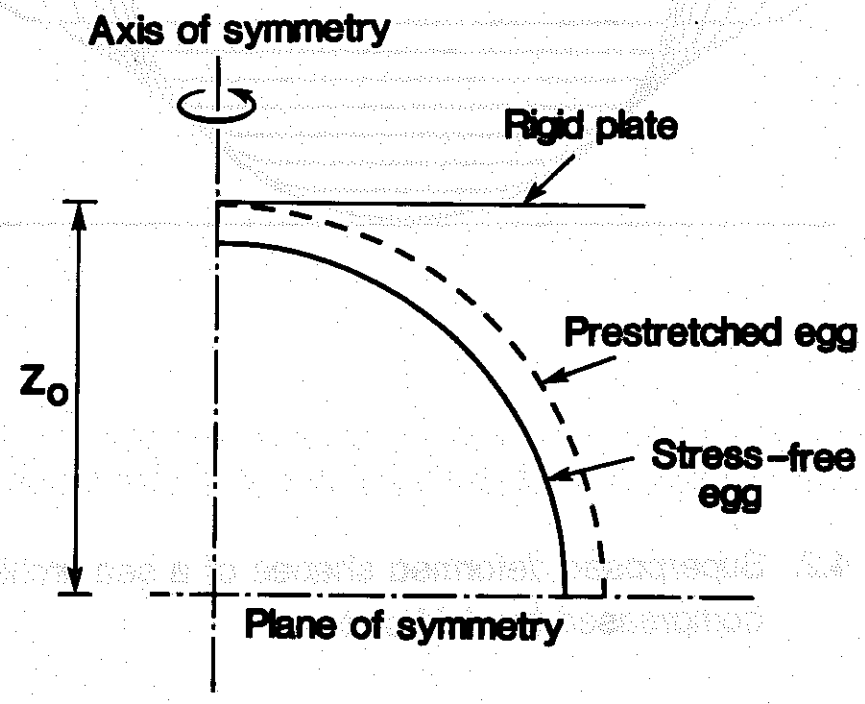

Fig. 4.1b. Analysis model for the compression experiment.

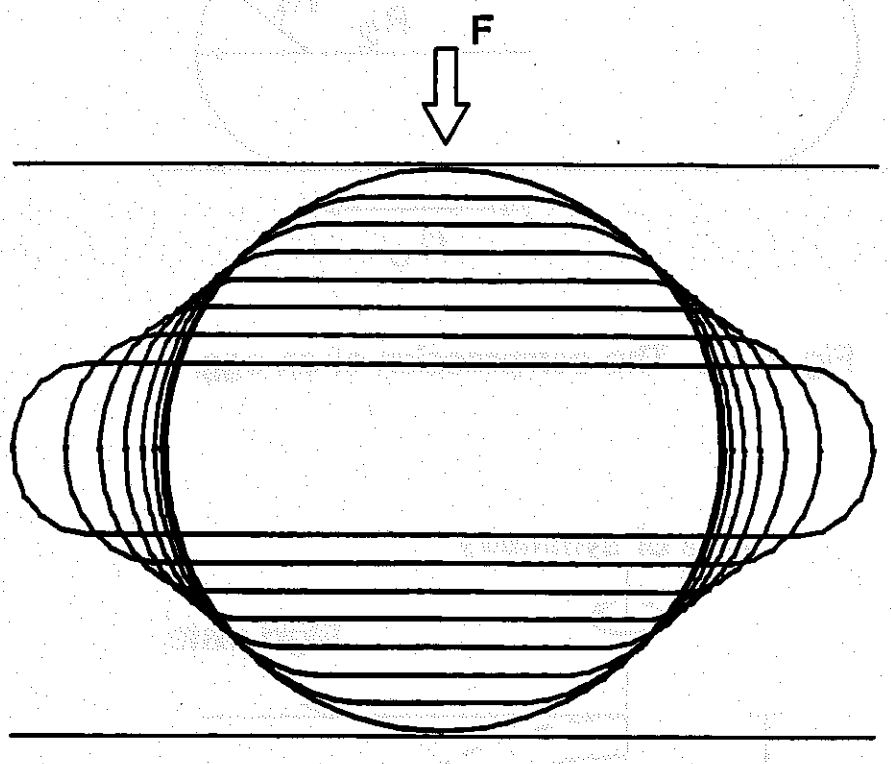

Fig. 4.2. Superposed deformed shapes of a sea urchin egg compressed by rigid plates.

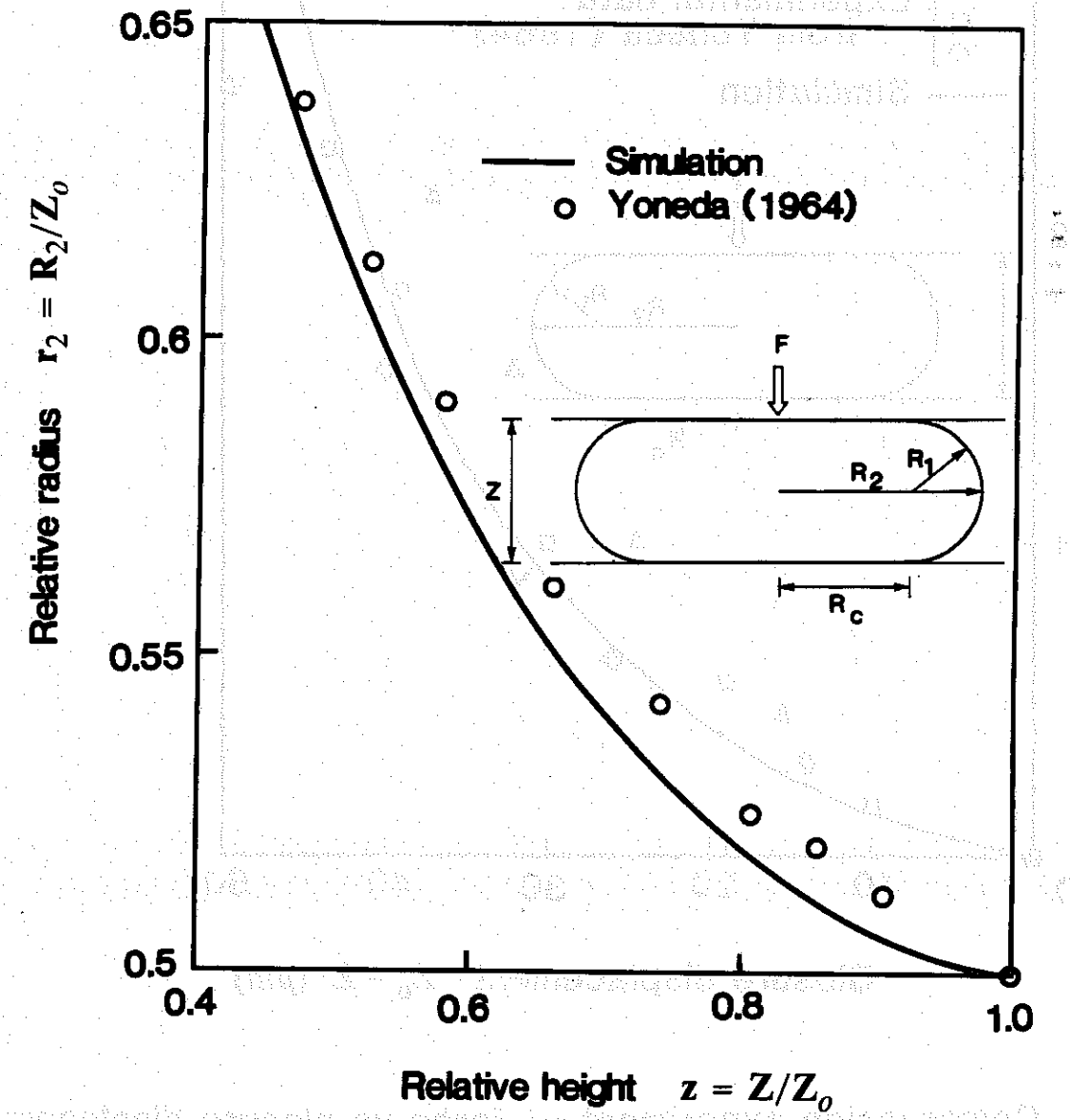

Fig. 4.3. Compression experiment — radius vs height.

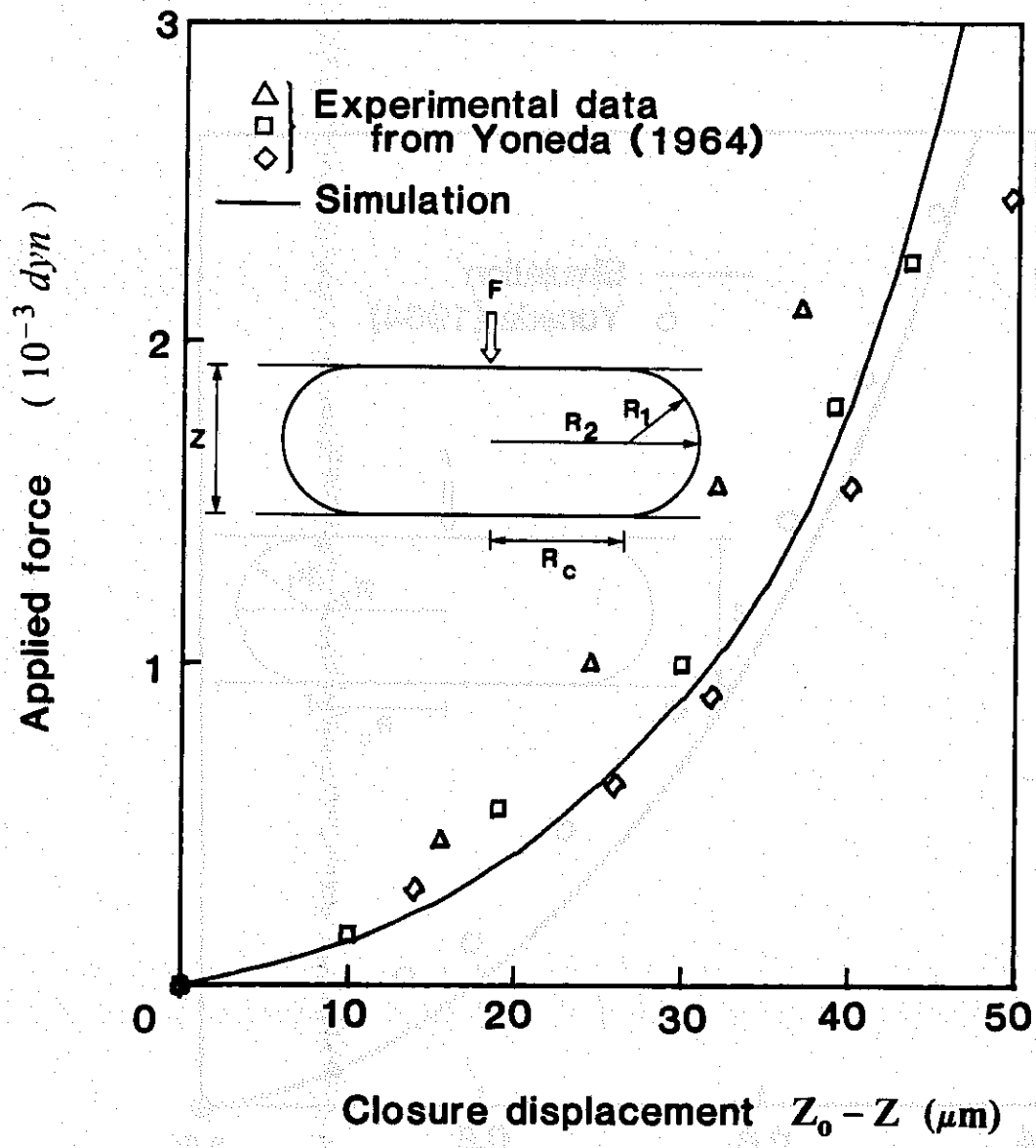

Fig. 4.4. Compression experiment -- force vs closure displacement.

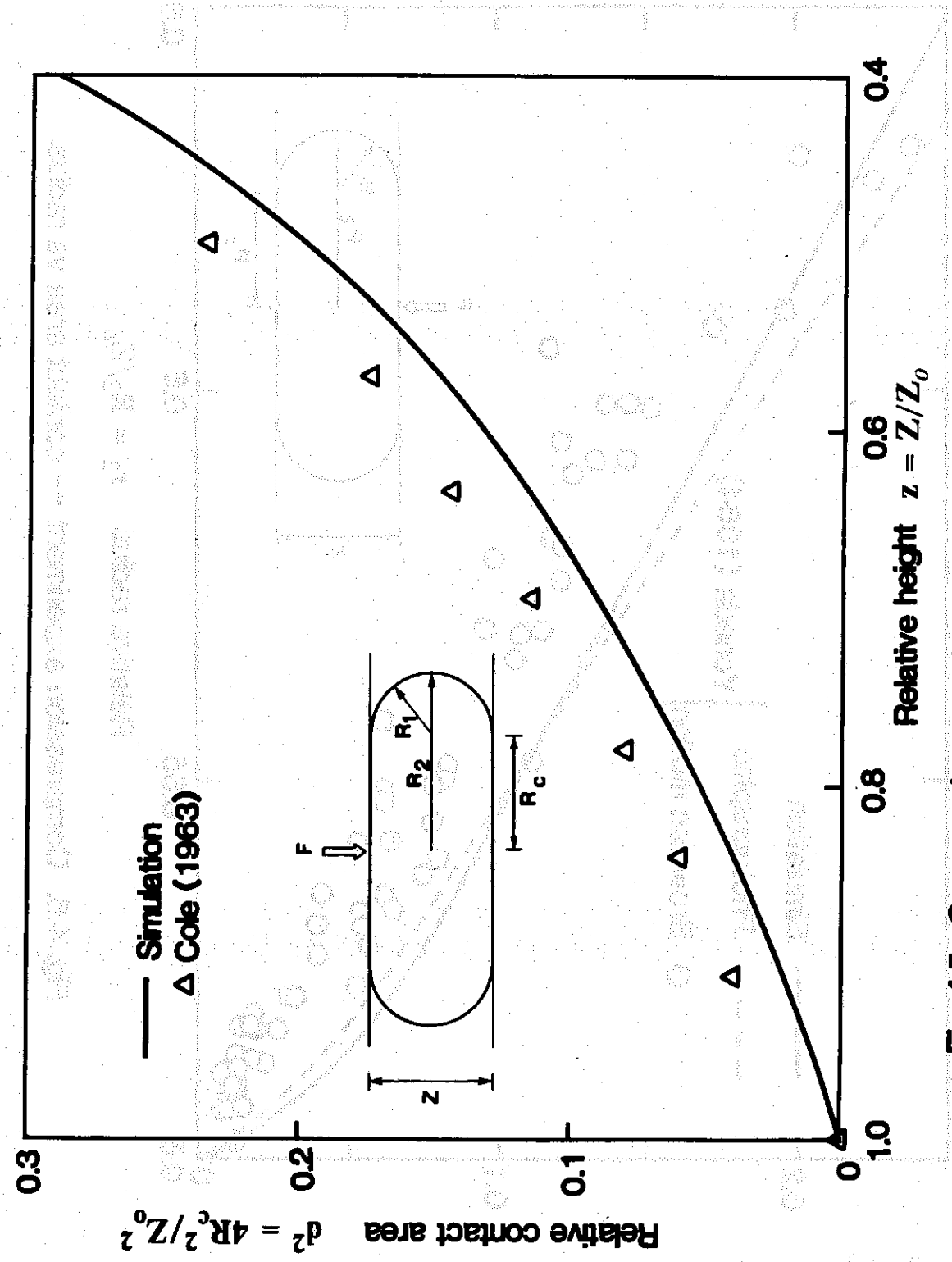

Fig. 4.5. Compression experiment — contact area vs height.

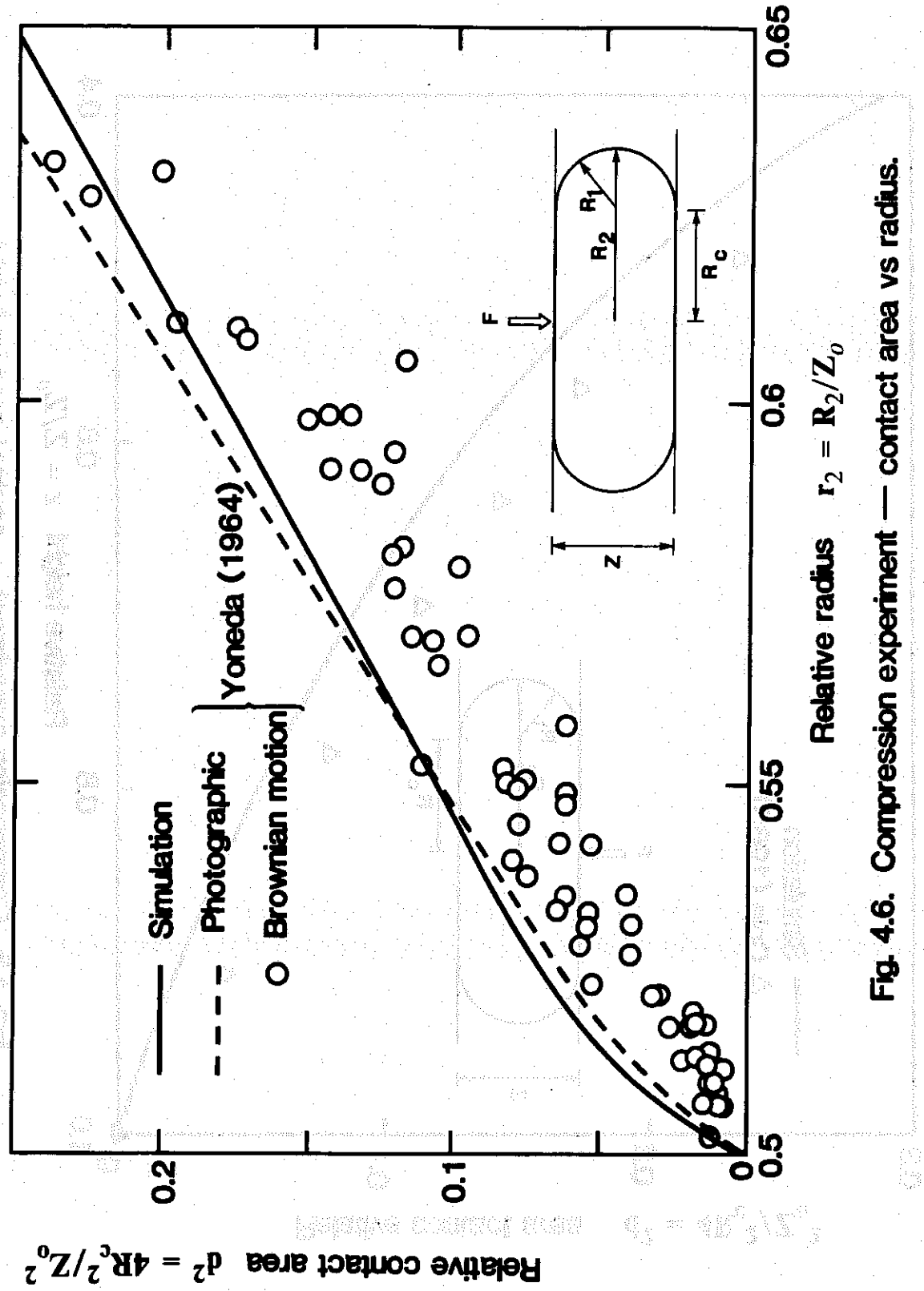

Fig. 4.6. Compression experiment — contact area vs radius.

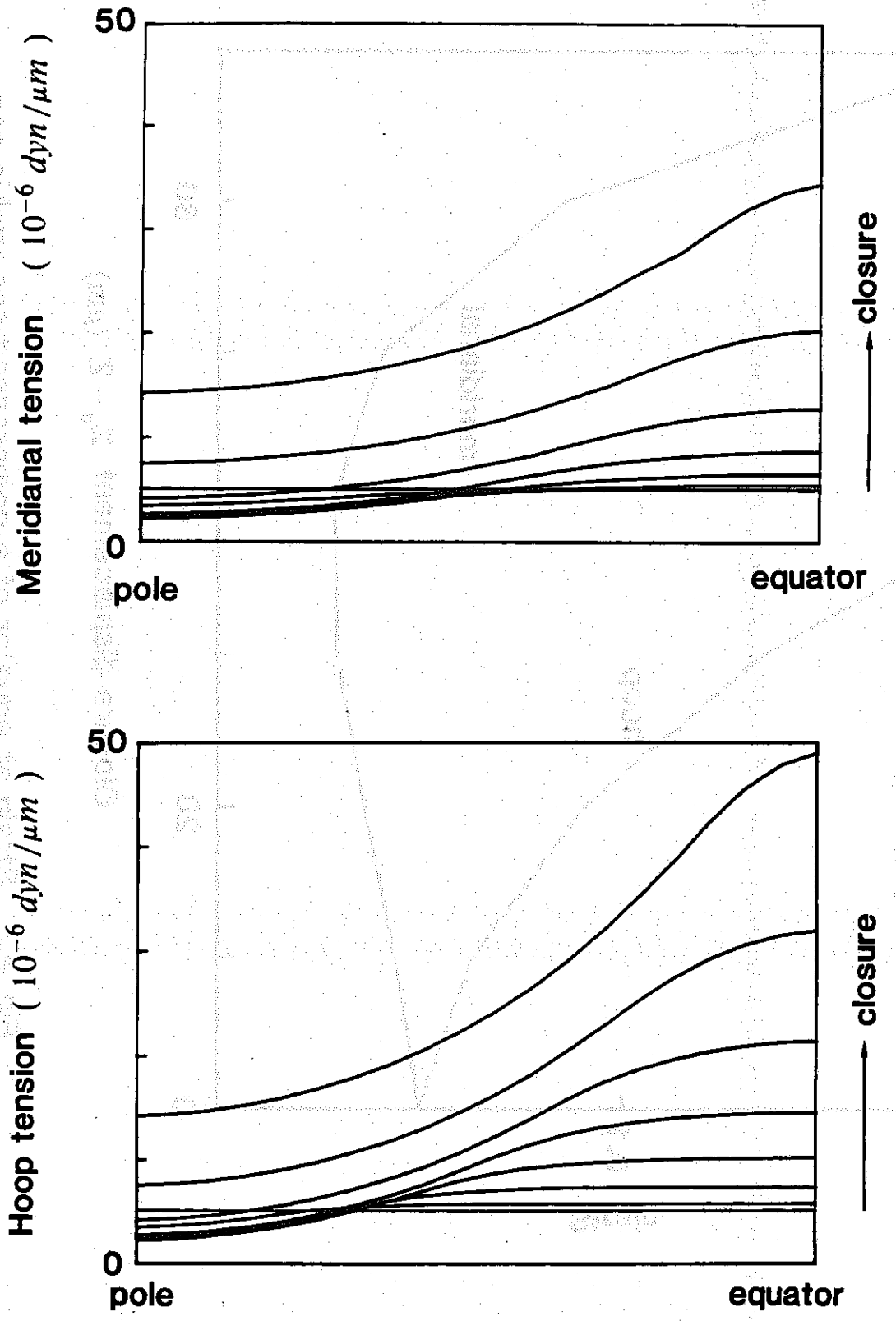

Fig. 4.7. Tension distributions on membrane of a compressed egg.

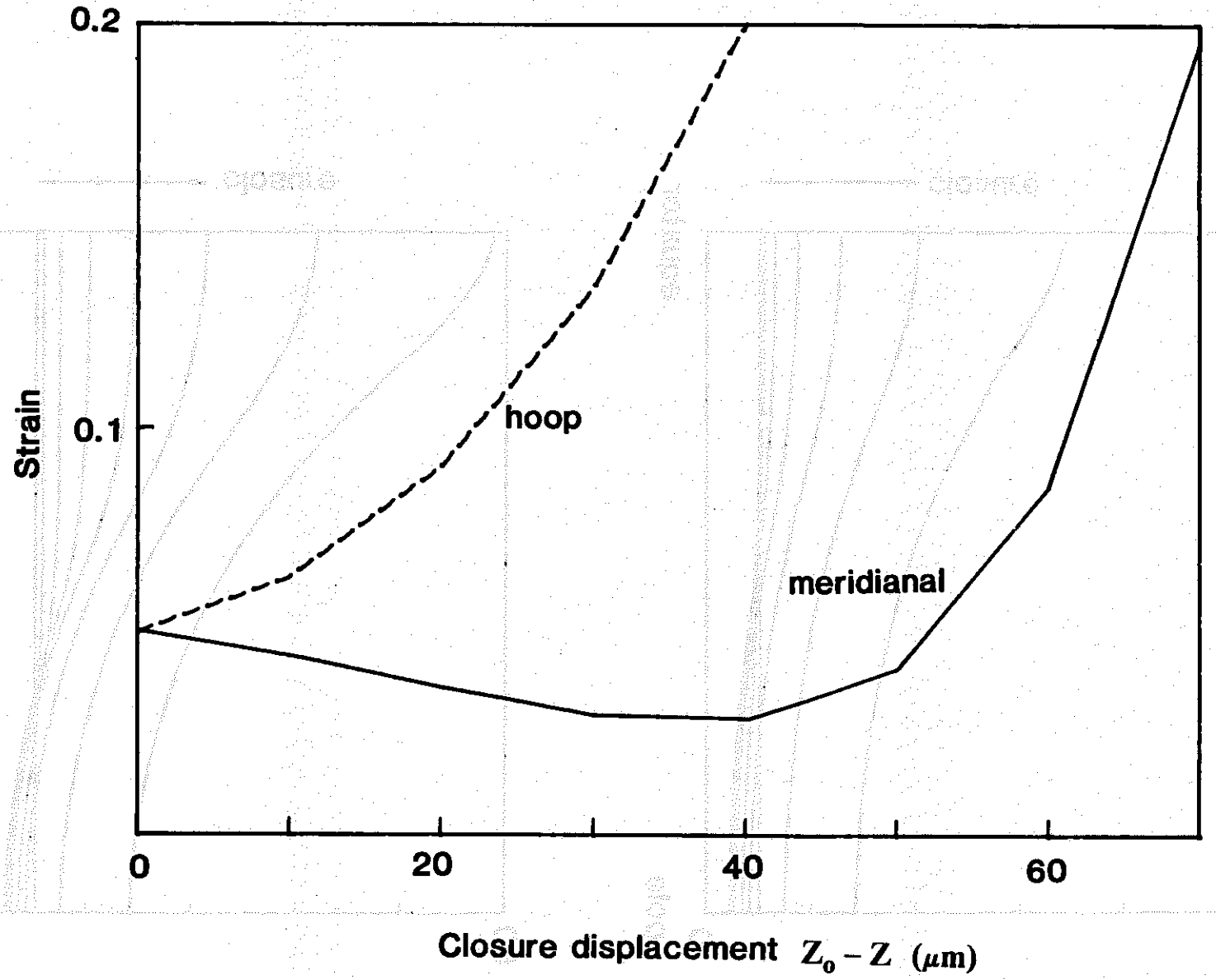

Fig. 4.8. Strain at equator of a compressed sea urchin egg

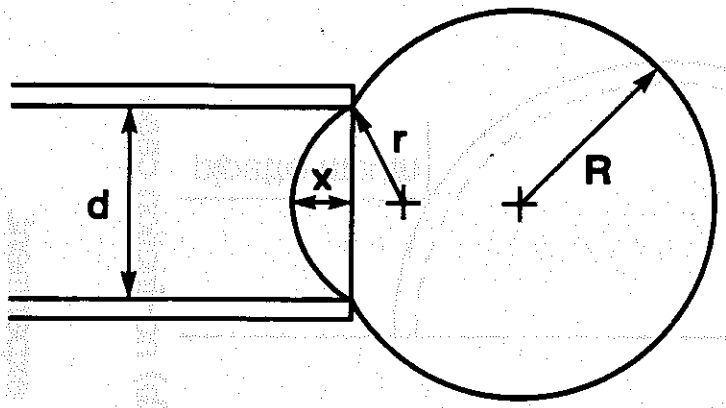

Fig. 4.9a. Deformation of an egg in the suction experiment.

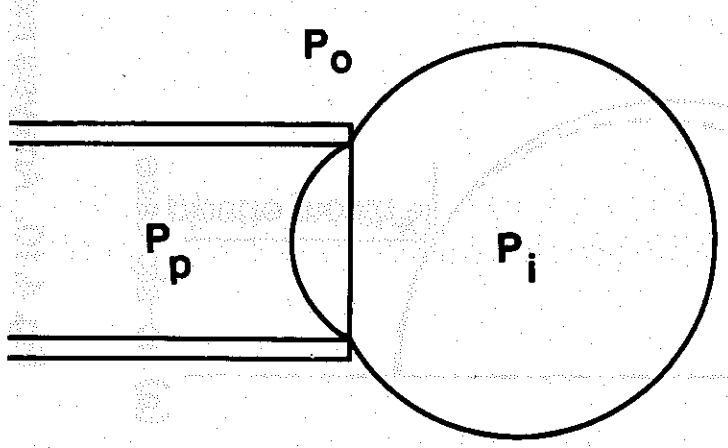

Fig. 4.9b. Fluid pressure acting at various locations.

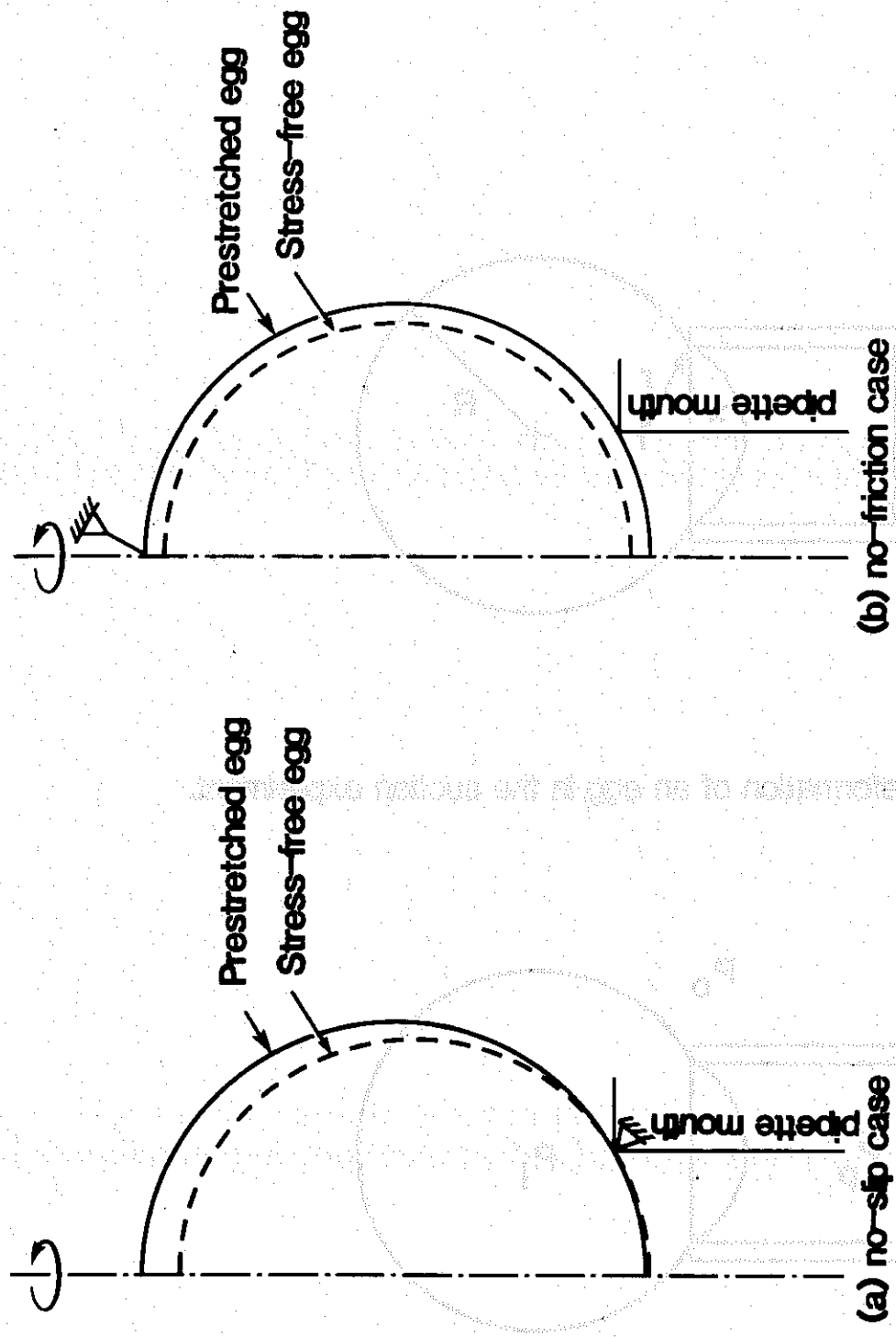

Fig. 4.10. Analysis models for the suction experiment.

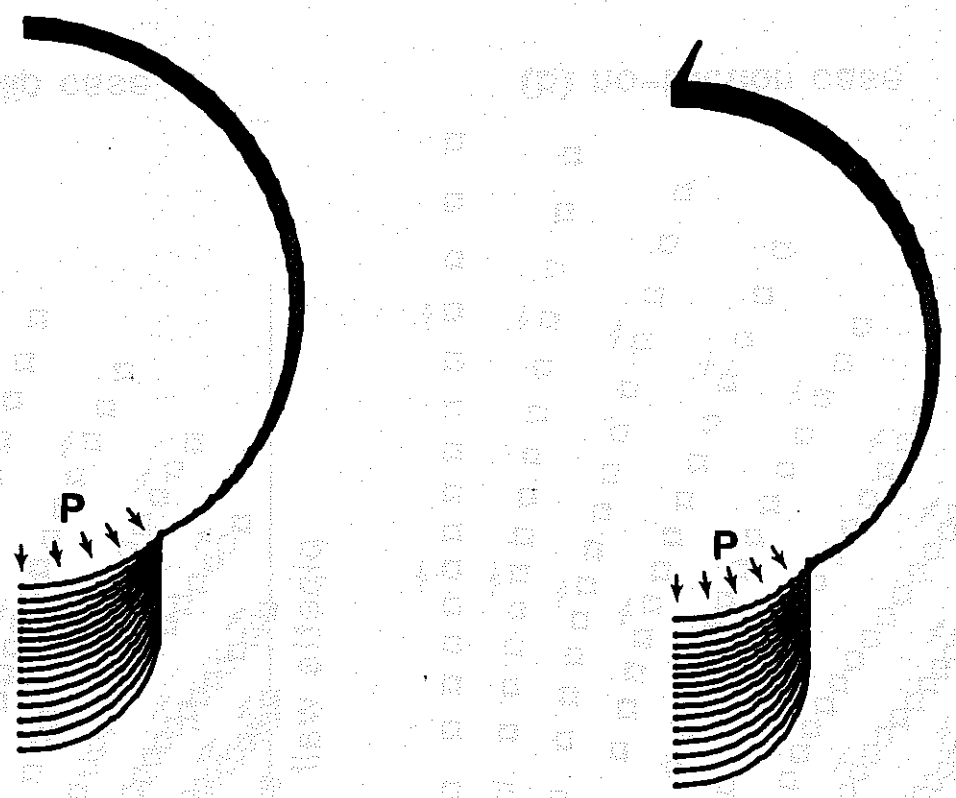

(a) no-slip case

(b) no-friction case

Fig. 4.11. Superimposed deformed shapes in suction experiment on sea urchin egg.

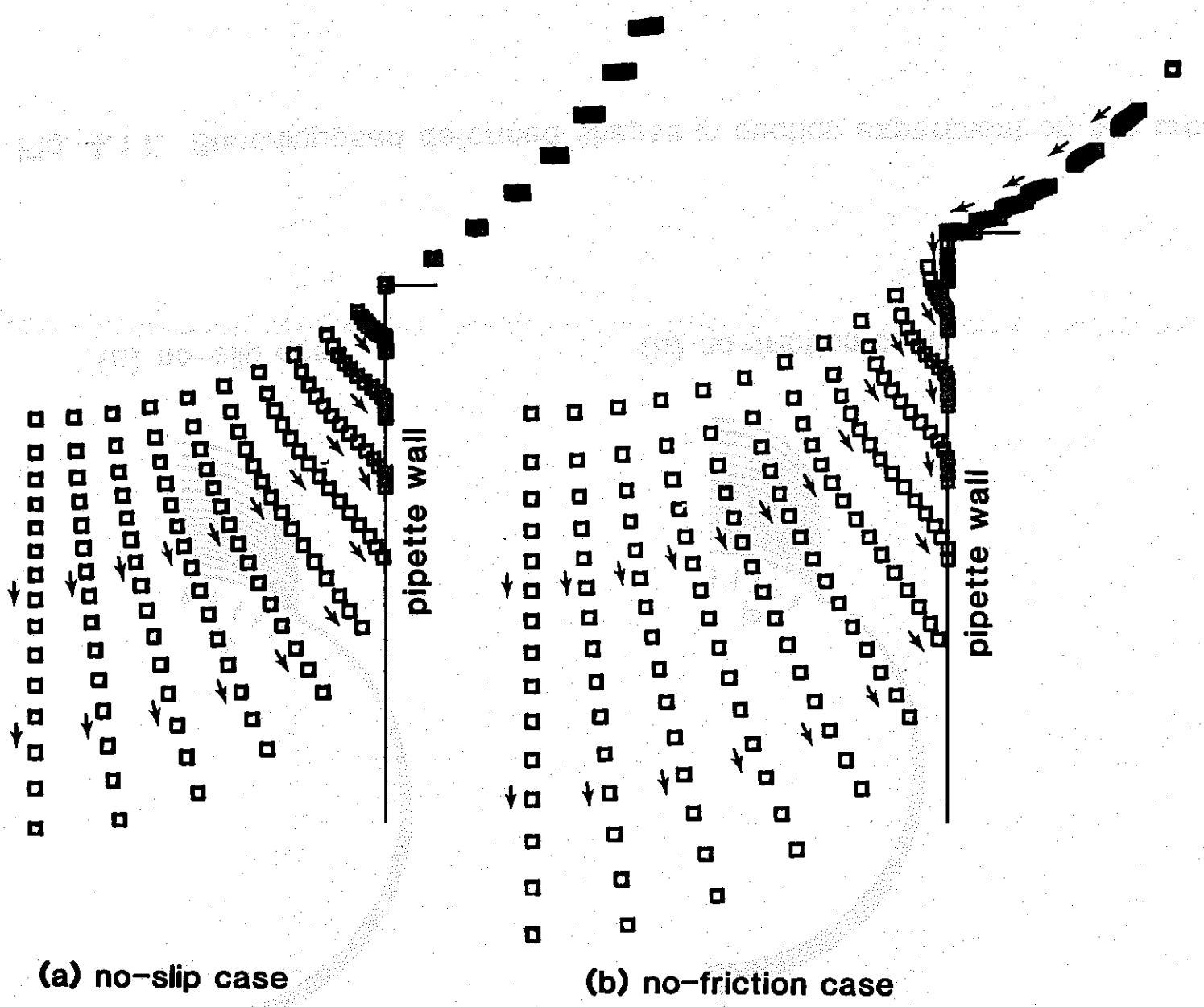

Fig. 4.12. Loci of points on membrane of a sea urchin egg in suction experiment.

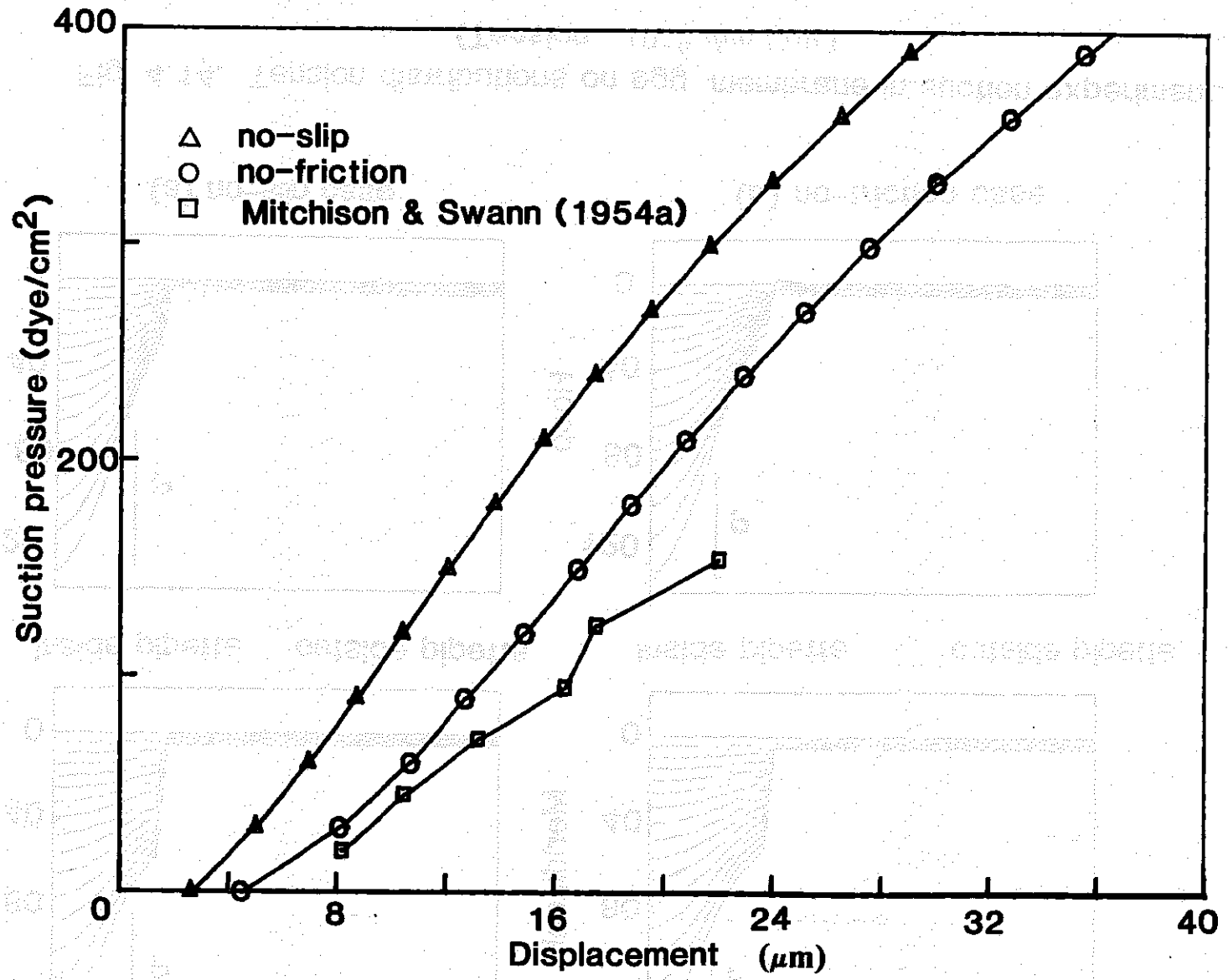

Fig. 4.13. Suction experiment -- suction pressure vs displacement into pipette mouth .

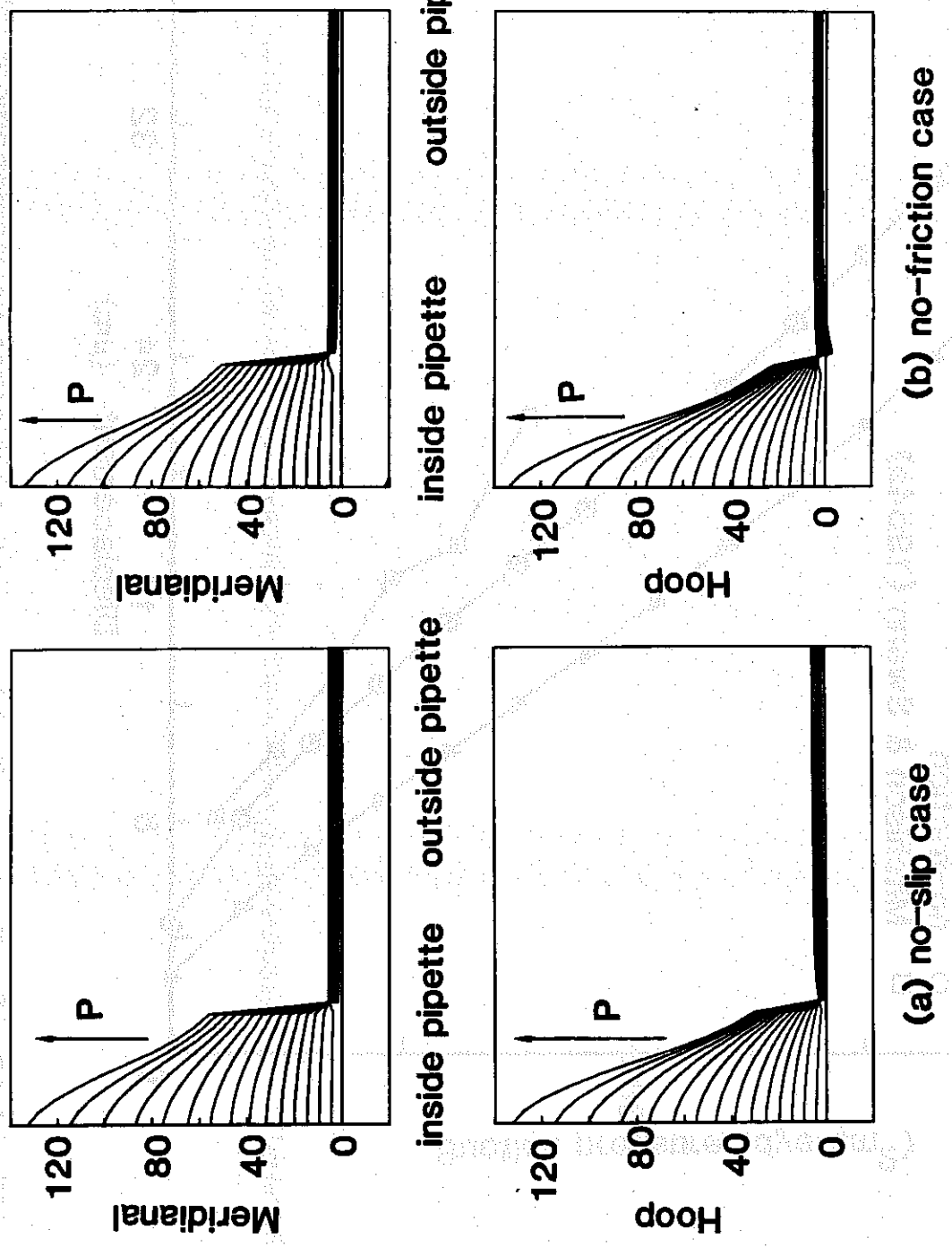

Fig. 4.14. Tension distributions on egg membrane in suction experiment. (Tension $10^{-6}\ dyn/\mu m$)

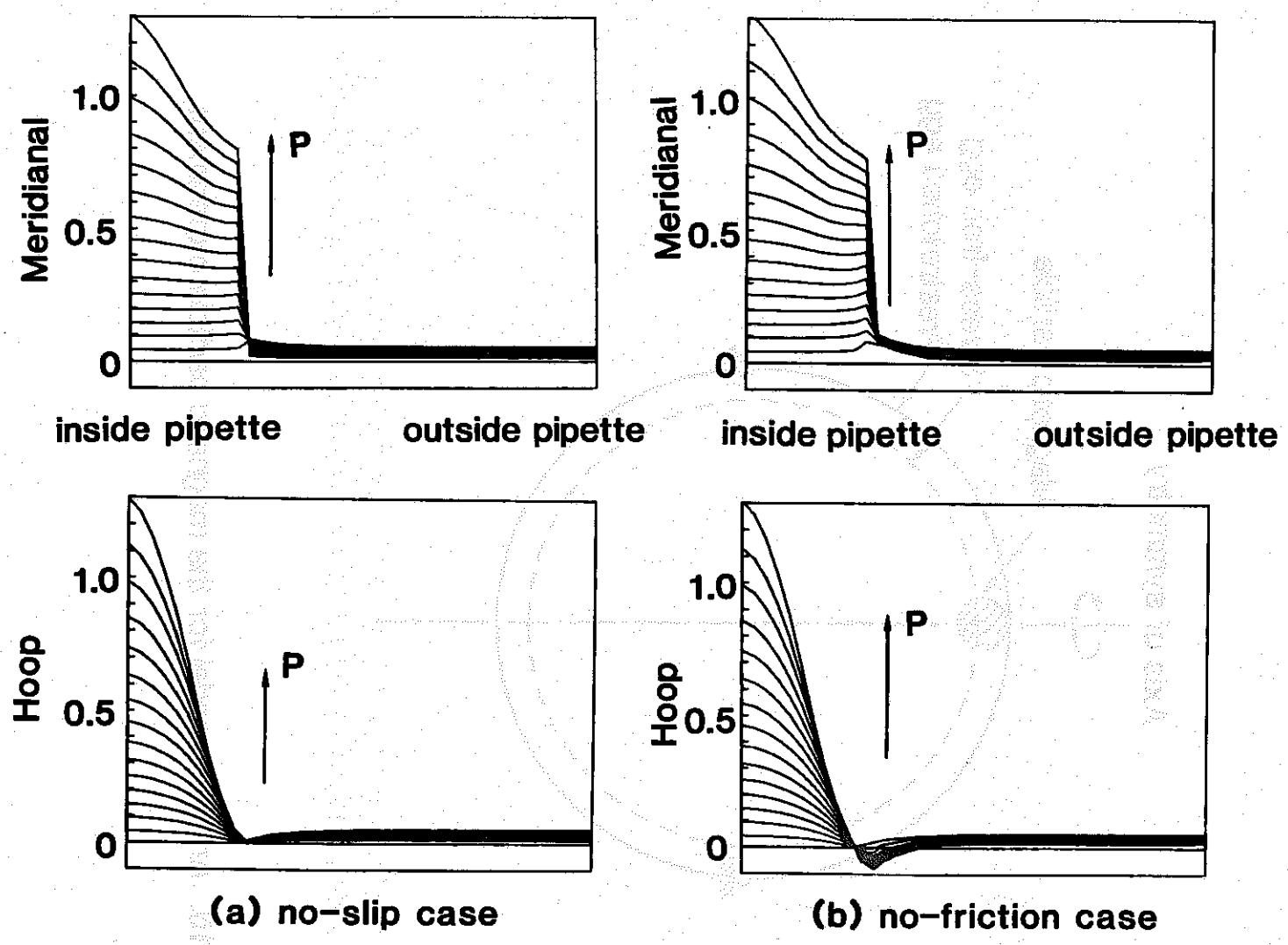

Fig. 4.15. Strain distributions on egg membrane in suction experiment.

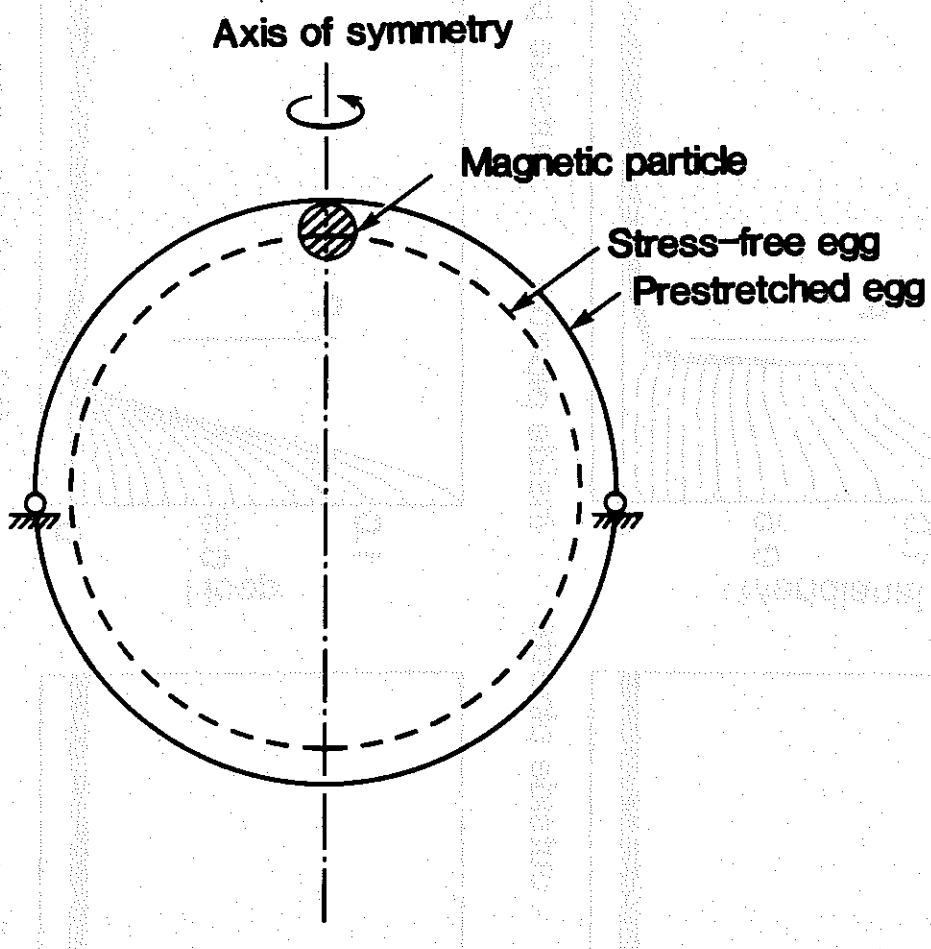

Fig. 4.16. Analysis model for the magnetic particle experiment.

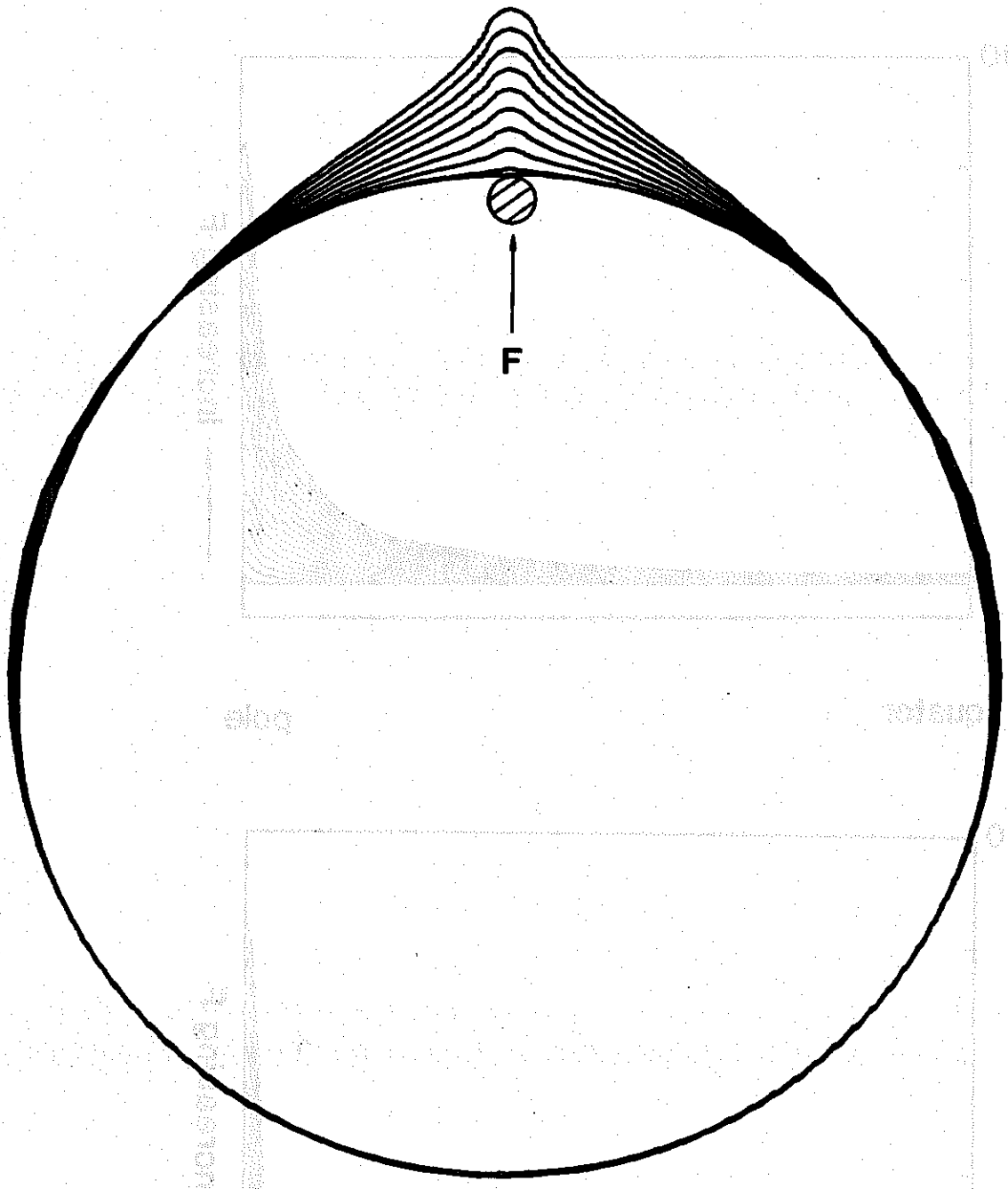

Fig. 4.17. Superimposed deformed shapes in magnetic particle experiment on sea urchin egg.

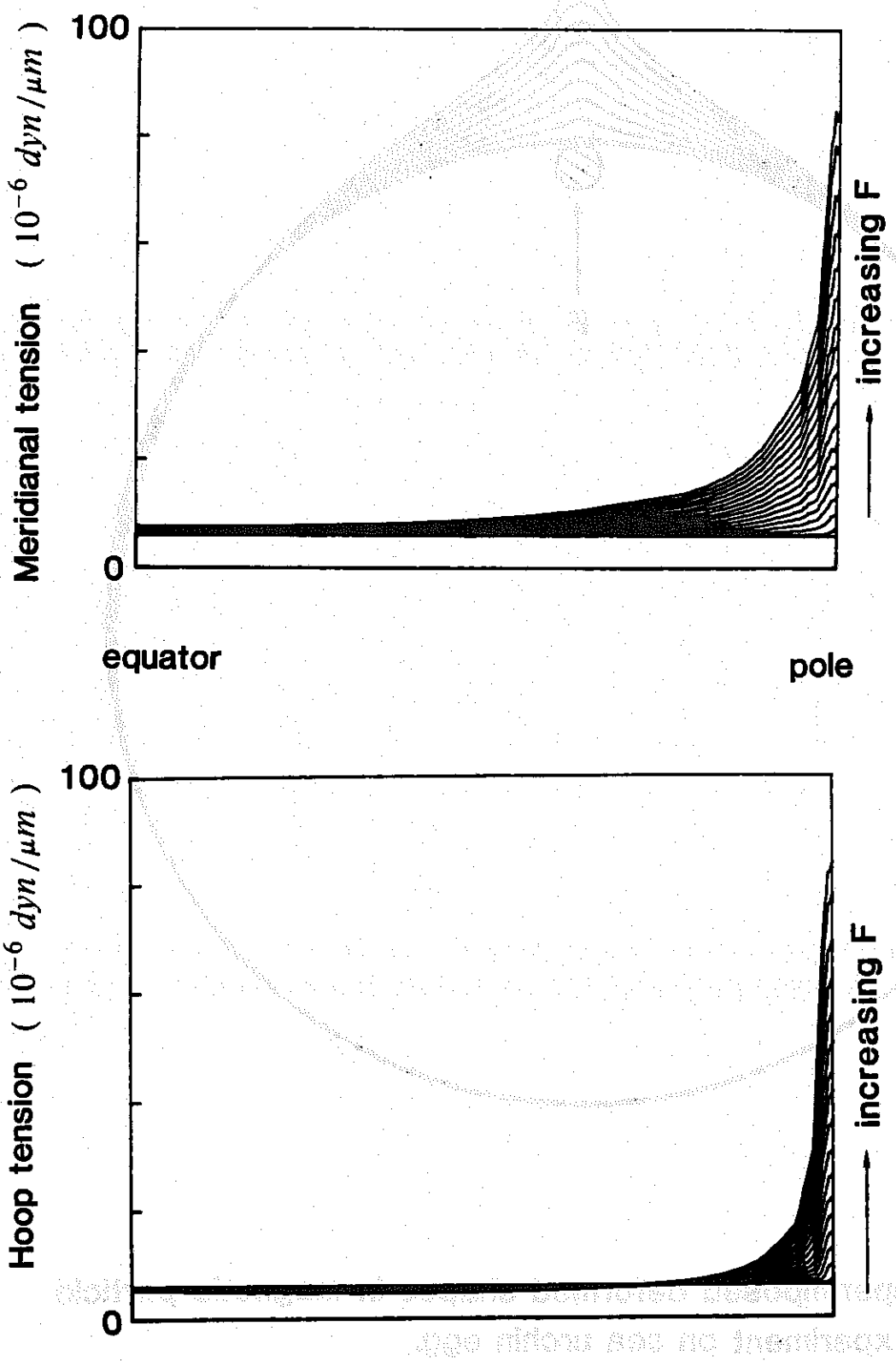

Fig. 4.18. Tension distributions on egg membrane in magnetic particle experiment.

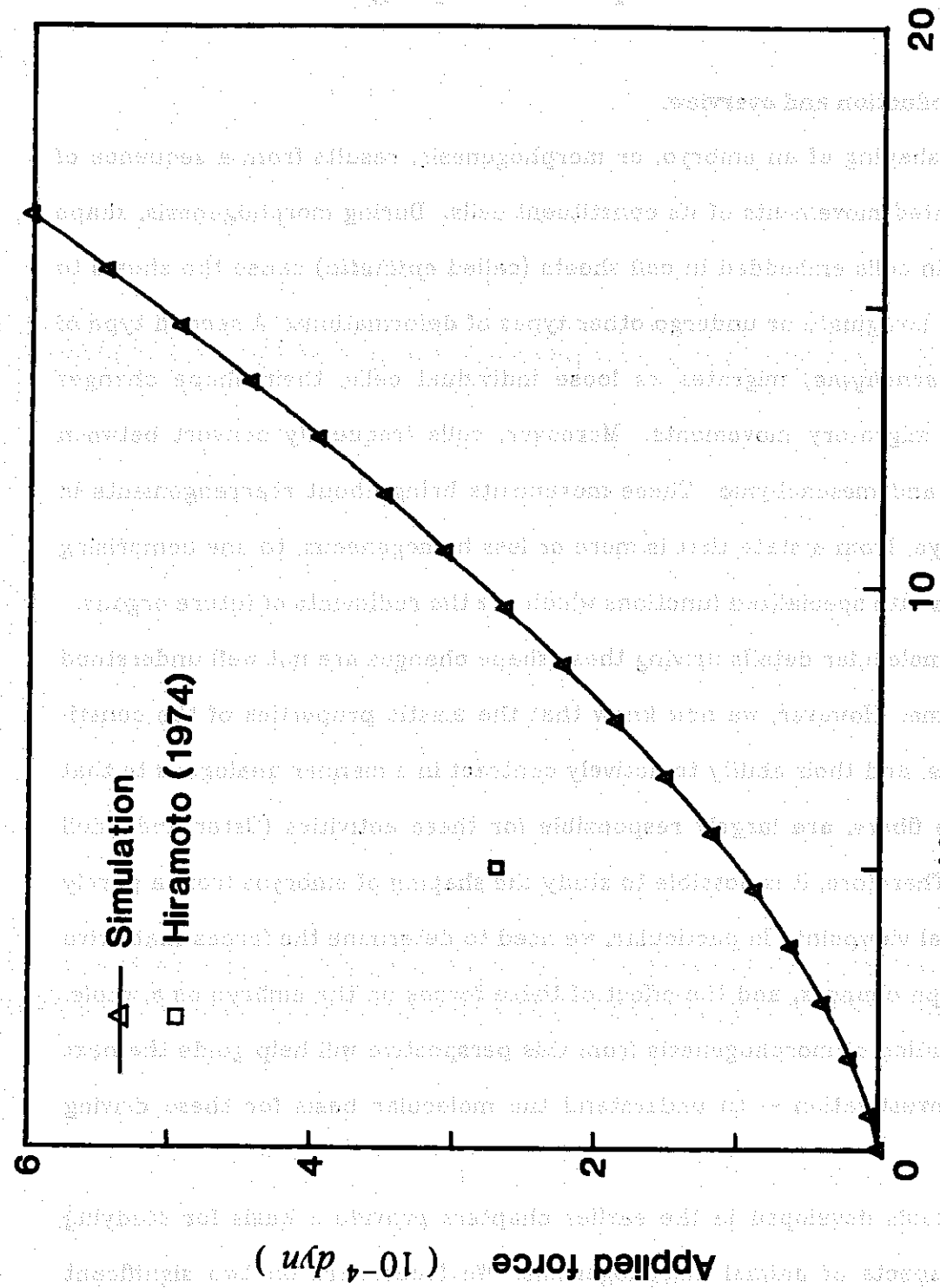

Fig. 4.19. Magnetic particle experiment -- force vs displacement.

Chapter 5

Mechanical Aspects of Morphogenesis

5.1. Introduction and overview.

The shaping of an embryo, or morphogenesis, results from a sequence of orchestrated movements of its constituent cells. During morphogenesis, shape changes in cells embedded in cell sheets (called *epithelia*) cause the sheets to roll, fold, invaginate or undergo other types of deformations. A second type of cells (*mesenchyme*) migrates as loose individual cells; their shape changes result in migratory movements. Moreover, cells frequently convert between epithelia and mesenchyme. These movements bring about rearrangements in the embryo, from a state that is more or less homogeneous, to one comprising cell layers with specialized functions which are the rudiments of future organs.

The molecular details driving these shape changes are not well understood at this time. However, we now know that the elastic properties of the constituent cells, and their ability to actively contract in a manner analogous to that of muscle fibers, are largely responsible for these activities (Oster and Odell [1984]). Therefore, it is possible to study the shaping of embryos from a purely mechanical viewpoint. In particular, we need to determine the forces that drive these shape changes, and the effect of these forces on the embryo as a whole. Understanding of morphogenesis from this perspective will help guide the next level of investigation -- to understand the molecular basis for these driving forces.

The tools developed in the earlier chapters provide a basis for studying various aspects of animal morphogenesis. We focus here on two significant developmental events -- gastrulation in sea urchins and neurulation in amphibia. In these studies, our emphasis is not on the molecular basis of the cell

shape changes, but on the mechanical consequences of the motion itself.

After fertilization, an egg undergoes a sequence of cell divisions, and is subdivided into a large number of cells (Stages 1-8, Fig. 5.1). These cells are arranged to form a cell sheet layer which encases a cavity in the center (Fig 5.2 for sea urchin embryo). During gastrulation, the basic body plan of the animal is established (Stages 9-14, Fig.5.1 for newt embryos, and Fig. 5.2 for sea urchin embryos). The reorganization and rearrangement of the cell sheet produce three cell layers. The outermost layer, the *ectoderm*, will eventually give rise to the nervous system and the *epidermis* -- the outermost body wall; the innermost layer, the *endoderm*, will become the gut and other internal organs related to the digestive tract; and the layer in between these two, the *mesoderm*, will form tissues such as the skeletal system, muscles and connective tissues. Following gastrulation, vertebrates undergo the process of neurulation, which establishes the spinal body axis. During this process, the dorsal side of the outermost cell layer rolls and elongates to form the rudiment of the future nervous system (Stages 15-20, Fig. 5.1).

5.2. Secondary invagination in sea urchin.

5.2.1. Introduction.

The sea urchin is a favorite organism to study gastrulation, because the movements involved are less complex than the analogous processes in other embryos. Furthermore, these embryos are easily obtained in large numbers, they develop rapidly and synchronously, and many species are transparent, allowing detailed observation of cellular movements during morphogenesis.

Gastrulation in sea urchin embryos occurs in two phases (Dan and Okazaki [1956], Gustafson and Kinnander [1956]). *Primary invagination* involves the

inward buckling of the embryo wall at its ***vegetal pole*** (see Fig. 5.2a,b), to form the gut rudiment, or ***archenteron***. As primary invagination proceeds, the gut rudiment, which is roughly cylindrical in shape, extends 1/4 to 1/2 of the way across the blastocoel (the large central cavity within the embryo); the length of the gut rudiment varies depending on the species. A slight pause marks the end of primary invagination, during which time the gut rudiment does not appreciably increase in length (Gustafson and Kinnander [1960]).

The onset of ***secondary invagination*** is marked by the appearance of long, narrow cytoplasmic filaments known as ***filopodia*** protruding from the ***secondary mesenchyme cells*** at the tip of the gut rudiment (Fig. 5.2c,d). The filopodia continuously probe the inner surface of the embryo wall as gastrulation continues; those which make stable contacts with cells in the opposite wall, the ***animal pole*** of the embryo, stick there and form "cones of attachment". Elongation of the gut rudiment also resumes at approximately this time, and continues until it reaches the opposite wall of the embryo (Fig. 5.2c,d). Where the gut rudiment makes contact, it fuses with the opposite wall of the embryo; this will be the site of the future mouth. The ***blastopore***, the external opening of the archenteron shown in Fig. 5.2, will become the anus of the future larva.

A number of workers have investigated the role of secondary mesenchyme cells during gastrulation in sea urchin embryos. Filopodial pulling by these mesenchymal cells has traditionally been regarded as the sole mechanism responsible for secondary invagination during sea urchin gastrulation. Studies have shown that treatments which normally disrupt filopodial formation and attachment indeed interfere with gastrulation of sea urchin embryos (Gustafson and Wolpert [1963], Dan and Okazaki [1956]). However, these treatments may have affected other processes which are important in secondary invagination. Furthermore, the phenomenon of ***exogastrulation***, the formation of an everted

gut (Dan and Okazaki [1956], Horstadius [1973]), suggests that the gut rudiment itself has some inherent capacity to elongate. To clarify the processes at work during secondary invagination, I have collaborated with an experimental biologist, Jeffrey Hardin, to investigate the cellular mechanisms and mechanics of gut rudiment elongation in two species of sea urchin, *Lytechinus pictus* and *Strongylocentrotus purpuratus*. Our studies (Hardin and Cheng [1986]) strongly suggest that, in addition to whatever tension is generated by contracting filopodia, active forces exist which cause cells within the gut rudiment itself to rearrange to form a longer, narrower tube.

5.2.2. Numerical simulations. Archenteron elongation during sea urchin gastrulation.

It is not known whether the forces responsible for the inward rolling of the vegetal plate during primary invagination continue to act during secondary invagination. If the embryo is made of elastic materials, then "unloading" these forces will cause the vegetal plate to unroll. The fact that this unrolling is not observed suggests that if the embryo is elastic this active force must persist throughout secondary invagination. On the other hand, the embryo may be composed of a viscoelastic material, whose memory of its strain history "fades" with time. In that case, "unloading" the active forces will not undo the deformation that has taken place, and the embryo remains in its newly deformed configuration. Since the mechanism causing primary invagination is not clearly understood, our simulations adopt the latter view. Accordingly, we treat the shape of the embryo after primary invagination as the initial stress-free configuration.

Figures 5.3a,b show tracings of embryos such as *L. pictus*, which are somewhat pear-shaped, have relatively thin walls, and which have relatively short gut

rudiments at the end of primary invagination. In contrast, Figures 5.3c,d show tracings of embryos such as *S. purpuratus*, which are more flattened, have somewhat thicker walls, and which have a relatively short distance to traverse during secondary invagination. Both models take into account the thicker wall at the animal pole of the embryo.

We use fifty axisymmetric shell elements to model the bending, shearing and stretching in the embryo wall. We assume the material of the wall to be elastic, (see Equation 2.8.4), and undergoes large deformation during gastrulation. We also maintain the fluid-filled volume bounded by the embryo wall, the ***blastocoel***, to be constant throughout the deformation history.

In order to simulate filopodia pulling on the ceiling of the embryo, we impose a uniformly distributed load acting over a spherical cap in that region, and directed towards the tip of the gut rudiment. Since the filopodia also pull the tip of the gut rudiment by equal and opposite forces, we model this by maintaining the tip of the gut rudiment stationary. Accordingly, the reactions induced by this kinematic constraint are the desired equal and opposite forces.

The first result of the simulations is that when the gut rudiment possesses the same mechanical properties as the rest of the embryo, denting of the roof of the embryo invariably results. Denting is especially pronounced in the case of *L. pictus* (Fig. 5.3a), but it also occurs in the case of *S. purpuratus*, although to a lesser extent (Fig. 5.3c). This result is consistent with the fact that the gut rudiment and the roof of the embryo, having roughly equal stiffness, are pulled by the filopodia with equal tensions. When the shapes of the actual embryos are compared with the predicted shapes, however, one sees that marked deflection of the embryo roof is never observed, at least in the two species we have studied. An occasional *S. purpuratus* embryo will exhibit a small degree of denting, but *L. pictus* embryos have never been observed to undergo this type of

deformation.

When the gut rudiment is made relatively more compliant than the rest of the embryo (fivefold or more), the embryo roof does not deflect (Fig. 5.3b,d). In this case, less tension is required to distend the gut rudiment, and the relatively stiff roof is able to withstand the traction exerted by the filopodia. Thus in order for the classical notion of filopodial traction to be consistent with the observed shape of the embryo, the wall of the gut rudiment must be much more compliant than the roof of the embryo.

However, even when the archenteron is assumed to be much more compliant than the rest of the embryo, two additional mechanical consequences of filopodial pulling are apparent. First, the blastopore (the external opening of the gut) does not constrict as the gut rudiment lengthens. *S. purpuratus* gastrulae do exhibit a relatively wide blastopore (Fig. 5.3d); however, the blastopore of *L. pictus* gastrulae show marked constriction (Figure 5.3b). Second, filopodial contraction results in a slight flattening of the embryo. Here again, embryos such as *S. purpuratus* do exhibit some flattening (Fig. 5.3d); in contrast, embryos such as *L. pictus* maintain their pear-shaped structure (Figure 5.3b).

5.2.3. Filopodial pulling is not the sole mechanism for archenteron elongation.

The question posed here is whether filopodial contraction itself is a *sufficient* mechanism responsible for elongating the gut rudiment. For a long time, the answer to this question has been yes. Our numerical and experimental studies (Hardin and Cheng [1986]), however, strongly suggest that it is in fact the combined effect of filopodial contraction and an additional active force system that drives secondary invagination.

The following observations have been made based on the mechanical simulations of filopodial pulling alone. First, denting of the embryo ceiling and flattening of the entire embryo will occur if the gut rudiment has the same mechanical properties as the rest of the embryo. Denting does occur in some species; in extreme cases some embryos take on an almost "biconcave" appearance (Okazaki [1956]). This extreme case may represent a significant contribution by filopodial pulling. If no denting is to occur, the gut rudiment must be very compliant in comparison with the rest of the embryo. Since it is not known whether such a difference in mechanical properties actually exists in these embryos, this case of no denting suggests that other mechanisms, besides filopodial pulling, may exist to help elongate the gut rudiment.

Second, filopodial pulling alone will produce a relatively wide blastopore. Indeed, the thicker-walled embryos we have examined tend to have wider blastopores (e.g. *S. purpuratus*). However, embryos such as *L. pictus* possess contricted blastopores which actually decrease in diameter as gastrulation proceeds. This again suggests the possibility that an additional mechanism may be at work. However, this additional mechanism may not necessarily be the same mechanism that helps the gut rudiment to elongate.

Our experimental findings (Hardin and Cheng [1986]) augment the above arguments. Based on tissue sections we found that the number of cells in the circumference of the gut rudiment decreases sharply during gastrulation. At the same time, the aspect ratio (the dimension along the longitudinal axis versus the dimension in the circumferential direction) of these cells in the gut rudiment remains constant while the gut rudiment lengthens. These two observations suggest that extensive cell rearrangements do occur in the gut rudiment during secondary invagination -- the cells in the wall of the gut rudiment repack preferentially along the longitudinal axis to form a longer tube with

smaller diameter.

It could be argued that the cell rearrangements observed here occur as a passive response to stretching, and not because the gut rudiment actively elongates. However, our experimental findings strongly suggest that the latter is indeed the case. In Hardin and Cheng [1986], we artificially induced exogastrulation in *L. pictus* via treatment with lithium chloride. When so treated, the evaginated gut rudiment lengthens following the first phase of evagination (Fig. 5.4a) in a manner resembling the normal process of secondary invagination (Fig. 5.2b). However, ***elongation occurs without filopodial pulling by secondary mesenchyme cells.*** Furthermore, secondary evagination seems to be accompanied by a decrease in the number of cells in the circumference of the gut rudiment, as in the normal case.

We conclude that, the combined effect of filopodial contraction and active cell rearrangements drives secondary invagination in the sea urchin. The relative contributions of the two processes seem to vary among different species, which could account for the wide range of morphologies observed amongst sea urchin embryos. Based on our findings, a greater contribution by filopodial contractions produces denting in the embryo ceiling while the gut rudiment elongates, whereas active cell rearrangements does not result in such denting. In both cases, filopodial contraction is important for the proper completion of gastrulation, both by stabilizing the lengthening gut rudiment, and subsequently guiding it to the site of the future mouth.

5.3. Neurulation in amphibia.

5.3.1. Introduction.

Neurulation in vertebrates is another example of cell sheet invaginations. Among vertebrates, amphibian neurulation is the simplest to study: their nervous system do not grow during that period of time, and some amphibia have large cells so that direct observation of cellular activities is possible. In the following, our study of neurulation will focus on the California newt *Taricha torosa* (Jacobson [1981]).

As gastrulation is completed, the embryo is reorganized into the three cell layers discussed above -- the endoderm, the mesoderm and the ectoderm. In newt, the ectoderm -- the outermost cell sheet -- comprises a single cell layer.

During neurulation, the hemisphere of ectoderm on the dorsal side of the embryo flattens to form the ***neural plate***. Underlying the neural plate along the midline is the ***notochord*** (Fig. 5.5). The portion of the plate directly above the notochord is referred to as the ***notoplate***. While the flattening takes place, the width of the neural plate decreases, and cells in the neural plate change shape from cuboidal to columnar (stage 17 in Fig. 5.5). The plate then elongates along the midline and cells in the notoplate undergoes systematic neighbor changes. As a result of these movements, the disc-shaped plate distorts into a key-hole shape (Fig. 5.6). Finally, while the elongation persists, the neural plate rolls into a tube (Fig. 5.6 and stages 17-21 in Fig. 5.5). This closed tube is the rudiment of the central nervous system, from which the brain and the spinal cord will form.

It is not easy to ascertain the underlying mechanisms driving the various movements that take place during neurulation. A number of workers have proposed models to explain how cell sheets invaginate (Ettensohn [1985]). Among various proposals, the ***apical constriction*** hypothesis of Burnside [1971,1973]

appears to be most favored. Ultrastructural studies have shown that microfilaments are circumferentially organized near the apical surface of neural plate cells (Fig. 5.7). The possible constriction of these microfilaments induces cells to become taller and at the same time expand basally. The basal expansion produces a bending moment that rolls the neural plate into a tube.

Recently, Jacobson, Odell and Oster [1985] presented the *cortical tractor* model for driving the movements of cell sheets. They view a cell sheet as a dynamic structure: each cell cortex, driven by its contractile machinery, cycles its cytoplasm in a flow pattern whose time average is shown in Fig. 5.8. Membrane and adhesive structures are inserted in the basal and lateral surfaces, flow apicalward, and are recycled to the cell interior in the apical region. Junctional structures pile up at the apical circumference and maintain the seal which isolates the embryo from the external chemical environment. The cortical tractor model further attributes morphogenesis of an epithelium to the difference in tractor intensity amongst cells within a cell sheet, which may be stimulated by local ionic conditions. According to this model, cells can "tractor" within the plane of the cell sheet, thereby changing their neighbor relationships, without violating the integrity of the apical seal. Furthermore, cell tractoring in the direction normal to the sheet surface can cause cell shapes to change from cuboidal to columnar. These two motile activities are indeed observed in neural plate cells during neurulation. The cortical tractor model further suggests that neural plate cells, tractoring faster than the neighboring epidermal cells (see Fig. 5.9), will crawl beneath the epidermis. This active cell crawling is believed to cause the neural plate/epidermis boundary to elongate, and meanwhile produce a bending moment to roll the plate into a tube (see Fig. 5.9).

The cortical tractor and the apical constriction models provide a number of possible mechanisms for the various cellular events during neurulation. We shall perform numerical simulations to assess the relative importance of several of these mechanisms. Based on these results, and on results by other workers, we shall try and deduce how the various processes contribute and fit together during neurulation.

5.3.2. Neurulation in amphibia. Numerical simulations.

We study here several possible mechanisms of neural plate deformation separately in order to assess their relative contributions to the observed morphological changes. Our focus is on the three principal cell movements that drive the process of neurulation:

1. columnarization of cuboidal cells (i.e. increase in the cell height/cross sectional area ratio) to form the initial neural plate.
2. elongation of the neural plate associated with active cell repacking (i.e. neighbor exchange).
3. apical constriction and basal expansion of plate cells which roll the plate into a tube.

5.3.2.1. Columnarization.

Odell *et al* [1981] simulated the neural plate by a finite element plane stress truss model that involved only bending moments generated by apical constriction. They found that, regardless of how the contraction initiated (e.g. at the center, or at the plate edges) the first event was the columnarization of the active cells and the flattening of the active cell population into a plate. I have collaborated with these workers in constructing a model for epithelial deformation driven by the cortical tractor mechanism. Our study, as described

below, shows that cell tractoring can also produce columnarization of the neural plate (Cheng, Murray, Odell and Oster [1986]).

First, we consider two adjacent cells of the neural plate by trapezoidal elements, whose vertices are denoted by $(i-1,i,i+1)$, and refer to the cell with boundaries $i,i+1$ as cell i (see Fig. 5.10). We shall employ the following notation:

- H_i = the height at node i (i.e. the boundary between cell i and cell $i-1$).
- H_0 = the initial (unstressed) height of each cell.
- W_i = the width of cell i.
- W_0 = the initial (unstressed) width of each cell.
- v_i = the velocity of the cortical flow in cell i.
- k = the passive extensional modulus of each cell.
- G = the passive shear modulus of each cell.
- α = the active shear modulus for each cell due to tractor motion.

The equations of motion of cell i are derived by writing down balance equations on node i for the vertical force components. Since the inertial force acting on embryos of this scale is negligible (Odell *et al* [1981]), the force balance equation for node i at steady state is

$$k\left[\left(\frac{H_i+H_{i+1}}{2}-H_0\right)\frac{W_i}{2}+\left(\frac{H_{i-1}+H_i}{2}-H_0\right)\frac{W_{i-1}}{2}\right]+G\left[\left(\frac{H_i-H_{i-1}}{2}\right)+\left(\frac{H_i-H_{i+1}}{2}\right)\right] \quad (5.1)$$

$$=\alpha\left|(v_i-v_{i-1})H_i\right|$$

The terms on the left hand side above are the passive resisting forces to extension at node i and to shearing by the cells on both sides of node i, respectively. The right hand side gives the active shear forces generated by the tractoring motion. Here, the absolute value is present since any relative velocity change will generate an active shearing force. The active shear modulus per unit height

is α, and so must be multiplied by the cell height, H_i.

We also impose an incompressibility constraint on each cell:

$$(\frac{H_i + H_{i+1}}{2}) W_i = H_0 W_0 \qquad (5.2)$$

Thus it is possible to express the equilibrium equations (5.1) in terms of H_i only.

The simulation of (5.1) and (5.2) is straightforward. The equations lead to a stiffness matrix that is symmetric and tridiagonal, which can be solved by standard equation solving packages. Two results are shown in Fig. 5.11, which illustrate some counterintuitive properties of the cortical tractor model. The tractor velocity is a monotone function of local chemical conditions, and so the variation in the tractor velocity field can be taken as reflecting the spatial chemical concentration distribution. In Fig. 5.11a, a uniform gradient in tractor velocity, v, produces a placode of constant height: i.e. a constant displacement field. In Fig. 5.11b, a periodic tractor velocity field, $v(x)$, produces a displacement field which is shifted with respect to the velocity field. Thus the morphogenetic movements generated by the cortical tractor do not correspond simply to the pattern of chemical concentrations, but to the *gradients* in concentrations.

This model demonstrates that cell tractoring can also produce columnarization of the plate. Therefore, on the basis of this model, and that of Odell *et al* [1981], it is only possible to assert that either, or both, mechanisms -- acting simultaneously and uniformly over the presumptive plate -- can produce the initially flattened neural plate.

5.3.2.2. Rolling.

The combined effects of apical constriction (via apical filament constriction and/or tractoring) and cell crawling is to produce a rolling moment. Elongation of the notochord can also induce a rolling moment by generating a transverse compression ("Poisson buckling"). We first study the pure rolling problem employing the axisymmetric shell elements developed in Chapter 2. The elongation problem will be studied next.

We model the embryo as a torus, with a very large major radius (see Fig. 5.12). By this approach, the embryo is effectively modeled as a cylinder. We choose the thickness/radius-of-curvature ratio to be 1/10 for the epidermal cell layer, and twice that for the neural plate. These represent the approximate size proportions at the time of tube formation. We employ forty shell elements to represent the cross-section of the embryo, and assume the volume within the embryo wall to remain constant while the embryo is deformed.

The effects of apical constriction and cell crawling is to produce an *active* rolling moment acting on the neural plate. This active moment can simply be incorporated in the constitutive relation in (2.8.4):

$$\mathbf{S} = \mathbf{D}\mathbf{E} + \mathbf{S}_{active} \tag{5.3}$$

where $\mathbf{S}$ is the stress resultant vector, $\mathbf{E}$ is the strain vector, and $\mathbf{D}$ is the constitutive matrix (see Box 2.9.1). In this case, $\mathbf{S}_{active}$ takes the form:

$$\mathbf{S}_{active} = [0\ 0\ M_{active}\ 0\ 0]^T, \tag{5.4}$$

where M_{active} is a loading function to be prescribed spatially and temporally.

Although the effects of apical constriction and cell crawling both create an active rolling moment, there are differences between these two mechanisms. Cell crawling initiates near the plate margin (see Fig. 5.9), and progresses towards the midline of the plate. It is not clear whether apical constriction

follows this pattern of activity, or simply acts over the entire neural plate simultaneously. We shall study both of these cases in the following, via the prescription of M_{active} in (5.4).

The results of our simulations, as shown in Fig. 5.13, are essentially the same as the predictions based on the plane stress model of Odell *et al* [1981]: bending moments generated either by apical constriction or by tractoring can roll the neural tube.

Fig. 5.13a shows the results of applying a uniform rolling moment across the neural plate, due to tractoring and/or apical constriction. The sequence of deformed configurations for increasing magnitudes of the applied moment are shown superimposed. These results are qualitatively similar to those of Odell *et al* [1981], who demonstrated that the rolling moment alone is capable of deforming the neural plate in the proper sequence of shapes: first a flat plate forms, which then rolls into a tube. The simulations in Fig. 5.13 also show several other interesting features of neurulation. First, the formation of the plate, and the subsequent rolling of the neural tube, are much more realistically mimicked by the simulations if the notochord is fixed (Fig. 5.13b). This suggests a role for the notochord during neurulation quite different than has heretofore been proposed: as a structural reinforcement supporting the neural plate. Second, the intermediate shapes of the neural tube during rolling are much more realistically reproduced if the rolling commences at the plate edge and proceeds inward towards the centerline (Fig. 5.13c). This, coupled with the hypothesis that crawling of plate cells on the epithelium generate the rolling moment, leads us to conclude that the rolling moment generated by the plate edge, rather than beginning at the centerline, as simulated by Odell *et al* [1981].

5.3.2.3. Elongation.

In order to investigate the role of midline and/or marginal elongation a full three dimensional model is required. We employ for this a general purpose finite element program called ABAQUS (Hibbitt, Karlsson and Sorensen [1982]). The neural plate is modeled as flat plate, as shown in Fig. 5.14. We apply a tangential force to the plate along the midline to produce the elongation, and impose a uniformly distributed vertical pressure, which produces a small perturbation to initiate the buckling instability.

Fig. 5.14 shows the results for plate with thickness/length ratios of around 1/20 and 1/200. These results demonstrates that pure elongation of the neural plate boundary cannot reproduce the proper shape of the neural fold, and cannot roll the plate into a tube unless the plate is unrealistically thin. However, in conjunction with the rolling moment, elongation contributes somewhat to the proper shaping of the neural folds.

5.3.3. The sequence of events during neurulation.

We have concluded from the simulations that the sequence that best reproduces the observed changes is as follows. First, the plate forms by movements that are uniform over the entire neural plate. These movements produce columnarization of the initially cuboidal plate cells, and can be generated by apical constriction, tractoring, or a combination of the two. Concurrently, elongation of the neural plate occurs both at the centerline and at the plate edges. The elongation is driven by the active interdigitation of notoplate cells at the centerline, and the crawling and interdigitation of plate cells at the neural plate/epidermis boundary. This elongation is not sufficient by itself to generate much of a rolling moment because of the thickness of the plate; however, it does appear to contribute somewhat to the rolling forces.

Subsequently, rolling of the neural tube commences at the plate boundaries, and proceeds inward (rather than from the center outward, as suggested by the simulations of Odell *et al* [1981]). As we mentioned above, the rolling moment can be generated by apical constriction or tractoring alone, or in combination. However, the configuration of cells shown in Fig. 5.9 gives strong support to the supposition that crawling of the marginal cells on the epidermis is a strong component of the rolling moment.

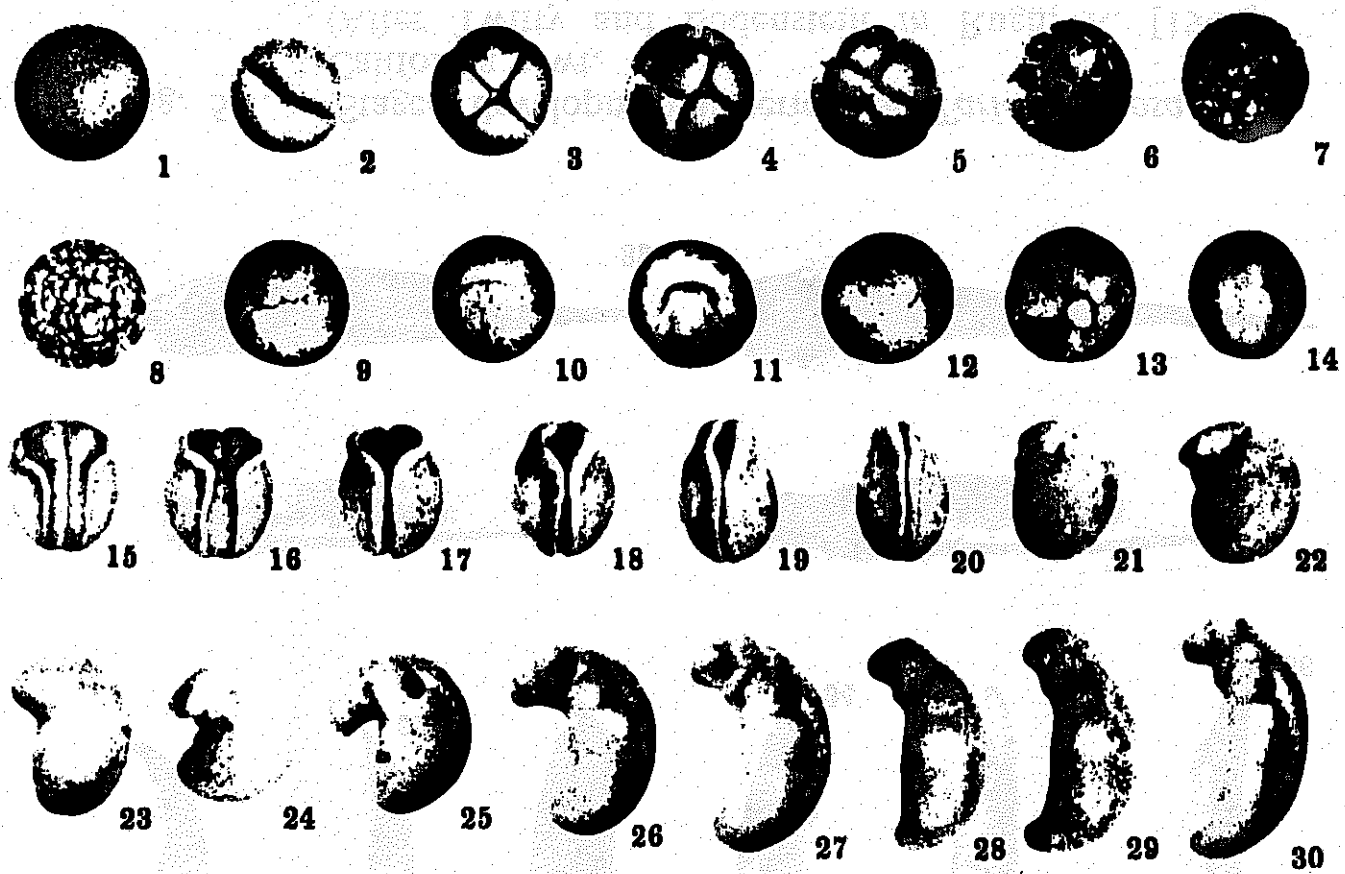

Fig. 5.1. (Continued on the next page).

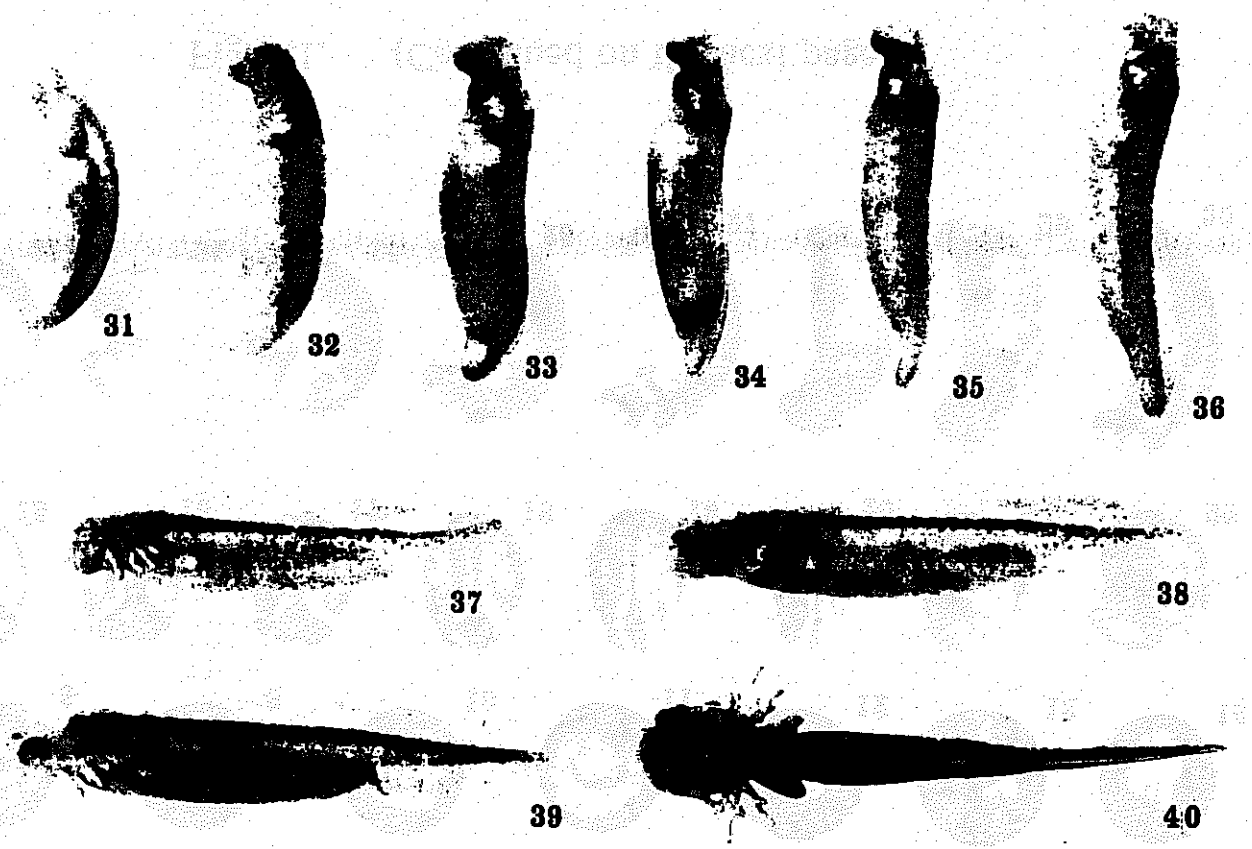

Fig. 5.1. Staged developmental series for *Taricha torosa*, the California newt.
(After Twitty and Bodenstein *in* Rugh, R. [1948]. *Experimental Embryology*, p.101, Minneapolis: Burgess Publishing Co.)

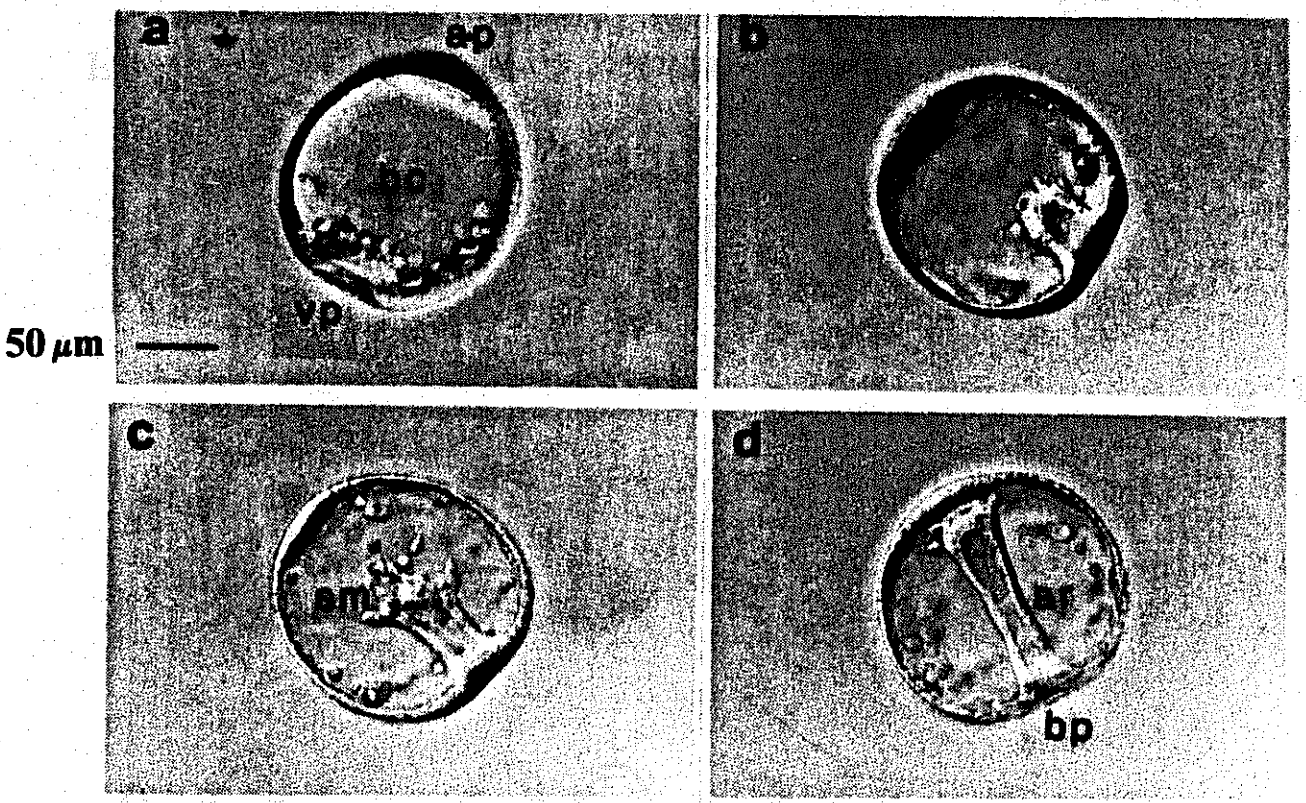

Fig. 5.2. Normal gastrulation in *Lytechinus pictus*. (a) Early gastrula, (b) onset of secondary invagination, (c) continuation of secondary gastrulation, (d) gastrulation completed. (ar) archenteron, (ap) animal pole, (vp) vegetal pole, (bc) blastocoel, (sm) secondary mesenchyme, (bp) blastopore. (From Hardin and Cheng [1986]).

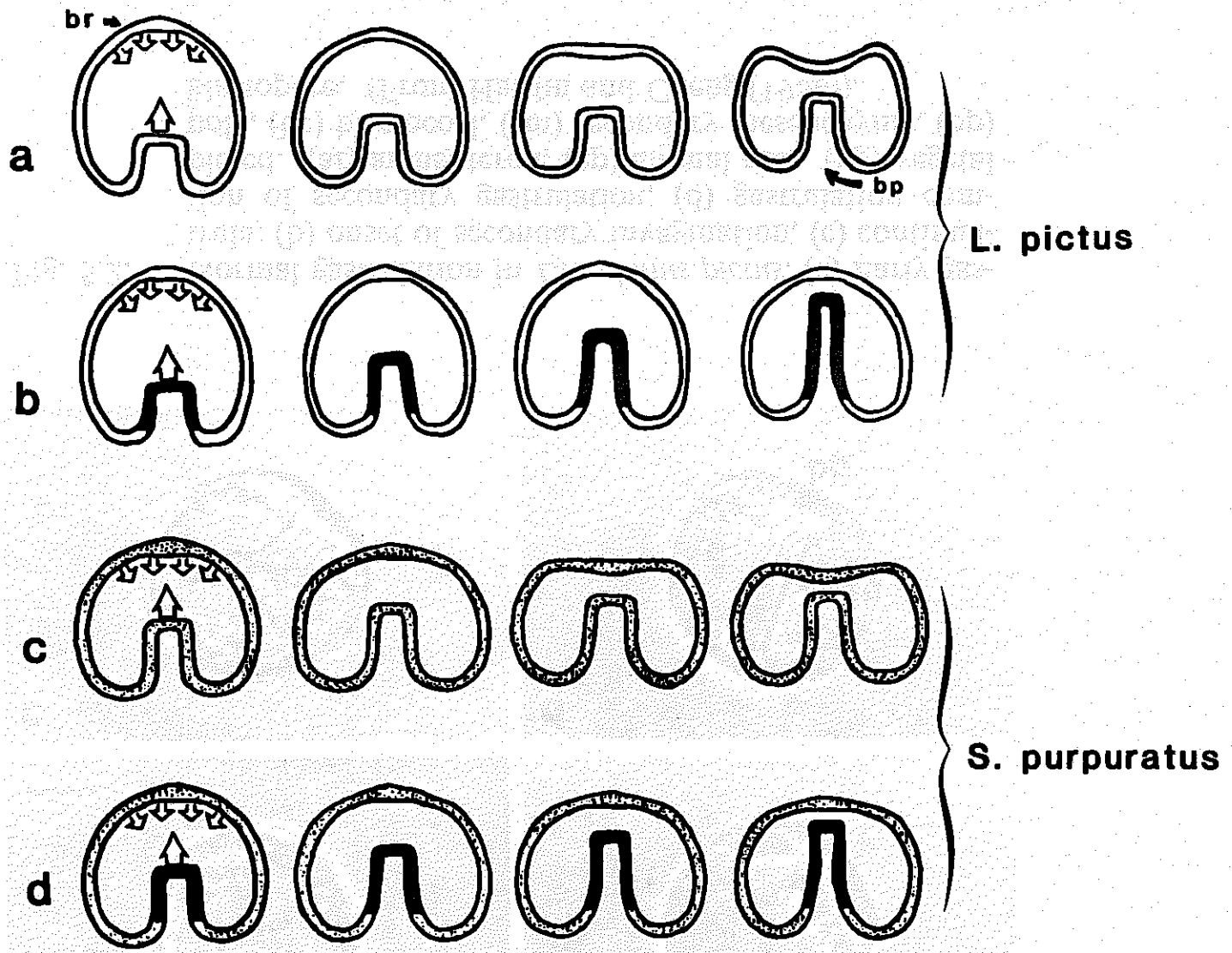

Fig. 5.3. Simulations of secondary invagination in sea urchin embryos. Shaded archenteron is more compliant than the rest of the embryo. (br) blastocoel roof, (bp) blastopore. (From Hardin and Cheng [1986]).

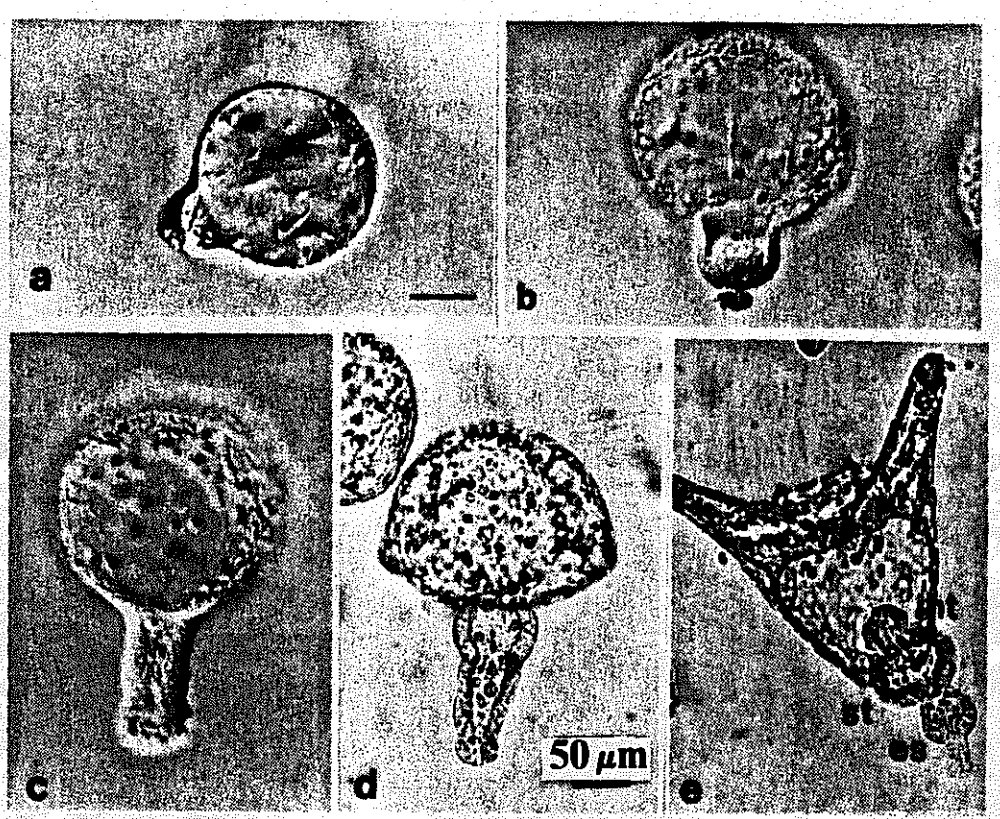

Fig. 5.4. LiCl-induced exogastrulation in *L. pictus*. (a) Early exogastrula, (b) onset of secondary evagination, (c) mid-/late exogastrula, (d) prism-stage exogastrula, (e) pluteus-stage exogastrula. Note the normal development of skeletal spicules (sp), and the tripartite differentiation of the gut into esophagus (es), stomach (st), and intestine (int). (From Hardin and Cheng [1986]).

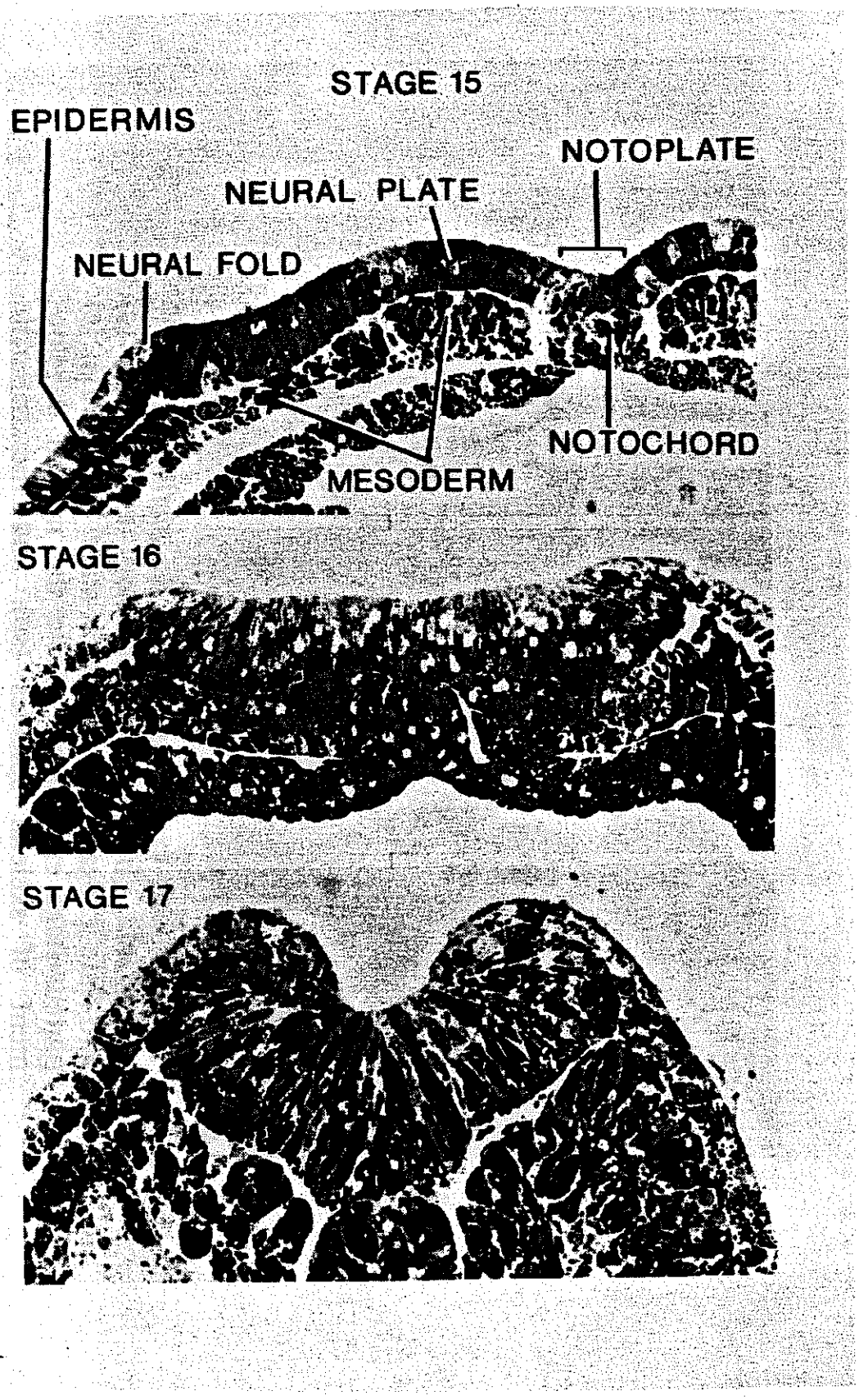

Fig. 5.5. (Continued on the next page).

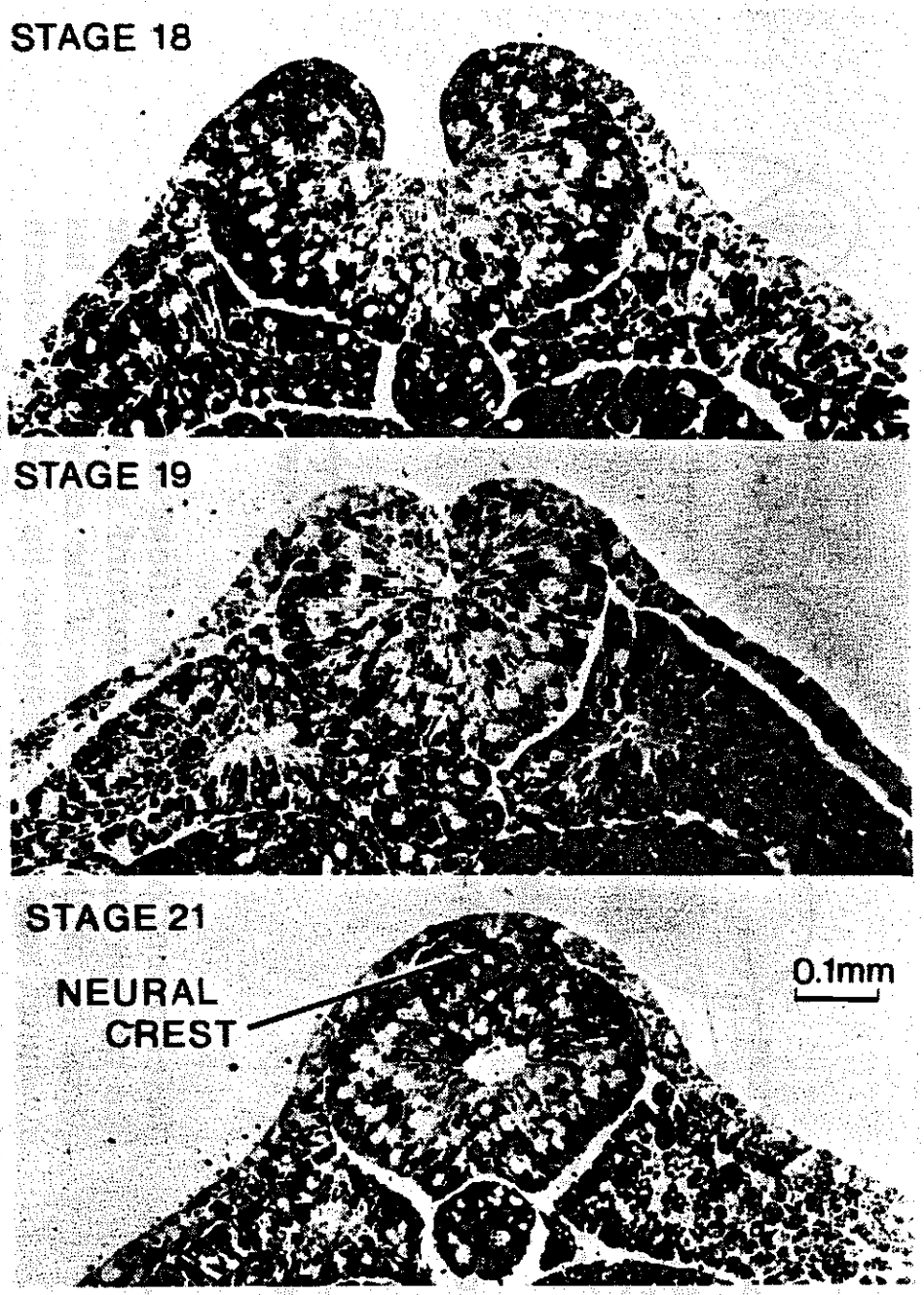

Fig. 5.5. The neural plate, and the tissues that underlie it, are shown in cross section at stages through the period of neural fold formation and rolling of the plate into a tube, in newt embryos. (From Jacobson, Oster, Odell and Cheng [1986]).

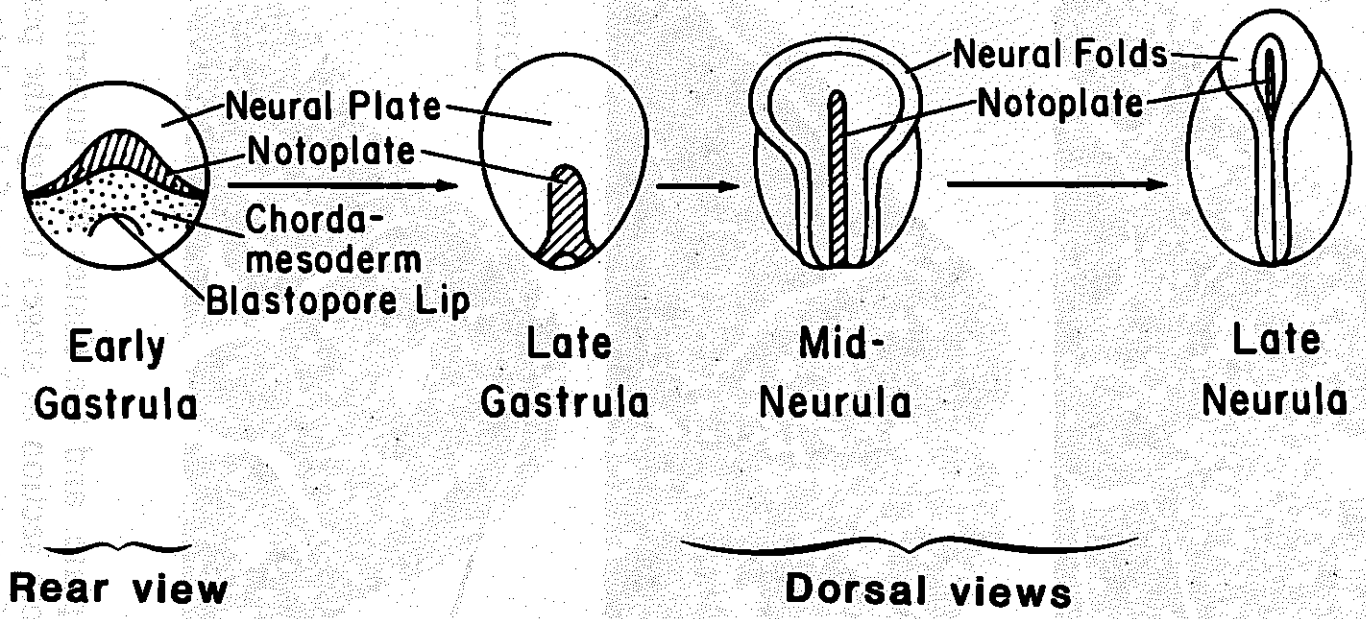

Fig. 5.6. Development of newt embryos from early gastrula to late neurula stages. The notochord shown above the dorsal lip of the blastopore of the early gastrula has involuted around the blastopore lip and lies beneath the notoplate in subsequent stages. (From Jacobson, Oster, Odell and Cheng [1986]).

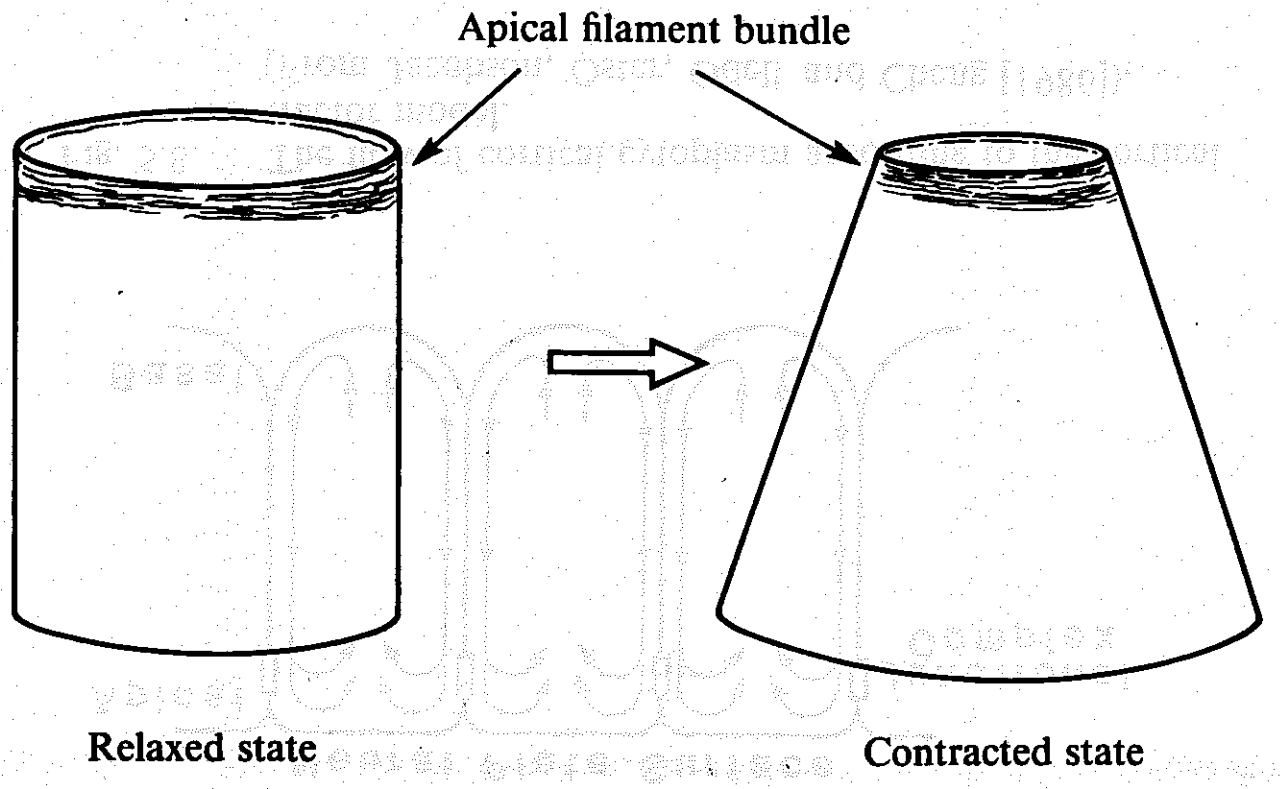

Fig. 5.7. The "apical constriction" hypothesis.

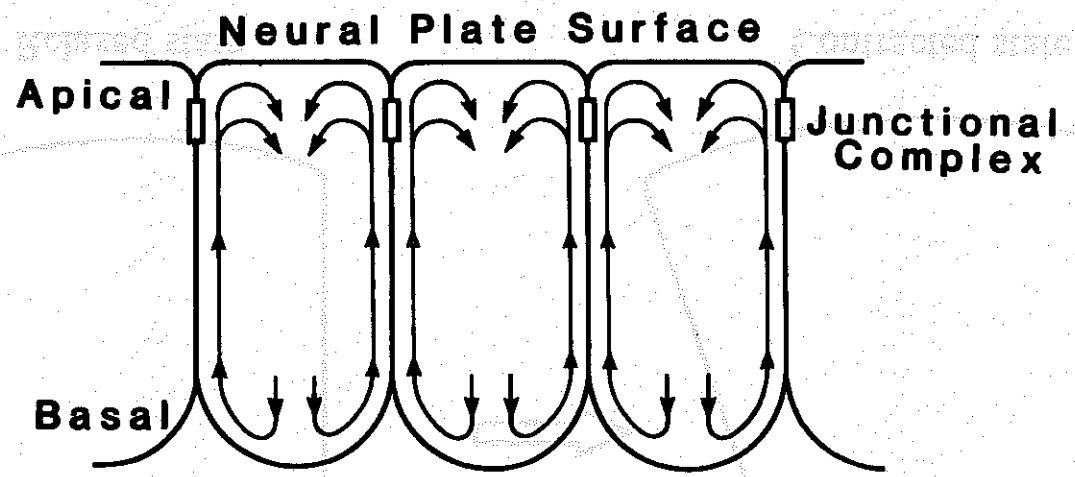

Fig. 5.8. The flow of cortical cytoplasm according to the cortical tractor model.
(From Jacobson, Oster, Odell and Cheng [1986]).

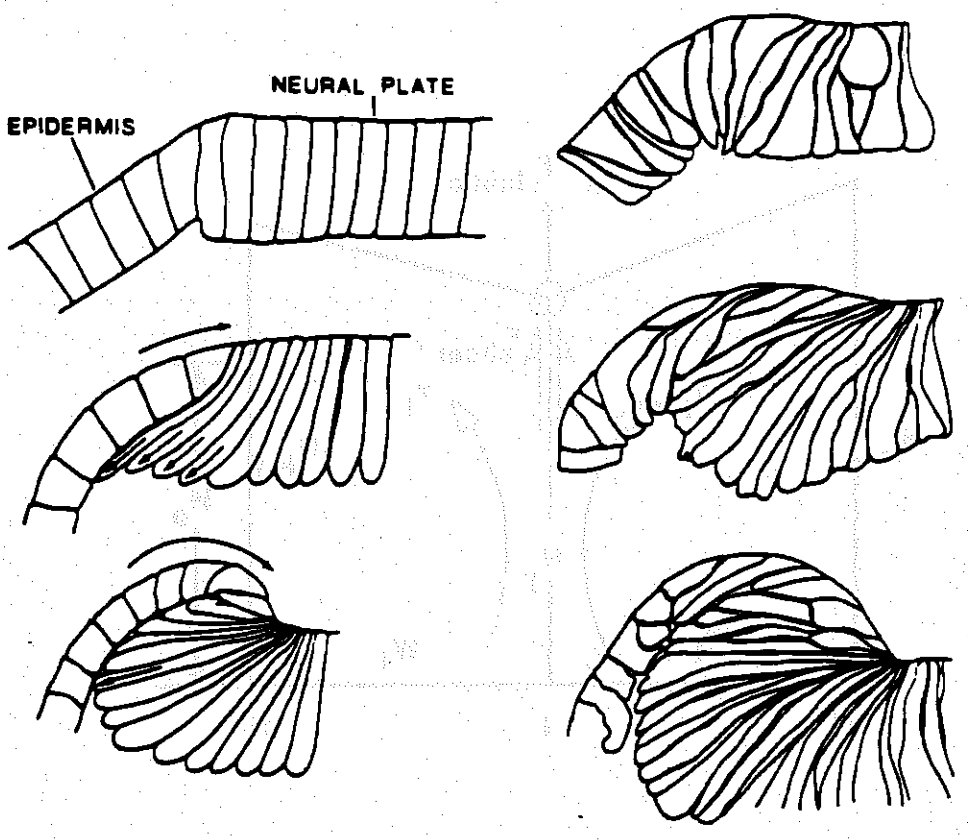

Interpretation of events

Tracings of cells from cross sections of newt neurulae at stages 15, 16 and 17.

Fig. 5.9. The "cortical tractor" hypothesis. Neural plate cells tractor on the bottoms of the epidermal cells, pulling them into a fold, and at the same time stretching the neural plate cells until their apical surfaces are points, or even become released. This tractoring motion produces a rolling moment toward the midline and lifts the folds up out of the plane.
(From Jacobson, Oster, Odell and Cheng [1986]).

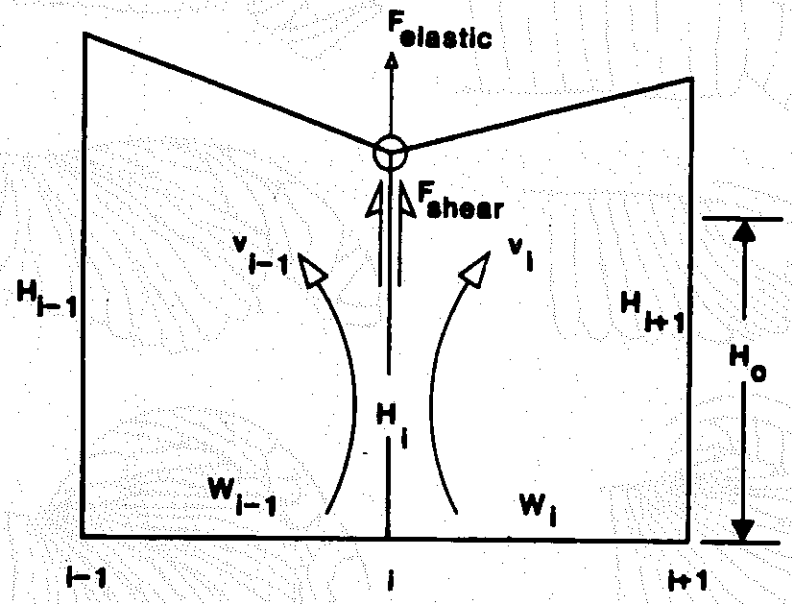

Fig. 5.10. A free body diagram of two adjacent cells showing the elastic, shear and tractor forces.

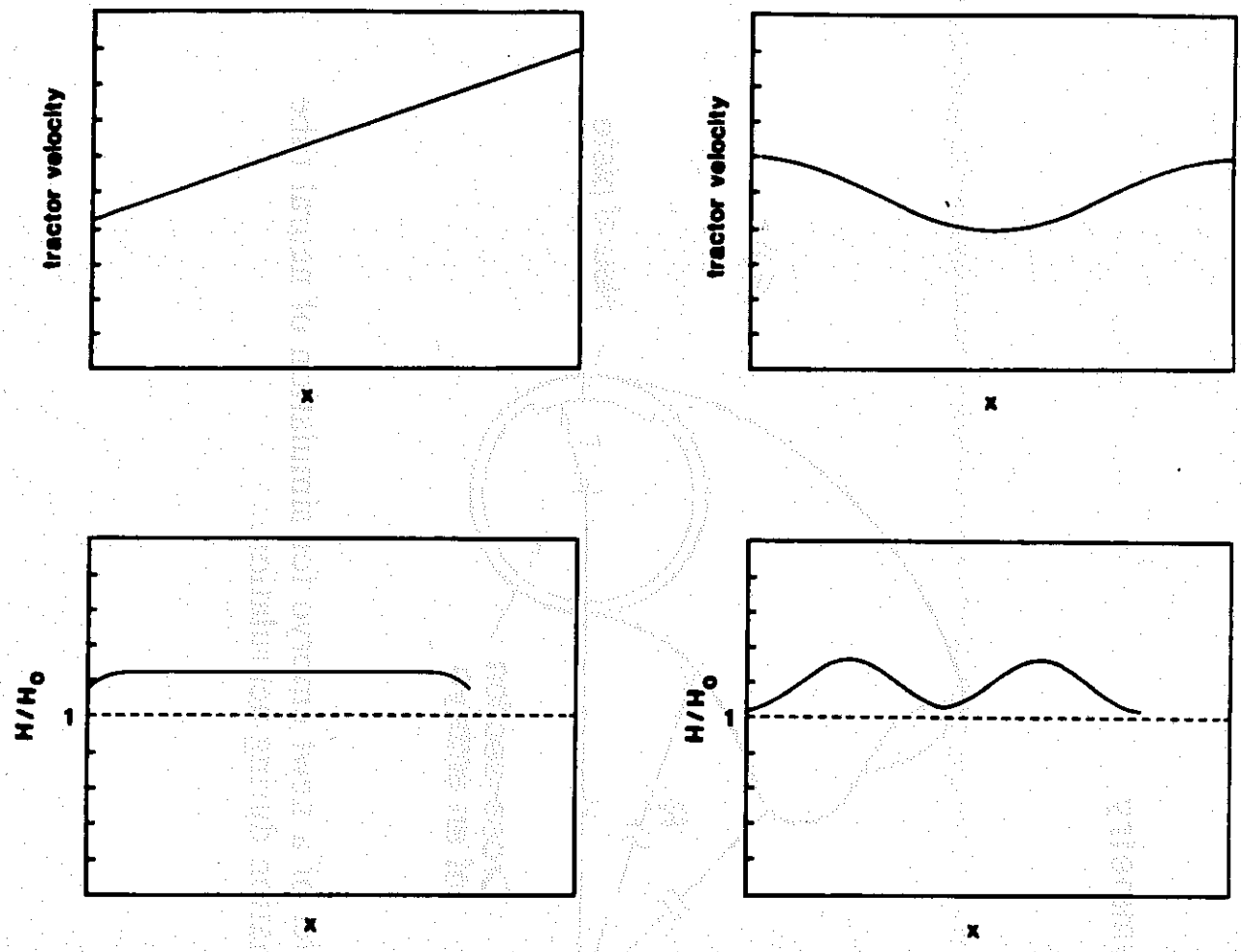

Fig. 5.11. The deformation fields corresponding to (a) a linear tractor velocity field, and (b) a periodic velocity field.

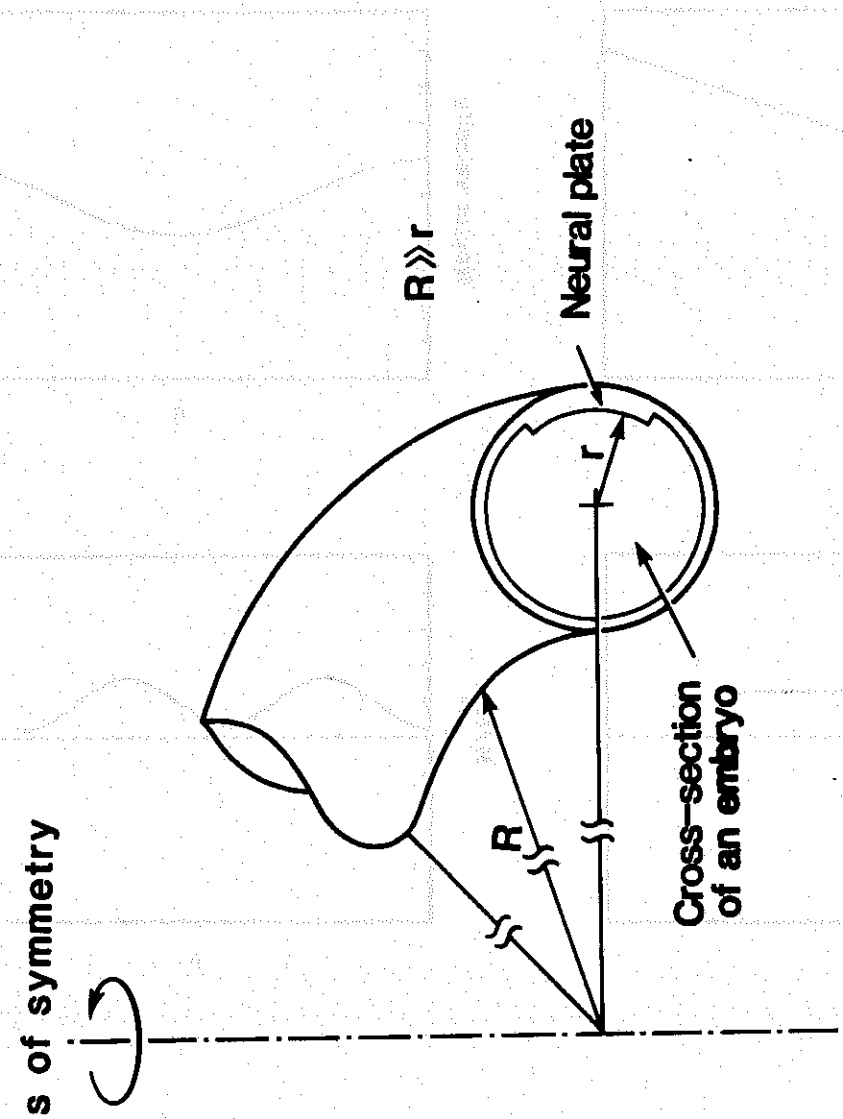

Fig. 5.12. Model of a newt embryo for simulation of neural tube formation during neurulation.

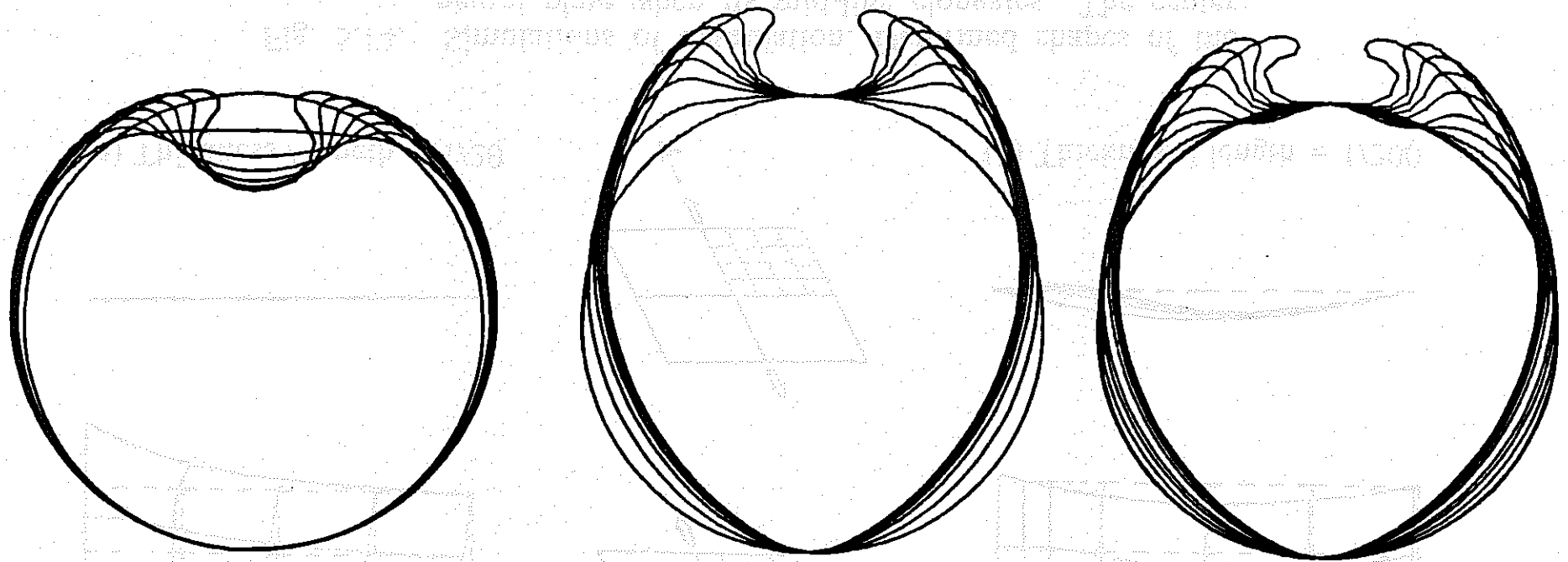

(a) Uniform rolling moment

(b) Uniform rolling moment + notochord fixed

(c) Rolling moment commences at plate edge and proceeds inward towards centerline + notochord fixed

Fig. 5.13. Simulation of neurulation. Deformed shapes of an embryo due to a rolling moment acting over the neural plate.

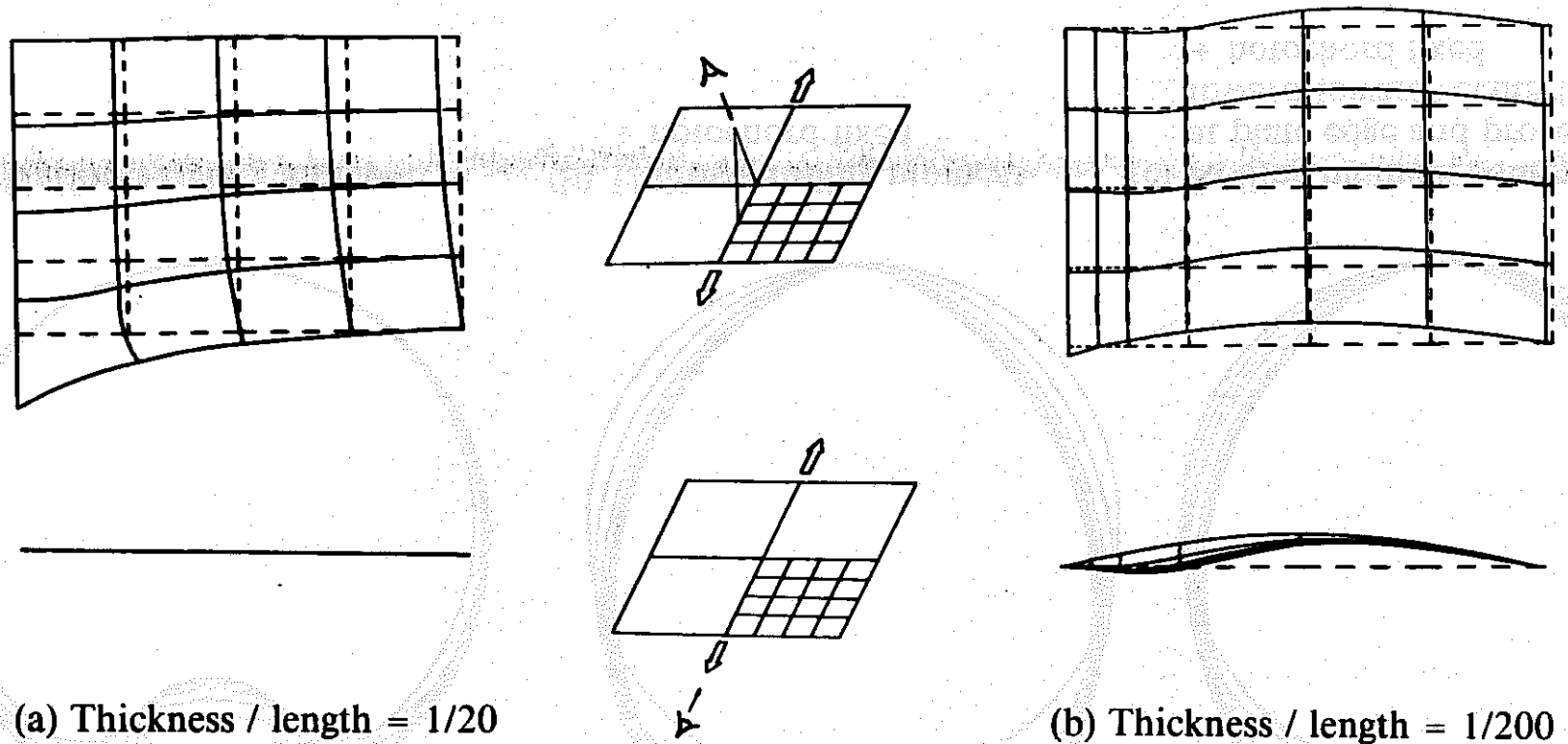

(a) Thickness / length = 1/20

(b) Thickness / length = 1/200

Fig. 5.14. Simulations of neurulation. Deformed shapes of the neural plate when its mid-line elongates. The center diagrams indicate the angles from which the diagrams at left and right are viewed.

Chapter 6
Closure

The first part of this study was devoted to developing efficient and accurate methods for mechanical analyses of cells and embryos. Using the finite element method as the computational framework, I have developed an axisymmetric shell/membrane element based on a stress resultant formulation, a volume constraint algorithm based on the Lagrange multiplier method, and finally a contact algorithm based on the penalty method.

Using these finite element tools, I simulated three commonly used mechanical experiments on sea urchin eggs -- the compression experiment, the suction experiment, and the magnetic particle experiment. I have also studied two developmental events -- gastrulation in sea urchins and neurulation in amphibia. These examples demonstrate how valuable it is to apply mechanics to cell and developmental biology.

There are numerous possible extensions to further study problems in cell and developmental biology. I have included below a brief list of interesting future topics:

- Analyses of other mechanical experiments, such as the sessile drop experiment (Hiramoto [1967]). There, the effect of the centrifugal force has to be included.
- Analyses of mechanical experiments on red blood cells (Evans and Skalak [1979a,b]). There, we need to account for the red cell's large resistance to area deformation.
- Study of surface adhesiveness of cells (see Evans [1980] for work on red blood cells). This requires modifications to the current contact algorithm.
- Analyses of mechanical experiments on tissues and embryos.

- Simulation of cell division (see Pujara and Lardner [1979], Akkas [1980,1981]).
- Analyses of mechanical experiments on dividing cells (see Hiramoto [1981]).
- Simulations of mechanical waves in amphibian eggs (see Cheer, Nuccitelli, Oster and Vincent [1986]).
- Simulations of plasmodial oscillations in *Physarum* (see Oster and Odell [1984]). The periodic contraction rhythms observed in *Physarum* strands are believed to be orchestrated by a mechanochemical mechanism. This requires solving a coupled mechanochemical problem which involves the diffusion/reaction of chemicals, the large deformations of the strands, and the coupling of the chemical and the mechanical variables.

Appendix 1

Shell Coordinate System

Two coordinate systems are used for the development of this nonlinear theory of the axisymmetric shell. The reference configuration is described by coordinates X^K with covariant base vectors $\mathbf{G}_K$, $K=1,3$. As for the current (deformed) configuration, the coordinates x^k with covariant base vectors $\mathbf{g}_k$, $k=1,3$, are used. These two coordinate systems are illustrated in Fig 1. In the evaluation of the kinematic relationships, and the expression of the equilibrium equations for the shell, quantities such as the metric tensors and the Christoffel symbols for these coordinate systems are called for. These quantities will be evaluated in the following. More formal presentation on this subject can be found in Naghdi [1972], Malvern [1965] and Flügge [1972].

Base vectors. For the current configuration, we denote the contravariant base vectors conjugate to the covariant base vectors $\mathbf{g}_k$ by $\mathbf{g}^k$, and the corresponding components by x_k, $k=1,3$. These bases can be related to the cartesian coordinate as follows. A position vector $\mathbf{dp}$ in space can be expressed as

$$\mathbf{dp} = dx^k\, \mathbf{i}_k \tag{A1.1a}$$

where dx^k is the kth component of $\mathbf{dp}$ in the cartesian basis $\mathbf{i}_k$, $k=1,3$, Here, the summation convention is implied for repeated indices. This same position vector $\mathbf{dp}$ can be similarly written in terms of the shell coordinates, we have

$$\mathbf{dp} = dx^i \mathbf{g}_i = dx_j \mathbf{g}^j \tag{A1.1b}$$

From these two expressions (A1.1a) and (A1.1b), we can establish the relationship of the covariant base vectors $\mathbf{g}_k$ and the cartesian base vectors $\mathbf{i}_m$ by differentiation,

$$\mathbf{g}_k = \frac{\partial \mathbf{p}}{\partial x^k} = \frac{\partial \mathbf{p}}{\partial z^m}\frac{\partial z^m}{\partial x^k} = \frac{\partial z^m}{\partial x^k}\mathbf{i}_m \tag{A1.2}$$

Since the contravariant basis is defined as the dual basis of $\boldsymbol{g}_i$ such that $\boldsymbol{g}_i \cdot \boldsymbol{g}^j = \delta_i{}^j$, its relationship with the cartesian basis $\mathbf{i}^m$ (same as $\mathbf{i}_m$) can be obtained from (A1.2) as

$$\boldsymbol{g}^k = \frac{\partial x^k}{\partial z^m}\,\mathbf{i}^m \tag{A1.3}$$

For the shell coordinate system here, relations (A1.2) and (A1.3) can be evaluated first by examining Fig. 1. Defining the radius in the current configuration as $r \equiv x^1\sin\alpha + x^2\cos\alpha$, we can determine that

$$\begin{aligned} z^1 &= r\cos x^3 \\ z^2 &= -r\sin x^3 \\ z^3 &= -x^1\cos\alpha + x^2\sin\alpha \end{aligned} \tag{A1.4}$$

Evaluating (A1.2) using (A1.4), we obtain the expression for the covariant base vectors:

$$\begin{aligned} \boldsymbol{g}_1 &= \sin\alpha\cos x^3\,\mathbf{i}_1 - \sin\alpha\sin x^3\,\mathbf{i}_2 - \cos\alpha\,\mathbf{i}_3 \\ \boldsymbol{g}_2 &= \cos\alpha\cos x^3\,\mathbf{i}_1 - \cos\alpha\sin x^3\,\mathbf{i}_2 + \sin\alpha\,\mathbf{i}_3 \\ \boldsymbol{g}_3 &= -r\sin x^3\,\mathbf{i}_1 - r\cos x^3\,\mathbf{i}_2 \end{aligned} \tag{A1.5}$$

Using the inverse relation of (A1.4), the contravariant base vectors in (A1.3) becomes,

$$\begin{aligned} \boldsymbol{g}^1 &= \sin\alpha\cos x^3\,\mathbf{i}^1 - \sin\alpha\sin x^3\,\mathbf{i}^2 - \cos\alpha\,\mathbf{i}^3 \\ \boldsymbol{g}^2 &= \cos\alpha\cos x^3\,\mathbf{i}^1 - \cos\alpha\sin x^3\,\mathbf{i}^2 + \sin\alpha\,\mathbf{i}^3 \\ \boldsymbol{g}^3 &= -\frac{\sin x^3}{r}\,\mathbf{i}^1 - \frac{\cos x^3}{r}\,\mathbf{i}^2 \end{aligned} \tag{A1.6}$$

Comparison of (A1.5) and (A1.6) reflects an important character about the local coordinate system chosen: the covariant and the contravariant base vectors are identical in the first two directions, and they are different only in magnitude

in the third direction. Furthermore, the base vectors $\mathbf{g}_1$, $\mathbf{g}_2$, $\mathbf{g}^1$ and $\mathbf{g}^2$ are all unit vectors. The unit vectors in the 3-direction can be found from (A1.5) and (A1.6) to be

$$\widehat{\mathbf{g}}_3 = \frac{1}{r}\mathbf{g}_3\,, \qquad \widehat{\mathbf{g}}^3 = \frac{1}{r}\mathbf{g}^3 \tag{A1.7a}$$

for the current configuration. Similar results are found for the reference configuration:

$$\widehat{\mathbf{G}}_3 = \frac{1}{R}\mathbf{G}_3\,, \qquad \widehat{\mathbf{G}}^3 = \frac{1}{R}\mathbf{G}^3 \tag{A1.7b}$$

Metric tensors. The metric tensors, defined as $g_{ij} = \mathbf{g}_i \cdot \mathbf{g}_j$ and $g^{ij} = \mathbf{g}^i \cdot \mathbf{g}^j$, can be obtained directly from (A1.5) and (A1.6). They are

$$\left[g_{ij}\right] = \begin{bmatrix} 1 & 0 & 0 \\ 0 & 1 & 0 \\ 0 & 0 & (r)^2 \end{bmatrix} \tag{A1.8}$$

and

$$\left[g^{ij}\right] = \begin{bmatrix} 1 & 0 & 0 \\ 0 & 1 & 0 \\ 0 & 0 & \dfrac{1}{(r)^2} \end{bmatrix} \tag{A1.9}$$

where the superscript associated with a bracketed quantity denotes its power. It is noted that both metric tensors given above are diagonal matrices, implying that the shell coordinate system is an ***orthogonal*** system. This will result in some important simplifications to the subsequent development.

Following the same method used above, the metric tensors G_{IJ} and G^{IJ} corresponding to the reference configuration can be found to be

$$\left[G_{IJ}\right] = \begin{bmatrix} 1 & 0 & 0 \\ 0 & 1 & 0 \\ 0 & 0 & (R)^2 \end{bmatrix} \tag{A1.10}$$

and

$$\left[G^{IJ}\right] = \begin{bmatrix} 1 & 0 & 0 \\ 0 & 1 & 0 \\ 0 & 0 & \dfrac{1}{(R)^2} \end{bmatrix} \tag{A1.11}$$

where R is the radius in the reference configuration defined as $R \equiv X^1 \sin\alpha + X^2 \cos\alpha$.

Permutation tensors. A permutation symbol e_{lmn} (or e^{lmn}) is defined as

$$e_{lmn} = e^{lmn} = \begin{cases} 1 & \text{if } lmn = 123, 231, 312 \\ -1 & \text{if } lmn = 321, 213, 132 \\ 0 & \textit{otherwise} \end{cases}$$

The permutation tensors ε_{lmn} and ε^{lmn} for any coordinate system are related to these permutation symbols e_{lmn} and e^{lmn} by

$$\varepsilon_{lmn} = \sqrt{\det(g_{ij})}\, e_{lmn} \tag{A1.12}$$

$$\varepsilon^{lmn} = \sqrt{\det(g^{ij})}\, e^{lmn}$$

With the results from (A1.8) and (A1.9), (A1.12) becomes

$$\varepsilon_{lmn} = \tau\, e_{lmn}\,; \qquad \varepsilon^{lmn} = e^{lmn} / \tau \tag{A1.13}$$

These permutation tensors above are associated with the current configuration. Similarly for the reference configuration, they are given by

$$\varepsilon_{LMN} = R\, e_{LMN}\,; \qquad \varepsilon^{LMN} = e^{LMN} / R \tag{A1.14}$$

Christoffel symbols. The Christoffel symbols for the current configuration, denoted here as γ_{ijk} and $\gamma_{ij}{}^{k}$, are defined as

$$\mathbf{g}_{i,j} = \gamma_{ijk}\, \mathbf{g}^{k} = \gamma_{ij}{}^{k}\, \mathbf{g}_{k} \tag{A1.15}$$

where $,j$ denotes differentiation with respect to x^j. Prior to evaluating them for the shell coordinate system, some general properties of the Christoffel symbols are stated.

From its definition in (A1.15), it follows that

$$\gamma_{ijk} = \mathbf{g}_{i,j} \cdot \mathbf{g}_k \tag{A1.16}$$

and

$$2\gamma_{ijk} = g_{jk,i} + g_{ki,j} - g_{ij,k} \tag{A1.17}$$

It can also be shown that the two Christoffel symbols, γ_{ijk} and $\gamma_{ij}{}^k$, are related to each other by

$$\gamma_{ijl} = \gamma_{ij}{}^k g_{kl}; \quad \gamma_{ijk} g^{kl} = \gamma_{ij}{}^l \tag{A1.18}$$

Finally, the Christoffel symbols are symmetric with respect to the first two subscripts:

$$\gamma_{ijk} = \gamma_{jik}; \quad \gamma_{ij}{}^k = \gamma_{ji}{}^k \tag{A1.19}$$

Because the metric tensor g_{ij} is diagonal for orthogonal systems, the only nonzero components of the metric tensor after differentiation are

$$g_{33,1} = 2r\sin\alpha; \quad g_{33,2} = 2r\cos\alpha \tag{A1.20}$$

As a consequence, the only nonzero Christoffel symbols, by (A1.17) and (A1.18), are

$$\begin{aligned} \gamma_{33}{}^1 &= -r\sin\alpha \\ \gamma_{33}{}^2 &= -r\cos\alpha \\ \gamma_{31}{}^3 &= \gamma_{13}{}^3 = \sin\alpha / r \\ \gamma_{32}{}^3 &= \gamma_{23}{}^3 = \cos\alpha / r \end{aligned} \tag{A1.21}$$

In the reference configuration, the Christoffel symbols are denoted by Γ_{IJK} and $\Gamma_{IJ}{}^K$. The counterpart of (A1.21) is

$$\begin{aligned} \Gamma_{33}{}^1 &= -R\sin\alpha \\ \Gamma_{33}{}^2 &= -R\cos\alpha \end{aligned} \tag{A1.22}$$

$$\Gamma_{31}{}^{3} = \Gamma_{13}{}^{3} = \sin\alpha / R$$

$$\Gamma_{32}{}^{3} = \Gamma_{23}{}^{3} = \cos\alpha / R$$

where $R \equiv X^1 \sin\alpha + X^2 \cos\alpha$.

Appendix 2

Derivations Leading To (2.6.11)

This appendix contains the derivation of the results used in proceeding from (2.6.10) to (2.6.11). The term of concern here is the one involving $\delta\psi$ multiplying P^{21} and P^{22}:

$$-\int_{-h/2}^{h/2}\delta\psi[\cos\psi\ \sin\psi]\begin{Bmatrix}P^{21}\\P^{22}\end{Bmatrix}RdX^2 \tag{A2.1}$$

First consider the stresses defined in the deformed section σ and τ. Combining (2.3.8), (2.3.11a) and the definition of σ in (2.4.10a)

$$\sigma = \left(\frac{d\omega}{d\Omega}\right)^{-1}J(\mathbf{F}^{T-1}\mathbf{G}_1)\cdot(\mathbf{P}^T\mathbf{G}_1) = \left(\frac{d\omega}{d\Omega}\right)^{-1}J\mathbf{G}_1\cdot(\mathbf{F}^{-1}\mathbf{P}^T)\mathbf{G}_1 \tag{A2.2}$$

$$= \left(\frac{d\omega}{d\Omega}\right)^{-1}J\mathbf{G}_1\cdot\mathbf{S}^T\mathbf{G}_1 = \left(\frac{d\omega}{d\Omega}\right)^{-1}JS^{11} = \frac{R}{\tau}JS^{11}$$

where the relation $\mathbf{P} = \mathbf{S}\mathbf{F}^T$ is used above. From (2.4.10b), using (2.3.7) and the expression of σ above,

$$\tau = \hat{\mathbf{l}}\cdot(\mathbf{P}^T\mathbf{G}_1) = (\mathbf{F}\mathbf{G}_2)\cdot(\mathbf{F}\mathbf{S}^T\mathbf{G}_1) \tag{A2.3}$$

$$= \mathbf{G}_2\cdot(\mathbf{C}\mathbf{S}^T\mathbf{G}_1) = C_{12}S^{11} + C_{22}S^{21} = C_{12}\frac{\tau\sigma}{RJ} + S^{21}$$

The product in (A2.1): $(\cos\psi P^{21} + \sin\psi P^{22})$ can also be written as $\hat{\mathbf{n}}\cdot(\mathbf{P}^T\mathbf{G}_2)$, in view of (2.3.11b). Utilizing the expression of τ in (A2.3), it can be simplified to become

$$\hat{\mathbf{n}}\cdot(\mathbf{P}^T\mathbf{G}_2) = \left(\frac{d\omega}{d\Omega}\right)^{-1}J(\mathbf{F}^{T-1}\mathbf{G}_1)\cdot(\mathbf{P}^T\mathbf{G}_2) = \left(\frac{d\omega}{d\Omega}\right)^{-1}J\mathbf{G}_1\cdot(\mathbf{F}^{-1}\mathbf{P}^T\mathbf{G}_2) \tag{A2.4}$$

$$= \left(\frac{d\omega}{d\Omega}\right)^{-1}J\mathbf{G}_1\cdot(\mathbf{S}^T\mathbf{G}_2) = \left(\frac{d\omega}{d\Omega}\right)^{-1}JS^{21} = \frac{R}{\tau}J\left(\tau - C_{12}\frac{\tau\sigma}{RJ}\right)$$

$$= \tau J\frac{R}{\tau} - C_{12}\sigma\ .$$

Using this result, (A2.1) takes the final form

$$-\int_{-h/2}^{h/2} \delta\psi[\cos\psi \ \sin\psi]\begin{Bmatrix} P^{21} \\ P^{22} \end{Bmatrix} R dX^2 = -\int_{-h/2}^{h/2} \delta\psi(\tau J\frac{R}{r} - C_{12}\sigma) R dX^2 \ . \qquad \text{(A2.5)}$$

References

References cited in Chapter 2.

Argyris J.H. *et al* [1979]. Finite element method - the natural approach. *Comp. Meth. in Appl. Mech. and Engr.* **17/18**: 1-106.

Flügge W. [1972]. *Tensor Analysis and Continuum Mechanics*. Springer-Verlag, New York.

Green A.E. and Adkins J.E. [1960]. *Large Elastic Deformations*. Oxford University Press, London.

Halleux J.P. [1980]. Non-linear transient analysis of thin axisymmetric structures. In: *Proc. Intern. Conf. on Num. Meth. for Non-linear Problems*.1, (Taylor C., Hinton E. and Owen D.R.J. Ed), University College of Swansea, U.K.

Hibbitt H.D. [1979]. Some follower forces and load stiffness. *Intern. J. for Num. Meth. in Eng.* **14(6)**: 937-941.

Hughes T.J.R. and Pister K.S. [1978]. Consistent linearization in mechanics of solids and structures. *Computers and Structures*, **8**: 391-397.

Malvern L.E. [1965]. *Introduction to the Mechanics of a Continuous Medium*. Prentice-Hall,New Jersey.

Marsden J.E. and Hughes T.J.R. [1983]. *Mathematical Foundations of Elasticity*. Prentice-Hall, New Jersey.

Mescall J.F. [1965]. Large deflections of spherical shells under concentrated loads. *J. Appl. Mech.* **32**: 936-938.

Naghdi P.M. [1972]. The theory of shells and plates. In: *S. Flügge's Handbach der Physik*. Vol. VIa/2, pp 425-640. (C. Truesdell, Ed.), Springer-Verlag, New York.

Oden J.T. [1972]. *Finite Elements of Nonlinear Continua*, McGraw Hill, New York.

Pian H.H.T. [1983]. Hybrid and Mixed Finite Element Methods. (S.N. Atluri, R.H. Gallagher and O.C.Zienkiewicz, Ed.), John Wiley and Sons.

Reissner E. [1950a]. On a variational theorem in elasticity. *J. Math. Phys.*, **29**: 90-95.

Reissner E. [1950b]. On axisymmetric deformation of thin shells of revolution. *Proc. Symp. in Appl. Math.* **3**: 32.

Riks E. [1972]. The application of Newton's method to the problem of elastic stability, *J. Appl. Mech.* **39**: 1060-1066.

Schweizerhof K. and Ramm E. [1984]. Displacement dependent pressure loads

in nonlinear finite element analysis. *Comp. & Struct.*, **18**: 1099-1114.

Simo J.C. [1982]. A consistent formulation of nonlinear theories of elastic beams and plates. *Report No. UCB/SESM-82/06*, University of California, Berkeley.

Simo J.C., Hjelmstad K.D. and Taylor R.L. [1983]. Finite element formulations for problems of finite deformation of elasto-viscoplastic beams. *Report No. UCB/SESM-83/01*, University of California, Berkeley.

Simo J.C. [1984]. On a one-dimensional finite strain beam theory: the 3-dimensional dynamic problem. *Report No. UCB/SESM-84/02*, University of California, Berkeley.

Wempner G.A. [1972]. Discrete approximations related to nonlinear theories of solids. *Int. J. Solid Structures*, **7**: 1581-1599.

Zienkiewicz O.C. [1977]. *The Finite Element Method*. 3rd Ed., McGraw Hill, London.

References cited in Chapter 3.

Hughes T.R.J., Taylor R.L., Sackman J.L., Curnier A. and Kanoknukulchai W [1976]. A finite element method for a class of contact-impact problems. *Comp. Meth. Appl. Mech. Engng.* **8**: 249-276.

Kikuchi N. and Oden J.T. [1984]. Contact problems in elastostatics. In: *Finite Elements: Special Problems in Solid Mechanics*, Vol **IV**, (Oden and Carey, Ed.), Prentice-Hall, Englewood Cliffs, New Jersey.

Landers J.A. and Taylor R.L. [1985] An augmented Lagrangian formulation for the finite element solution of contact problems. *Report No. UCB/SESM-85/09*, University of California, Berkeley.

Simo J.C., Wriggers P. and Taylor R.L. [1984] A perturbed Lagrangian formulation for the finite element solution of contact problems. *Report No. UCB/SESM-84/14*, University of California, Berkeley.

References cited in Chapter 4.

Cole K.S. [1932]. Surface forces of the *Arbacia* egg. *J. Cell. Comp. Physiol.* 1: 1-9.

Evans E.A. [1983]. Bending elastic modulus of red blood cell membrane derived from buckling instability in micropipette aspiration tests. *Biophys. J.* **43**: 27-30.

Evans E.A. and R. Skalak [1979a]. Mechanics and thermodynamics of biomembranes: Part 1. *CRC Critical Rev. in Bioeng.* **3(4)**: 181-330.

Evans E.A. and R. Skalak [1979b]. Mechanics and thermodynamics of biomembranes: Part 2. *CRC Critical Rev. in Bioeng.* **3(4)**: 331-418.

Evans E.A., R. Waugh and Melnik L. [1976]. Elastic area compressibility modulus of red cell membrane. *Biophys. J.* **16**: 585-595.

Hiramoto Y. [1963]. Mechanical properties of sea urchin eggs. I. Surface force and elastic modulus of the cell membrane. *Exp. Cell Res.* **32**: 59-75.

Hiramoto Y. [1967]. Observations and measurements of sea urchin eggs with a centrifuge microscope. *J. Cell. Physiol.* **69**: 219-230.

Hiramoto Y. [1969a]. Mechanical properties of the protoplasm of the sea urchin egg. I. Unfertilized eggs. *Exp. Cell Res.* **56**: 201-208.

Hiramoto Y. [1969b]. Mechanical properties of the protoplasm of the sea urchin egg. II. Fertilized eggs. *Exp. Cell Res.* **56**: 209-218.

Hiramoto Y. [1970]. Review article: rheological properties of sea urchin eggs. *Biorheology*. **6**: 201-234.

Hiramoto Y. [1974]. Mechanical properties of the surface of the sea urchin egg at fertilization and during cleavage. *Exp. Cell Res.* **89**: 320-326.

Hiramoto Y. [1981]. Mechanical properties of dividing cells. In: *Mitosis/Cytokinesis* (A.M. Zimmerman and A. Fover, ed.), pp.397-416. Academic Press, New York.

Mitchison J.M. and M.M. Swann [1954a]. The mechanical properties of the cell surface. I. The cell elastimeter. *J. Exp. Biol.* **31**: 443-461.

Mitchison J.M. and M.M. Swann [1954b]. The mechanical properties of the cell surface. II. The unfertilized sea-urchin egg. *J. Exp. Biol.* **31**: 461-472.

Rand R.P. and Burton A.C. [1964]. Mechanical properties of the red cell membrane. I. Membrane stiffness and intracellular pressure. *Biophys. J.* **4**: 115.

Rappaport R. [1971]. Cytokinesis in animal cells. In: *International review of cytology* (G.H. Bourne, J.F. Danielli and K.W. Jeon, ed.), pp.169-211. Academic Press, New York.

Richardson E. [1975]. Analysis of suction experiments on red blood cells. *Biorheology* **12**: 39-55.

Yoneda M. [1964]. Tension at the surface of sea urchin egg: A critical examination of Cole's experiment. *J. Exp. Biol.* **41**: 893-906.

Zienkiewicz O.C. [1977]. *The Finite Element Method*, 3rd Ed., McGraw-Hill, London.

References cited in Chapter 5.

Burnside B. [1971]. Microtubules and microfilaments in newt neurulation. *Devel. Biol.* **85**: 416-441.

Burnside B. [1973]. Microtubules and microfilaments in amphibian neurulation.

Am. Zool. **13**: 989-1006.

Cheng L.Y., Murray J.D., Odell G.M. and Oster G.F. [1986]. The cortical tractor: a new model for epithelial morphogenesis. In: *Lecture Notes in Biomathematics*. Springer-Verlag, Berlin. (in press).

Dan K. and Okazaki D. [1956]. Cyto-embryological studies of sea urchins. III. Role of the secondary mesenchyme cells in the formation of the primitive gut in sea urchin larvae. *Biol. Bull.* **110**: 29-42.

Ettensohn C.A. [1985]. Mechanisms of epithelial invagination. *Quar. Rev. Biol.* **60**: 289-307.

Gustafson T. and Kinnander [1956]. Microaquaria for time-lapse cinematographic studies of morphogenesis in swimming larvae and observations on gastrulation. *Exp. Cell Res.* **11**: 36-57.

Gustafson T. and Kinnander [1960]. Cellular mechanisms in morphogenesis of the sea urchin gastrula. *Exp. Cell Res.* **21**: 361-373.

Gustafson T. and Wolpert L. [1963]. The cellular basis of morphogenesis and sea urchin development. *Int. Rev. Cyt.* **15**: 139-214.

Hardin J.D. and Cheng L.Y. [1986]. The mechanisms and mechanics of archenteron elongation during sea urchin gastrulation. *Devel. Biol.* (To appear).

Hibbitt, Karlsson and Sorensen, Inc. [1982]. *ABAQUS User's Manual*, 35 South Angeli Street, Providence, Rhode Island RI 02906.

Horstadius S. [1973]. *Experimental embryology of echinoderms*. Oxford, Clarendon Press.

Jacobson A.G. [1981]. Morphogensis of the neural plate and tube. In: *Morphogenesis and Pattern Formation*. (T.G. Connelly, Brinkley L.L. and Carlson B.M., ed.), pp. 233-263, Raven Press, New York.

Jacobson A.G., Odell G.M. and Oster G.F. [1985]. The cortical tractor model for epithelial folding: application to the neural plate. In: *Molecular Determinants of Animal Form*. (G. Edelman, ed.), U.C.L.A. Sympos. Molec. Cell Biol., New Series, Vol. **31**, pp. 143-167. Alan R. Liss Inc., New York.

Jacobson A.G., Oster G.F., Odell G.M. and Cheng L.Y. [1986]. Neurulation and the cortical tractor model for epitheial folding. *J. Embryol. Exp. Morphol.* (To appear).

Okazaki K. [1956]. Exogastrulation induced by calcium deficiency in the sea uchin, *Embryologia* **3**: 23-36.

Odell G., Oster G., Burnside P. and Alberch P. [1981]. The mechanical basis of morphogenesis. I: Epithelial folding and invagination. *Devel. Biol.* **85**: 446-462.

Oster G.F. and Odell G.M. [1984]. The mechanochemistry of cytogels. *Physica*

12D: 333-350.

References cited in Chapter 6.

Akkas N. [1980]. On the biomechanics of cytokinesis in animal cells. *J. Biomechanics*. **13**: 977-988.

Akkas N. [1981]. A viscoelastic model for cytokinesis in animal cells. *J. Biomechanics*. **14**: 621-631.

Cheer A., Nuccitelli R., Oster G. and Vincent J-P. [1986]. Cortical activity in vertebrate eggs. I: The activation waves. *J. Theo. Biol.* (To appear).

Evans E.A. and R. Skalak [1979a]. Mechanics and thermodynamics of biomembranes: Part 1. *CRC Critical Rev. in Bioeng.* **3(4)**: 181-330.

Evans E.A. and R. Skalak [1979b]. Mechanics and thermodynamics of biomembranes: Part 2. *CRC Critical Rev. in Bioeng.* **3(4)**: 331-418.

Evans E.A. [1980]. Minimum energy analysis of membrane deformation applied to pipet aspiration and surface adhesion of red blood cells. *Biophys. J.* **30**: 265-284.

Hiramoto Y. [1967]. Observations and measurements of sea urchin eggs with a centrifuge microscope. *J. Cell. Physiol.* **69**: 219-230.

Hiramoto Y. [1981]. Mechanical properties of dividing cells. In: *Mitosis/Cytokinesis* (A.M. Zimmerman and A. Fover, ed.), pp.397-418. Academic Press, New York.

Oster G.F. and Odell G.M. [1984]. The mechanics of cytogels. I. Plasmodial oscillations in *Physarum*. *Cell Motility*. **4**: 469.

Pujara P. and Lardner T.J. [1979]. A model for cell division. *J. Biomechanics*. **12**: 293-299.